

Copyright Warning & Restrictions

The copyright law of the United States (Title 17, United States Code) governs the making of photocopies or other reproductions of copyrighted material.

Under certain conditions specified in the law, libraries and archives are authorized to furnish a photocopy or other reproduction. One of these specified conditions is that the photocopy or reproduction is not to be “used for any purpose other than private study, scholarship, or research.” If a user makes a request for, or later uses, a photocopy or reproduction for purposes in excess of “fair use” that user may be liable for copyright infringement,

This institution reserves the right to refuse to accept a copying order if, in its judgment, fulfillment of the order would involve violation of copyright law.

Please Note: The author retains the copyright while the New Jersey Institute of Technology reserves the right to distribute this thesis or dissertation

Printing note: If you do not wish to print this page, then select “Pages from: first page # to: last page #” on the print dialog screen

The Van Houten library has removed some of the personal information and all signatures from the approval page and biographical sketches of theses and dissertations in order to protect the identity of NJIT graduates and faculty.

ABSTRACT

COUPLED SIMULATION OF LOADING AND RESPONSE OF COLUMNS UNDER EXTREME EVENTS

by
Navid H. Allahverdi

Forces imparted to structural columns during blast-induced loading depends on the shape and size of columns as well as on the intensity of the blast. Column's geometry – i.e., shape and size – influences the flow field around the column and consequently the flow field determines forces experienced by the column. The main objective of this research is to estimate the forces imparted to columns in a blast event through studying the air flow field around columns.

In this study, the physics of shock wave reflection and rarefaction waves are reviewed with application to describing the air flow around columns with circular and square cross sections. Then, simulations will be performed to determine the flow field around columns with different geometries. Based on the simulation results, force and impulse experienced by columns with different cross-sectional shapes and varying sizes are estimated. Finally, through curve-fitting techniques, correlations of variables are investigated and proper equations are proposed to estimate the force on columns based on shape, and size for a range of blast intensities.

Also, it is attempted to approximate the response of columns with an equivalent single-degree of freedom (SDOF) model. The parameters of the equivalent single-degree of freedom are calibrated via simulation results. Due to the relatively short duration of blast loading in comparison with columns' natural period, column responses are mainly impulse-sensitive. The proposed equations in conjunction with SDOF model can be beneficial tools in blast design practices. Furthermore, the damage and failure modes of columns are studied. For columns that prove insufficient, the efficacy of retrofitting measures such as steel jackets have been investigated.

**COUPLED SIMULATION OF LOADING AND RESPONSE OF
COLUMNS UNDER EXTREME EVENTS**

by
Navid H. Allahverdi

**A Dissertation
Submitted to the Faculty of
New Jersey Institute of Technology
in Partial Fulfillment of the Requirements for the Degree of
Doctor of Philosophy in Civil Engineering**

Department of Civil and Environmental Engineering

May 2010

Copyright © 2010 by Navid H. Allahverdi
ALL RIGHTS RESERVED

APPROVAL PAGE

COUPLED SIMULATION OF LOADING AND RESPONSE OF
COLUMNS UNDER EXTREME EVENTS

Navid H. Allahverdi

5/10/10

M. Ala Saadeghvaziri, Dissertation Advisor
Professor, Department of Civil and Environmental Engineering, NJIT

Date

5/10/10

Bruce Bukiet, Committee Member
Associate Professor, Department of Mathematical Sciences, NJIT

Date

5/10/10

C.T. Thomas Hsu, Committee Member
Professor, Department of Civil and Environmental Engineering, NJIT

Date

5/10/10

I. Joga Rao, Committee Member
Associate Professor, Department of Mechanical Engineering, NJIT

Date

5/10/2010

Methi Wecharatana, Committee Member
Professor, Department of Civil and Environmental Engineering, NJIT

Date

BIOGRAPHICAL SKETCH

Author: Navid H. Allahverdi
Degree: Doctor of Philosophy
Date: May 2010

Undergraduate and Graduate Education:

- Doctor of Philosophy in Civil Engineering,
New Jersey Institute of Technology, Newark, NJ, 2010
- Master of Science in Structural Engineering,
Sharif University of Technology, Tehran, Iran, 2003
- Bachelor of Science in Civil Engineering,
Sharif University of Technology, Tehran, Iran, 2000

Major: Civil Engineering

Presentations and Publications:

- A. Joghataie, N. Allahverdi, "Iterative Univariate Optimization of Nonlinear Trusses with Fuzzy Strain Constraints," *Engineering Optimization*, Vol. 36, No. 6, December 2004, pp.677-690.
- N. Allahverdi, X. Wang, M.A. Saadeghvaziri, B. Bukiet, "On Interaction of Strong and Weak Shock Waves with Flexible Plates," *1st International Workshop on Performance, Protection, and Strengthening of Structures under Extreme Loading*, Whistler, Canada, August 20-22, 2007.
- N. Allahverdi, M.A. Saadeghvaziri, "The Effects of Column Shape on Blast-induced Loadings," *under preparation*.

To the memory of my uncles

ACKNOWLEDGMENT

I would like to express my sincere gratitude to my mentor and advisor, Professor M. Ala Saadeghvaziri. This work wouldn't have been possible without his support and supervision. His scholarly enthusiasm has been the driving force in all stages of this work. I am also thankful for his trust in me to let me pursue different research interests.

Also, my appreciation extends to my committee members. Professors Bruce Bukiet, Thomas Hsu, I. Joga Rao, and Methi Wecharatana showed interests in this work and critically reviewed it. Professor William Spillers served in the committee, but sadly left us just weeks before final defense. May he rest in peace.

I have attended lots of graduate level courses offered at NJIT. I have really enjoyed them and they have been instrumental in my research. Among them, I should mention classes offered by Professor Rao. His articulation in making hard-to-grasp subjects understandable is unique. I also benefitted from courses offered by Professors Michael Siegel, David Horntrop, Robert Miura and Peter Petropoulos in the Department of Mathematical Science. Professor Bukiet spent a great deal of time teaching me gas dynamics.

When I came to NJIT, little did I know that I am destined to meet a couple of great friends; Dr. Max Roman, Dr. Amit Banerjee, Dr. Kamyar Malakuti and Bakhtiar Feizi. You are great and I will treasure your friendship. I am also thankful to Dr. Verya Nasri at AECOM. I have been fortunate to have wonderful officemates, Shabnam Darjani, Nick Carlson and Shilan Motamedvaziri - though she is not officially in our office.

Finally, my "infinite" thank goes to my parents, Hana, and Parisa. I am receiving your love, encouragement, and support each and every minute. I can not say enough thank you.

TABLE OF CONTENTS

Chapter	Page
1 INTRODUCTION	1
1.1 Motivation	1
1.2 Objectives and Methodology of The Present Work	3
1.3 Scope of The Work	6
1.4 Blast Loading	9
1.4.1 Free Air Blast	9
1.4.2 Reflection	10
1.4.3 Diffraction:	17
1.5 Blast Scaling	18
1.6 Manuals and Design Aids	21
2 COMPRESSIBLE FLUID	26
2.1 Introduction	26
2.2 Kinematics of Motion, Strain and Stress Measures	26
2.3 Constitutive Equations	31
2.4 Balance Laws	32
2.4.1 Conservation of Mass	33
2.4.2 Conservation of Momentum	33
2.4.3 Conservation of Energy	34
2.5 The Euler's Equations	35
2.5.1 Strong Form of the Euler's Equations	35
2.5.2 Euler's Equations in One-dimension	37
2.5.3 Characteristic Form of the Euler Equations	38
2.6 Thermodynamical Aspects of Euler Equation	39
3 EXPLICIT AND IMPLICIT FINITE ELEMENT	41
3.1 Burger's Equation	41

TABLE OF CONTENTS
(Continued)

Chapter	Page
3.1.1 Linearizing Weak Form and Newton-Raphson Method	42
3.1.2 Spatial Finite Element Discretization	43
3.2 Temporal Discretization	44
3.3 The Euler's Equations	47
4 ASSESSING AUTODYN RESULTS ACCURACY AND LIMITATIONS	50
4.1 Spherical Blast Simulation with Autodyn	50
4.2 ConWep Program	51
4.3 Comparing Autodyn and ConWep	55
4.4 Conclusion	58
5 BLAST LOAD CHARACTERIZATION ON COLUMNS	60
5.1 Fluid Forces on Solid Objects	60
5.2 Fluid Flow Around a Solid Object	62
5.2.1 Supersonic Flow Over a Corner	64
5.3 Flow Field Around Column Sections	67
5.3.1 Qualitative Discussion	67
5.3.2 Quantitative Discussion	71
5.4 Characterizing Blast Loads on Columns	83
5.4.1 Three-Dimensional Simulations	85
5.4.2 Three-Dimensional Simulation Results	86
5.4.3 Proposed Equations	94
6 SINGLE DEGREE-OF-FREEDOM MODEL FOR COLUMNS	100
6.1 Elastic Response of a SDOF to Dynamic Loading	100
6.2 Elastic-Plastic Response of a SDOF to Dynamic Loading	104
6.3 Equivalent SDOF	106
6.4 Elastic Response of Columns	113
7 PERFORMANCE EVALUATION AND RETROFITTING OPTIONS	121

TABLE OF CONTENTS
(Continued)

Chapter	Page
7.1 Background	121
7.2 Damage Assessment	122
7.3 Retrofitting Measures	127
7.4 Material Models	130
7.4.1 Steel Constitutive Model	130
7.4.2 Concrete Constitutive Model	131
7.5 Summary	133
8 CONCLUSIONS	134
8.1 Conclusion	134
8.2 Future Research Directions	137
REFERENCES	139

LIST OF TABLES

Table	Page
1.1 Computer Programs Used in Blast Simulation [19]	6
1.2 Comparing Parameters for Two Similar Blast Waves	20
1.3 Blast Loading Categories	24
3.1 Newton-Raphson Iteration	43
3.2 The θ Family of Time Integration Methods	45
3.3 Newmark Method	47
4.1 JWL Parameters for TNT	52
5.1 Peak Overpressure and Impulse for Circular Column	73
5.2 Peak Overpressure and Impulse for Square Column	77
5.3 Peak Overpressure and Impulse for Rotated Square Column	77
5.4 Parameter Values for Force Equation f	95
5.5 Parameter Values for Impulse Equation i	95
5.6 Simulation Results and Equation Prediction for Circular Section.	97
5.7 Simulation Results and Equation Prediction for Square Section.	98
6.1 Deflection Results for Circular Section.	116
6.2 Deflection Results for Square Columns.	118
7.1 Comparing Elastic and Inelastic Deflections and Impulses	125

LIST OF FIGURES

Figure	Page
1.1 Typical Pressure History for Free Air Blast	9
1.2 Normal Reflection of a Plane Wave	11
1.3 Reflected Pressure Ratio C_p versus Incident Pressure p_s (TM5-1300) . .	14
1.4 Regular Reflection of Incident Shock I	14
1.5 Irregular Reflection	16
1.6 Oblique Reflected Pressure Ratio for Different Incident Angles α_I	16
1.7 Oblique Reflected Scaled Impulse versus Incident Angle α_I	17
1.8 Diffraction of Shock Wave around a Rectangle	18
1.9 Self-Similar Blast Waves	20
1.10 Free Air Blast Parameters versus Scaled Distance	22
1.11 Free Air Burst (top), Air Burst (middle), and Surface Burst (bottom) . .	25
2.1 Motion of A Body	27
2.2 Polar Decomposition of Deformation Gradient \mathbf{F}	28
4.1 Free Air Blast Model	51
4.2 Pressure versus Specific Volume in JWL	51
4.3 Peak Pressure as a Function of Scaled Distance	53
4.4 Scaled Impulse as a Function of Scaled Distance	53
4.5 Scaled Arrival Time and Scaled Duration versus Scaled Distance	54
4.6 Overpressure versus scaled distance.	56
4.7 Scaled Arrival Time versus Scaled Distance.	57
4.8 Scaled Positive Impulse versus Scaled Distance	59
4.9 Autodyn and ConWep Pressure Time Histories	59
5.1 Subsonic and Supersonic Flow Field Around a Rectangular Object [1] . .	63
5.2 Flow Over Concave(a) and Convex(b) Corners.	64
5.3 $\theta - \beta - M$ Curves.	66

**LIST OF FIGURES
(Continued)**

Figure	Page
5.4 Circular Column and Square Columns in 0 and 45° angles-of-attack . . .	68
5.5 Qualitative Flow Field Around a Square Column and Idealized Pressure Distribution	69
5.6 Qualitative Flow Field Around a Rotated Square Column and Idealized Pressure	70
5.7 Circular Column(A), Square Column(B), and Rotated Square Column(C)	72
5.8 Gauge Locations in Circular Column	73
5.9 Shock Wave Propagation Around Circular Column	74
5.10 Shock Wave Propagation Around Circular Column (Continued)	75
5.11 Gauge Locations in Rectangular Column	76
5.12 Shock Wave Propagation Around Square Column	78
5.13 Shock Wave Propagation Around Square Column (Continued)	79
5.14 Gauge Locations in Rotated Square Column	80
5.15 Locations of point a, b, c, d, and e.	80
5.16 Pressure and impulse histories at point “a”	81
5.17 Pressure and impulse histories at point “b”	81
5.18 Pressure and impulse histories at point “c”	82
5.19 Pressure and impulse histories at point “d”	82
5.20 Pressure and impulse histories at point “e”	83
5.21 3D Modeling of Circular Column	84
5.22 3D Modeling of Square Column	84
5.23 Force f (top) and Impulse i (bottom) for Circular Sections with Diameter of 500 mm and Lengths of 3000, 4500, and 6000 mm (denoted as s , m , and h respectively.)	88
5.24 Force f (top) and Impulse i (bottom) for Circular Sections with Diameter of 750 mm and Lengths of 3000, 4500, and 6000 mm (denoted as s , m , and h respectively.)	89

LIST OF FIGURES
(Continued)

Figure	Page
5.25 Force f (top) and Impulse i (bottom) for Circular Sections with Diameter of 1000 mm and Lengths of 3000, 4500, and 6000 mm (denoted as s , m , and h respectively.)	90
5.26 Force f (top) and Impulse i (bottom) for Square Sections with Diameter of 500 mm and Lengths of 3000, 4500, and 6000 mm (denoted as s , m , and h respectively.)	91
5.27 Force f (top) and Impulse i (bottom) for Square Sections with Diameter of 750 mm and Lengths of 3000, 4500, and 6000 mm (denoted as s , m , and h respectively.)	92
5.28 Force f (top) and Impulse i (bottom) for Square Sections with Diameter of 1000 mm and Lengths of 3000, 4500, and 6000 mm (denoted as s , m , and h respectively.)	93
6.1 Impulsive Loading Compared with Resistance Function [16].	102
6.2 Quasi-Static Loading	103
6.3 Shock Spectrum for Triangular Load	104
6.4 Idealized Resistance-Deflection Curve [16]	105
6.5 Actual and SDOF representation	107
6.6 Transformation Factors for Elastic and Plastic Behaviors	110
6.7 Stiffness for beams $k = \frac{\kappa EI}{L^3}$	111
6.8 Circular Column Deflection	115
6.9 Square Column Deflection	117
7.1 Damage Assessment for Different Structural Elements	123
7.2 Damage Index for Square Column for Loading with $z = 0.561$ (top), $z = 0.413$ (middle), and $z = 0.328$ (bottom)	126
7.3 Retrofitted Columns with Plates(A) and Jacket(B)	128
7.4 Deflection for Plate Retrofitted (dash-dot) and Jacket Retrofitted (solid) Compared with Bare Column (grey)	129
7.5 RHT Concrete Model	132

CHAPTER 1

INTRODUCTION

1.1 Motivation

Designing structures to withstand sudden shock loads becomes imperative while more structures are exposed to accidental or deliberate blast loads. Although a great body of work and knowledge has been acquired in designing hardened military structures [2, 5], blast design practice still is not fully comprehended and embraced in civil engineering community; and the need for appropriate codes and guidelines are not fulfilled [10].

In this research, it is attempted to understand and clarify aspects of blast loading and provide practical blast design recommendations. It is understood that following areas need to be further investigated:

- A methodology for designing blast resistant structures
- Estimating blast load for a specific level of threat
- Improving blast response of structures

To better understand blast loading, it is instructive to compare blast loading with earthquake loading which is better known by structural engineers. At first look, both earthquake and blast loads are dynamic loads; however, each has its own time scale. Earthquakes duration is usually in orders of seconds; while blast loads fade in couple of milli-seconds. Accordingly when an earthquake strikes a structure, usually the earthquake lingers enough to engage the entire structure into motion. On the other hand, blast load works in an impulsive manner and the structure may begin reacting while the load has well disappeared.

Secondly, earthquakes most often excite the whole structure no matter how tall or large the structure is; every part of the structure gets affected by inertial forces. On the other hand, blast loads usually have a finite *zone of influence* and they work in a local manner; i.e., the blast load may exert force on a limited number of structural elements. It is noteworthy to mention that the concept of modal analysis and mode shapes - which is extensively useful in earthquake analysis - is not well suited for shock type loading analysis [6].

The local nature of blast loads as compared with global nature of earthquakes suggests a member (local) approach for blast design methodology. As the first step of member approach, the adequacy of members located in the influence zone of loading should be assessed. If there is any likelihood of failure of members, then *progressive collapse analysis* should be performed to evaluate global stability of the structure.

In this research, the emphasis is mostly on the blast loading of isolated structural members and more specifically on column members. In buildings, columns are the most vital element in stability of the whole structure and failure of columns may jeopardize the integrity and load-path redundancy of the building. Specifically, in this research, emphasis has been put on facade columns located on the perimeter of tall buildings. These facade columns do not have any bracing or lateral supports.

Another lesson that can be learned from earthquake design methodology is the idea of protection (shielding) rather than hardening (strengthening). The notion of protection is quite established in earthquake design. For instance, using base isolation in reducing the seismic demand of structures is pretty common. Similarly, the idea of protecting structural members against blast has been pursued through using *sacrificial* or *protective* layers. For example, metal foams have been placed in front of concrete plates as a protective measure; however, there is no definite answer on the ability of metal foams in protecting structures. Ironically, some experimental

tests show metal foams have in fact amplified the energy and impulse imparted to the structure [9, 20]. The efficacy of using metal foams is still under research and it remains to be answered.

The avenue which seems more practical to pursue in mitigating the blast load is to dissect the blast wave nature and its interaction with structural members and accordingly to come up with members that are more blast resistant. As it is shown, columns cross-sectional shape and size can markedly affect the pressure and impulse experienced by columns [18, 21]. So, we will examine different column shapes under similar scenarios of blast and evaluate blast wave reflection and diffraction around columns in order to find the column with less amount of pressure and impulse.

1.2 Objectives and Methodology of The Present Work

The main objectives of this study can be summarized as following:

Estimating Blast Load on Columns: pressure and impulse distributions on columns with different cross section and size will be quantified through simulations. The results of this task serve two purposes; 1) determining blast loading as a function of member cross section shape and size and 2) comparing and finding cross sectional shapes that experience less amount of force.

In characterizing the blast intensity on members, *scaled distance* $z = R/w^{1/3}$ is employed. R and w are stand-off distance and weight of the charge, respectively; smaller z represents the more intense blasts. Based on the results of this task, proper equations will be suggested to approximate blast force and impulse acting on columns for a range of scaled distances.

Response of Columns to Blast Loading: In this task, three dimensional response of columns with elastic behaviors as well as true nonlinear inelastic behavior

have been investigated. Different type of damage or failure including shear and flexural modes have been examined. Additionally, for elastic range of response, an equivalent single-degree-of-freedom model has been presented to approximate the response of columns to blast loading. Furthermore, the efficacy of retrofitting measures for blast response mitigation of columns has been evaluated.

The main tool in this study is using numerical modelings. Computer simulations can be useful in blast design. While computer simulations can not replace experiments, they can provide valuable insights on the physics of blast loading. Performing blast tests is very difficult and expensive. It needs considerable amount of expertise, and requires special facilities. Instrumentations and measurements of blast parameters and structural responses necessitate high performance sensors. Also, the very abrupt nature of blast phenomenon (a couple of milli-seconds) makes visual observation of events in any given test virtually impossible, unless using high-speed cameras. All mentioned reasons render numerical simulation of blast loading very appealing.

Also, There are not analytical methods for problems involving complicated geometries where multiple reflection, or diffraction occurs; the only way to study such problems is to resort to computational methods.

Computational methods in the area of blast effects prediction are generally divided into: (1) those used for prediction of blast loads (2) those for determining structural response to the loading. The former is achieved through computational fluid dynamics (CFD) codes, while the latter is carried out by computational solid mechanics (CSM) codes. A current trend is to couple CFD and CSM codes in order to obtain simulations which consider the mutual interactions between two physics. By accounting the motion and deformation of structures, a more accurate prediction of blast wave is achieved and vice versa.

A number of computer programs used in blast prediction and structural response simulations is reported in Table 1.1 [19]. Most of these programs use a first-principle approach which they solve conservation laws in conjunction with material constitute models. On the other hand, there a number of programs that employ a semi-empirical approach. These programs usually contain equations based on data fitting of a collection of data obtained from experimental tests.

As seen in Table 1.1, commercially available codes that can couple solid and fluid solvers are Autodyn and LS-DYNA. Blast simulations in this research will be performed with Autodyn. “Autodyn is an explicit analysis tool for modeling nonlinear dynamics of solids, fluids, gas, and their interaction” [12]. Autodyn is part of Ansys Workbench suite. Explicit time integration - which is used in Autodyn - is very suitable for wave propagation phenomena; however, the numerical stability of explicit schemes requires satisfying CFL condition for each element [11].

Explicit programs once used to be known as hydrocodes [23]; since they were used mostly to model fluids without shear strength; i.e. only equation of state were included. However, current explicit programs including Autodyn, and LS-Dyna [8] have an extensive library for strength and failure of solid materials in addition to equation of state models. For instance, Autodyn is capable of simulating material behaviors such as strain-rate hardening, pressure hardening, tensile failure and material erosions.

For simulating blast wave propagation in air Euler equation should be solved [15]. Euler equation governs the behavior of inviscid compressible fluids like air. Autodyn has two different solver to handle Euler equation. They are namely Euler Multi-Material solver and Ideal-gas solver. Euler Multi-Material (MM) uses Godunov method and Ideal-gas solver adopts “Flux Corrected Transport” (FCT) technique which was first introduced by Book and Boris [14].

In Autodyn both *Eulerian* and *Lagrangian* meshes can be used. Also, it is possible to make models which contain both Eulerian and Lagrangian parts. This option is very useful in modeling solid parts with Lagrangian mesh which are coupled with Eulerian mesh for air.

Table 1.1 Computer Programs Used in Blast Simulation [19]

Name	Purpose	Type	Corporate Author
BLASTX	Blast prediction	Semi-empirical	SAIC
ConWep	Blast prediction	Semi-empirical	US Army Corps of Engineers
CTH	Blast prediction	First-principle	Sandia National Laboratories
FEFLO	Blast prediction	First-principle	SAIC
FOIL	Blast prediction	First-principle	Applied Research Associates,
HULL	Blast prediction	First-principle	Orlando Technology, Inc.
SHARC	Blast prediction	First-principle	Applied Research Associates
ABAQUS	Structural response	First-principle	Simulia
DYNA3D	Structural response	First-principle	Lawrence Livermore National Lab.
FLEX	Structural response	First-principle	Weidlinger Associates
ALE3D	Coupled analysis	First-principle	Lawrence Livermore National Lab.
ALEGRA	Coupled analysis	First-principle	Sandia National Laboratories
AUTODYN	Coupled analysis	First-principle	ANSYS, Inc.
LS-DYNA	Coupled analysis	First-principle	Livermore Software Tech. Corp
FUSE	Coupled analysis	First-principle	Weidlinger Associates

1.3 Scope of The Work

In the remainder of this chapter, a brief review of the blast loading has been presented. This review covers the current state of practice on blast load estimation. This also includes methods and tools such as formulas, or graphs used in estimating blast loading. Also, available technical manuals on the subject has been mentioned.

Chapter 2 covers the theory of compressible fluids. This chapter explains the *balance laws* of mechanics including conservation of mass, momentum, and energy to derive *Euler's equations*. Euler's equations govern the behavior of compressible and inviscid fluid flows. Different forms of the Euler's equations have been discussed.

This chapter serves as a reference for most of the nomenclatures and symbols used in the manuscript.

Chapter 3 documents the finite element techniques used in solving differential equations like Euler's equations. The chapter discusses methods for *spatial* and *temporal* discretization of equations. In temporal discretization, *implicit* and *explicit* time integration methods are discussed. The model equation which is discretized in this chapter is *Burger's equation*. Burger's equation is very similar to Euler's equations. In fact, Euler's equations is a combination of three Burger-like equations.

Chapter 4 reports the results of one-dimensional free air blast simulations performed with Autodyn. The results include blast parameters like peak overpressure, impulse, and arrival times. The results obtained with Autodyn are compared with other benchmark results. In this chapter, capabilities and limitations of the Autodyn in modeling detonation as well as its subsequent wave propagations are mentioned.

Chapter 5 continues the blast load simulations when solid obstacles like structural columns are present in the flow field. The ultimate goal of this chapter is to estimate the force and impulse experienced by columns in blast events and to propose appropriate equations that can predict force and impulse. Before estimating force and impulse on columns, first a qualitative discussion on the pressure distribution around columns with circular and square shapes is presented. In the discussion, it is tried to explain the pressure distribution around different column's section via using concepts of *shock wave reflection* and *expansion wave*. The qualitative discussion is followed by a quantitative Autodyn simulations on pressure distribution.

At the end of the chapter 5, the results for a set of three-dimensional simulations on columns with circular and square sections are presented. The force and impulse experienced by columns are obtained from the simulation results. Next, proper equations are derived for both force and impulse on columns as functions of the column

size (section size and height) as well as blast intensity. Scaled distance z is used to represent the blast intensity. The proposed equations are obtained via performing curve-fitting techniques on the simulation results. The proposed equations can be an indispensable tool in blast design practices.

Chapter 6 has been devoted to study the elastic structural behavior of columns in blast events. In this chapter, the concept of reducing a column to an equivalent *single-degree-of-freedom* mass-spring system is discussed. This is done through using *transformation factors* which were introduced by Biggs [3]. Biggs proposed the transformation factors through assuming arbitrarily shape functions or mode shapes. In his work, load factors for concentrated load as well as uniformly distributed loads are mentioned and the designer should make assumptions on the blast load distributions. The work on this chapter builds upon the Biggs work in the way that the transformation factors has been refined by using the deflection results obtained from simulations performed in previous chapter. The transformation factors have been back calculated from actual simulation results. Once, the factors are obtained, the structural response of columns (deflection) can be estimated. The proposed transformation factors are customized for blast load distribution and no load distribution assumptions need to be made, since simulations consider the actual blast loading.

Chapter 7 concludes this research through assessing the actual performance of concrete columns in blast events. In this chapter true nonlinear behavior of concrete materials is used to evaluate the potential damage or failure sustained by columns. For the case of under-performing or insufficient columns, suitable upgrade or retrofitting measures are discussed to mitigate the response of such columns.

1.4 Blast Loading

Here, the basic nature of blast wave propagation is mentioned with reference to blast loading. Common phenomena such as Free Air Blast, Reflection and Diffraction of blast waves will be explained. This section summarizes current available tools and methods for estimating blast loading.

1.4.1 Free Air Blast

When a spherical or point explosion occurs in atmosphere, the characteristics of blast wave including pressure, and impulse at an arbitrary location are functions of standoff distance R from the center of the charge and time t . If employing a pressure transducer and measuring the pressure history, the typical pressure reading is very similar to Figure 1.1.

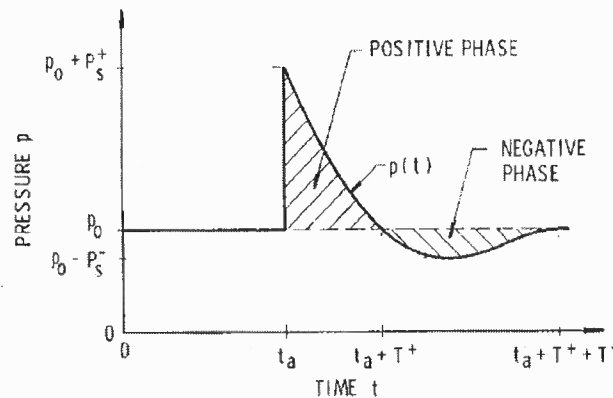


Figure 1.1 Typical Pressure History for Free Air Blast

At the beginning, before any pressure disturbance reaches to the transducer, it reads the ambient pressure p_0 . It will take time T_a for the shock wave to travel the distance R with shock velocity of U_s . Upon arrival time of T_a , pressure jumps to $p_0 + p_s^+$ in no time; this is the instant which the point is *shocked-up*. Afterwards, pressure starts to decay during positive phase T^+ until transducer reads ambient

pressure once again. Next, pressure drops below the ambient pressure to $p_0 - p_s^-$ and causes a relative vacuum in negative phase duration T^- . At the end, pressure returns to ambient pressure once again.

The maximum positive overpressure p_s^+ is referred to as *peak incident overpressure* or just the *peak overpressure*. Usually, p_s^+ is larger than p_s^- by orders of magnitude and we are more concerned about positive overpressure. For convenience, the \pm signs will be omitted and positive overpressure will be shown as p_s unless otherwise noted.

It is useful to define *incident impulse* $i_s(t)$ as the area under overpressure p_s time history shown in Figure 1.1:

$$i_s(t) = \int_{T_a}^t p_s(t) dt$$

The maximum amount of incident impulse corresponds to the end of the positive phase; afterwards the negative overpressure reduces the impulse.

Free air blast is usually obstructed by objects such as buildings. When a shock wave encounters any solid objects or dense media, it *reflects from* the object as well as *diffracts around* it. It is imperative to study shock wave reflection and diffraction patterns in order to evaluate the amount of pressure experienced by the object (structure). In the following sections, a brief review of reflection and diffraction of blast wave is presented.

1.4.2 Reflection

When a shock wave impinges on a rigid (fixed) wall, the forward-moving air particles are brought to rest at the face of the wall. As the velocity of each arriving layer of air

is arrested; they are stacked up on each other and resulted in a highly compressed air layers adjacent to the wall. Compressed air, in turns, fires back and generates a reflected shock wave that propagates away from the wall with velocity U_r . The reflected overpressure p_r on the wall has higher magnitude than the incident overpressure.

Normal Reflection of A Plane Wave: the simplest type of reflection is *normal* or *head-on reflection* in which the shock wave front is parallel to the wall. As depicted in Figure 1.2, the incident wave I is approaching the wall with velocity U_s and leaving behind the shocked state pressure p_s , density ρ_s , and particle velocity u_s ; s subscripts denote the shocked state while zero subscripts refer to ambient state which are p_0 , ρ_0 , and $u_0 = 0$. The shocked state variables are identical and equal to those of free air shock wave propagation. As incident shock wave hits the wall and consequently reflects away, the reflected state contains reflected pressure p_r , density ρ_r , and velocity $u_r = 0$. Figure 1.2 on the right side shows the reflected wave. Reflected shock wave front R moves away from the wall with velocity U_r into the flow field which has been previously compressed with the incident front. The particle velocity u_r in reflected region is zero; however, the pressure, density, and temperature of reflected region are considerably magnified as compared to the incident shocked state.

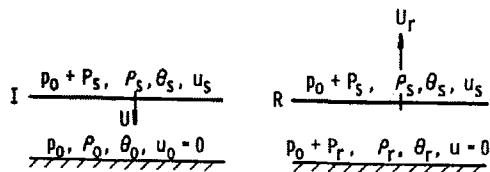


Figure 1.2 Normal Reflection of a Plane Wave

In normal reflection, it is possible to obtain peak reflected overpressure p_r in

terms of peak incident overpressure p_s and ambient pressure p_0 in air:

$$p_r = p_s \frac{(3\gamma - 1) p_s + 4\gamma p_0}{(\gamma - 1) p_s + 2\gamma p_0} \quad (1.1)$$

in which γ is the *specific heats ratio* for air. In order to derive the above equation, conservation of mass, momentum, and energy have been utilized between the two states of air as detailed in [7]. For air at sea level, γ is equal 1.4. Substituting for $\gamma = 1.4$ in Equation 1.1 results in following:

$$p_r = 2p_s \frac{4p_s + 7p_0}{p_s + 7p_0} \quad (1.2)$$

Also, it is convenient to define *reflected impulse* $i_r(t)$ as time integration of reflected overpressure p_r :

$$i_r(t) = \int_0^t p_r(t) dt$$

In general, one can define *reflected pressure ratio* C_p and *reflected impulse ratio* C_i as following:

$$C_p = \frac{p_r}{p_s}$$

$$C_i = \frac{i_r}{i_s}$$

These ratios are very useful when reflected pressure p_r and reflected impulse i_r are sought for design purposes. For the special case of normal reflection the theoretical value for C_p can be derived from Equation 1.2 as:

$$C_p = 2 \frac{4p_s + 7p_0}{p_s + 7p_0} \quad (1.3)$$

Finding limits of above equation for extreme cases of very large and very small overpressure p_s is easy. For the strong incident overpressure, i.e. large p_s relative to

p_0 , reflected pressure ratio C_p tends to an upper-bound of 8; while for weak incident pressures, C_p approaches 2.

$$2 \leq C_p \leq 8 \quad (1.4)$$

The lower-bound of 2 for C_p clearly represents the linear reflection which corresponds to acoustic fluid model. The upper bound of 8 is due to the compressibility of air as discussed in [13]. It is worth mentioning that higher values of C_p , up to 20, have been measured in experiments. In Equation 1.2, the *specific heats ratio* γ for air has been assumed as a constant value of $\gamma = 1.4$; however in reality γ can change in high temperature and pressure. In fact in high temperatures γ start decreasing as a result of dissociation and ionization of gas molecules [16]. TM5-1300 manual [2] provides reflected pressure ratio C_p for a wide range of incident pressure p_s for normal reflection which is also shown in Figure 1.3. Based on this graph C_p can reach up to 12 in extreme pressures.

Oblique Reflection of A Plane Wave When the shock front is impinging on a wall at angle α_I with respect to the wall, depending on the angle α_I two different reflection scenarios may happen, namely *regular reflection* and *irregular reflection*. Detailed accounts of each type of reflections are described in following sections.

Regular Reflection Regular reflection happens when α_I is smaller than a specific critical angle α_{cr} . In regular reflection three different regions can be identified as shown in Figure 1.4. The incident shock front I and reflected shock front R meet on the surface of wall and they distinguish three regions. The three regions are un-shocked (ambient), incident shock region, and reflected shock regions. Reflected shock front makes an angle of α_R which is not necessarily equal to α_I and depends on the strength of the incident shock. Following facts hold for regular reflections:

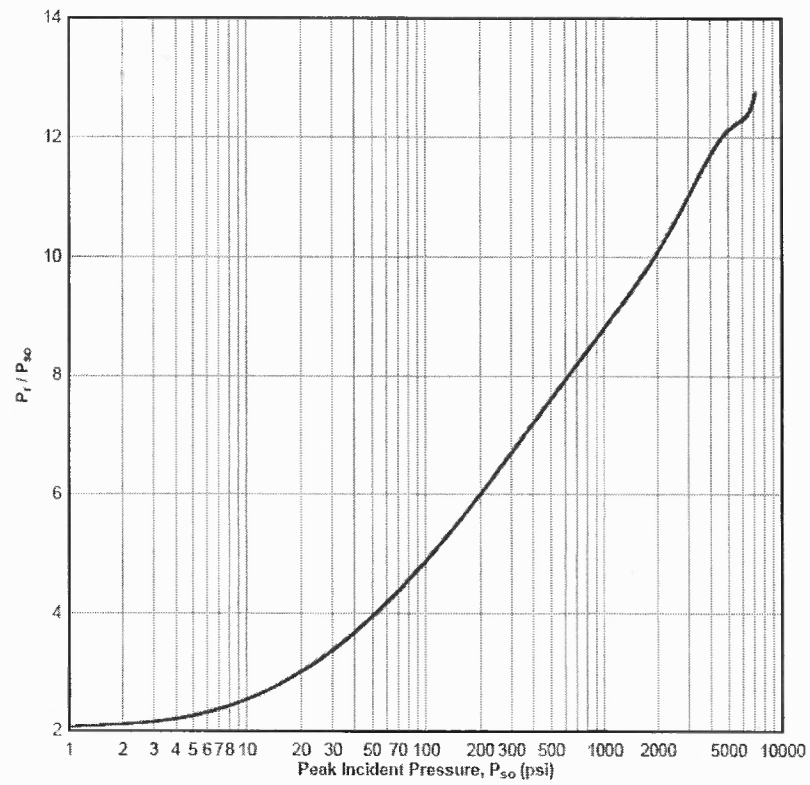


Figure 1.3 Reflected Pressure Ratio C_p versus Incident Pressure p_s (TM5-1300)

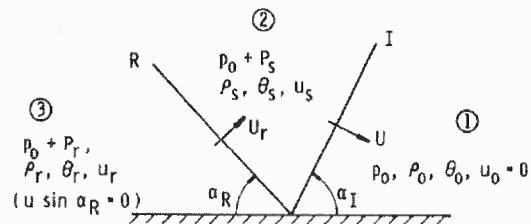


Figure 1.4 Regular Reflection of Incident Shock I

1. Normal reflection is a special case of regular reflection in which $\alpha_I = 0$.
2. For an incident shock with infinite strength, $\alpha_{cr} = \sin^{-1}(1/\gamma)$; in the limit of vanishing shock strength $\alpha_{cr} = 90^\circ$, i.e. all reflections are regular for low strength shocks.
3. The angle of reflection α_R is an increasing monotonic function of the α_I .

The properties of oblique shock reflection listed above are quite different than corresponding characteristics of acoustic wave reflection. In acoustic limits, regular reflection occurs regardless of the angle of incidence α_I ; also, reflected pressure is twice the incident pressure for all values of α_I ; i.e. $C_p = 2$. Finally, reflected shock angle is equal to incident shock angle $\alpha_I = \alpha_R$

Irregular Reflection (Mach Reflection): As discussed in preceding section, regular reflection occurs when α_I is smaller than α_{cr} . In situations where α_I is larger than α_{cr} *irregular reflection* develops. In regular reflection, there are three shock fronts, namely *incident* I, *reflected* R, and *Mach stem* M as well as one *slipstream* ST as shown in Figure 1.5. This is different with regular reflection in which only two shocks are discernible namely incident and reflecting. In addition to incident and reflecting shocks, irregular reflection gives rise to another shock which is called Mach stem *M*. The point of intersection of shock fronts is called *triple point* “T”. Triple point is not necessarily located on the reflecting surface. Whether the triple point is approaching or retreating or moving parallel to the reflecting surface, different types of irregularity can be identified [7]. In Figure 1.5 triple point moves along path “AB”.

Reflected pressure and reflected scaled impulse for different values of incident angle have been shown in Figures 1.6, and 1.7 respectively.

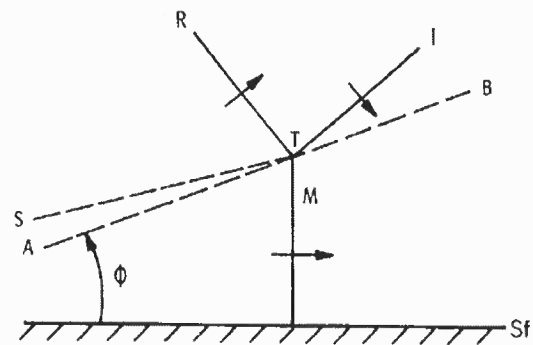


Figure 1.5 Irregular Reflection

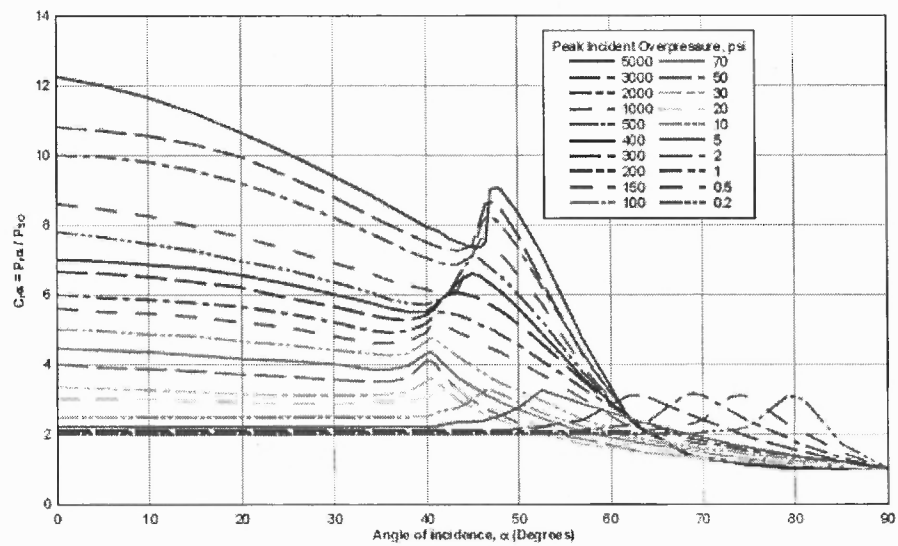


Figure 1.6 Oblique Reflected Pressure Ratio for Different Incident Angles α_I

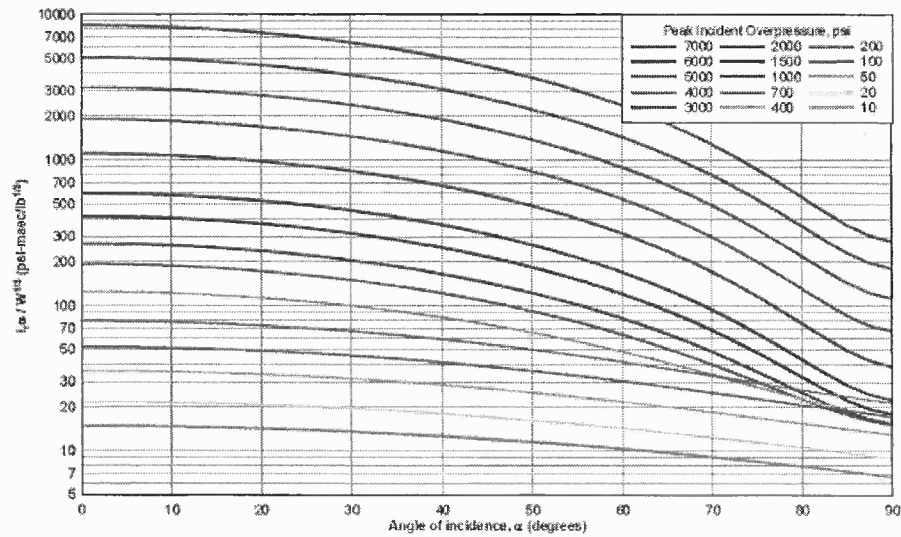


Figure 1.7 Oblique Reflected Scaled Impulse versus Incident Angle α_I

In reflected pressure diagram, it can be observed that there is a change in the trend of curves approximately between 40° to 50° . This can be assigned to the transition from regular reflection regime to irregular reflection as incident angle α_I increases. Critical reflection angle α_{cr} for air with specific heats ratio $\gamma = 1.4$ is $\alpha_{cr} = \sin^{-1}(1/1.4) \approx 45^\circ$ for strong shocks.

1.4.3 Diffraction:

When a shock front encounters a body with finite size, in addition to reflection, the shock front also diffracts around the object. Diffraction is a very complicated process and it directly depends on the shape of the object. In order to explain the diffraction, a very simple case of impinging of a plane wave on a rectangle is depicted in Figure 1.8. At the two corners of the rectangular object, shock wave goes through *expansion fans* and loses its strength considerably. Also, relief waves (rarefaction waves) propagate to the front of the rectangular object and decrease high reflected pressures experienced in the front.

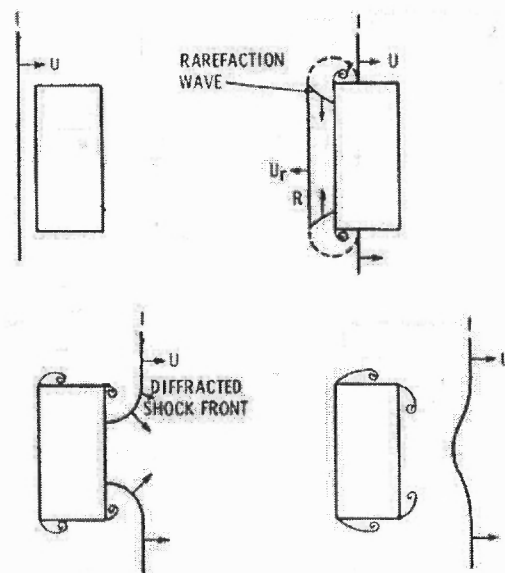


Figure 1.8 Diffraction of Shock Wave around a Rectangle

Diffraction becomes imperative when determining pressure experienced by structural members with finite sizes including slabs, walls, and columns. Unlike reflection, there are not available formulas or charts to determine blast parameters for diffraction. In Chapter 5, blast loading for columns with different cross sectional shape and size has been elaborated.

1.5 Blast Scaling

The idea of *scaling* or *dimensional analysis* is to obtain dimensionless quantities and reduce the number of parameters that a physical model depends on. Experimental studies of blast wave are often difficult, and expensive – particularly when conducted on a large scale. As a result, blast scaling is an appealing way to widen or extend the applicability of a limited number of tests to other cases using the idea of *similarity* of tests.

Performing a dimensional analysis for blast parameters including pressure p ,

and a stand-off distance R for a specific explosives which contains stored chemical energy E , it is possible to get a non-dimensionalized pressure parameter π as:

$$\pi = \frac{p}{E/R^3}$$

or it is possible to express pressure p as a function of E/R^3 , or $p = f(E/R^3)$. The quantity $R/E^{\frac{1}{3}}$ is known as *scaled distance* z ; so pressure can be expressed as a function of inverse of scaled distance $p = g(\frac{1}{z^3})$. It is worthy to mention the smaller the scaled distance is, the stronger the blast wave is. This scaling of parameters is known as *cube-root scaling*. It was first formulated by B. Hopkinson in 1915 and hence sometimes it is referred to as *Hopkinson scaling*. Cube-root scaling reads as:

“Self-similar blast (shock) waves are produced at identical scaled distances z , when two explosive charges of similar geometry and the same explosive composition, but of different size, are detonated in the same atmosphere.”

The chemical energy E stored in explosives release during detonation phase and is proportional with the weight of explosive; it is very common to use equivalent weight of TNT w instead of energy E in defining scaled distance z :

$$z = \frac{R}{w^{\frac{1}{3}}}$$

As an example of two self-similar blasts, two different charges with diameter d and kd will be detonated and blast parameters are monitored at stand-off distance R and kR as shown in Figure 1.9. It is easy to show that scaled distances are equal for both cases;

$$\frac{z_1}{z_2} = \frac{R/d}{kR/kd} = 1$$

blast parameters for each test are shown in Table 1.2. As seen, pressure and velocity

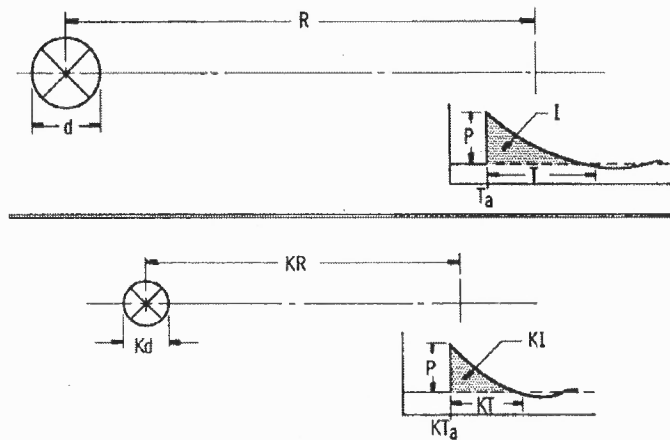


Figure 1.9 Self-Similar Blast Waves

Table 1.2 Comparing Parameters for Two Similar Blast Waves

Blast parameters	Case 1	Case 2
Charge diameter	d	kd
Stand-off distance	R	kR
Scaled distance, z	$R/w_1^{\frac{1}{3}}$	$kR/kw_2^{\frac{1}{3}}$
Peak pressure	p_s	p_s
Time of arrival	T_a	kT_a
Duration	T_s	kT_s
Impulse	I_s	kI_s
Shock velocity	U_s	U_s
particle velocity	u_p	u_p

quantities are self-similar (unchanged) in both cases; however, temporal parameters and impulses have been changed by a factor k . Note that $k = kd/d = w_2^{\frac{1}{3}}/w_1^{\frac{1}{3}}$.

The validity of cubic-root scaling law has been demonstrated through experimental tests. It has been reported that there has been a very good agreement between blast data obtained during field tests with 5-, 20-, 100-, and 500-ton TNT detonation when scaled to 1-lb TNT charge [5].

Blast Parameters The most common way to represent blast parameters is through adopting cube-root scaling law. In this way scaled parameters are:

$$z = R/w^{\frac{1}{3}}; \text{ scaled distance}$$

$$\tau = t/w^{\frac{1}{3}}; \text{ scaled time}$$

$$\xi = I/w^{\frac{1}{3}}; \text{ scaled impulse}$$

As mentioned, temporal parameters like time of arrival and duration are not similar in a self-similar blast. However, *scaled time* and *scaled impulse* will be similar (unchanged). Based on cube-root scaling, pressure p , scaled time τ , scaled impulses ξ and velocities become only a function of scaled distance z .

$$p = p(z)$$

$$\tau = \tau(z)$$

$$\xi = \xi(z)$$

$$U = U(z)$$

In Figure 1.10, blast parameters for positive phase of free air blast are shown as a function of scaled distance z .

1.6 Manuals and Design Aids

In this section, a quick overview of the manuals and design aides which are available in public domain is presented.

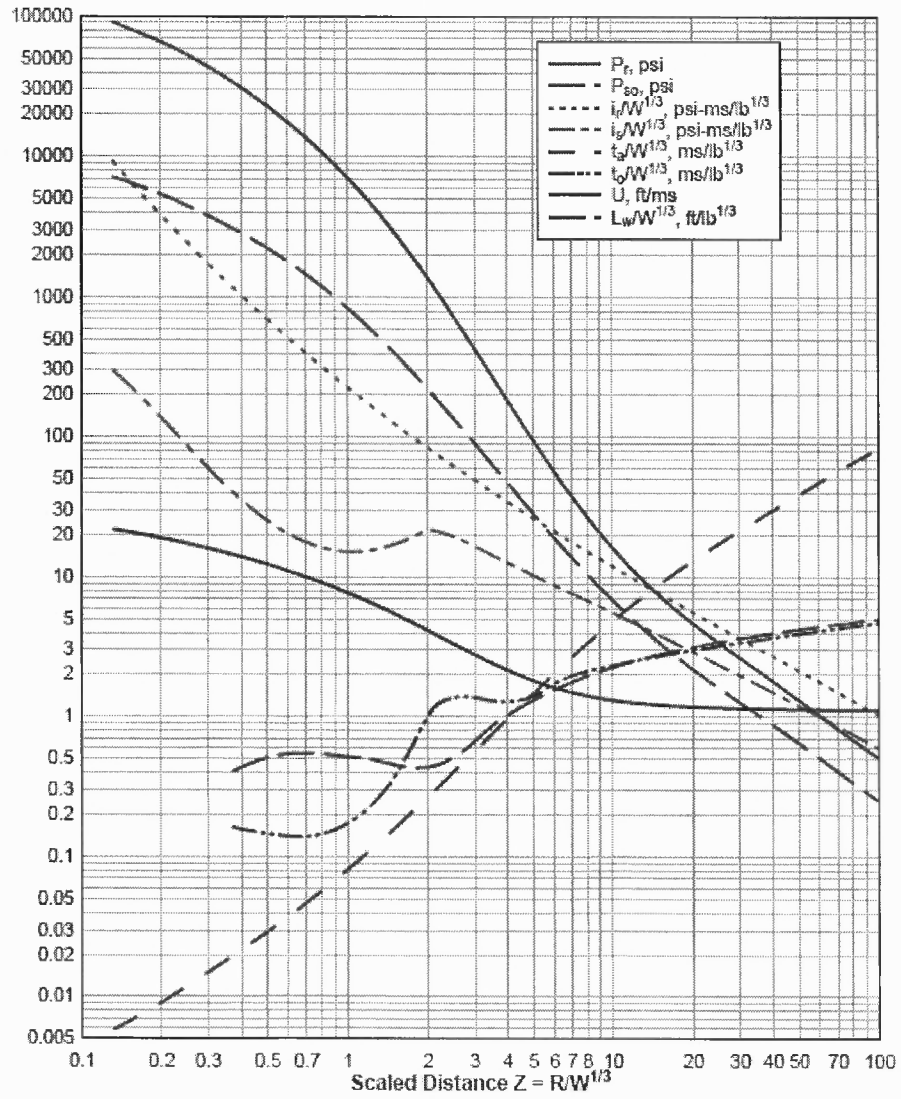


Figure 1.10 Free Air Blast Parameters versus Scaled Distance

UFC 3-340-01 (TM5-855-1) This manual is on “Design and Analysis of Hardened Structures to Conventional Weapons Effects”. It contains chapters on air blast, fire, incendiary and chemical agents, loads on structures, and auxiliary systems (piping, air ducting, and electrical cable); in its appendix, graphs are provided to determine blast parameters versus scaled distances; ConWep program adopts these graphs for blast parameter calculations.

UFC 3-340-02 (TM5-1300) Among first technical blast design manuals is “Structures to Resist the Effects of Accidental Explosions”. This manual was prepared by “Joint Departments of the Army, the Navy, and the Air Force” and is known as TM5-1300. This manual serves structural engineers in estimating blast loading as well as analyzing and designing of concrete and steel military protective structures under blast loads.

TM5-1300 was originally published in 1969 and later revisions released in 1971, and 1990. Finally, TM5-1300 was incorporated in Unified Facilities Criteria (UFC) with minor modifications in 2008 and is now referred to as UFC 3-340-02.

This totally contains six chapters on items including (1) blast, fragment, and shock-loading; (2) principles of dynamic analysis; (3) reinforced concrete and structural steel design; and (4) a number of special design considerations, including information on connections, shock motion tolerances and fragility, shock isolation devices, design criteria for glazing, and design loads for underground structures.

This manual recognizes two types of explosions namely, *confined (internal)* and *unconfined (external)* explosions based on whether the explosive is located in a confined area or an open area. Furthermore, confined explosion is divided to *fully confined*, *partially confined*, and *fully vented*. Herein, we are only concerned about unconfined explosions since usually buildings are more exposed to outdoor threats rather indoor

explosions.

Unconfined explosion is further divided to *free-air burst*, *air burst* and *surface burst* depending on the location of explosive charges with respect to ground and whether ground reflection occurs. Figure 1.11 shows all three types of unconfined explosions.

In free air burst, the propagating shock wave strikes the target structure without intermediate amplification from ground reflections. Air burst happens when ground reflections of the initial shock wave occurs prior to the arrival of the blast wave. Air burst is usually limited to an explosion which occurs at two to three times the height of a one or two-story building.

Surface burst explosions will occur when the detonation is located close or on the ground so that the initial shock is amplified at the point of detonation due to the ground reflections.

For each type of explosions appropriate loading graphs are presented in the manual. These graphs provide blast wave parameters including pressure, impulse, time-of-arrival, duration time for a range of scaled distances. Table 1.3 summarizes different types of blast environments along with applicable pressure loads.

Table 1.3 Blast Loading Categories

Explosion	Confinement	Pressure
Unconfined	1. Free Air Burst	Unreflected
	2. Air Burst	Reflected
	3. Surface Burst	Reflected
Confined	4. Fully Vented	Internal Shock, Leakage
	5. Partially Confined	Internal Shock and Gas, Leakage
	6. Fully Confined	Internal Shock and Gas

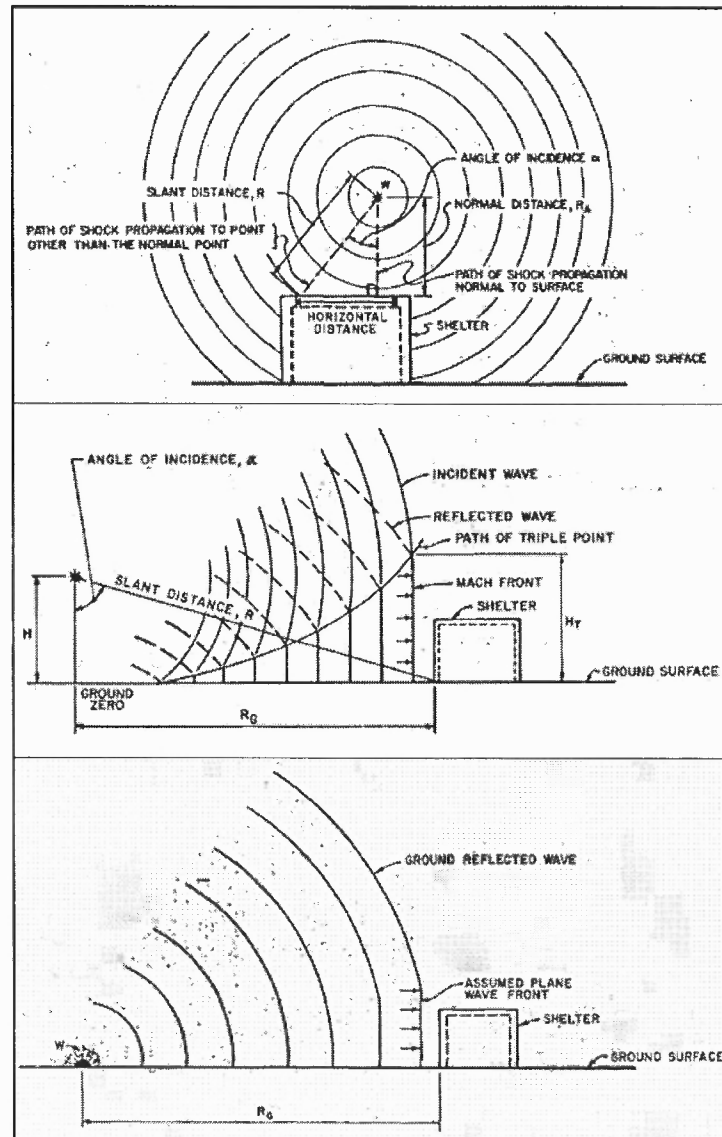


Figure 1.11 Free Air Burst (top), Air Burst (middle), and Surface Burst (bottom)

CHAPTER 2

COMPRESSIBLE FLUID

2.1 Introduction

In this chapter, motion of a body along with the balance laws of mechanics are described. The balance laws are used to obtain the Euler's equations. Euler's equations governs the wave propagation in a compressible and inviscid medium like air. It is attempted to introduce most of the nomenclatures used throughout the script in current chapter. It is tried to reserve bold capital letters for tensorial quantities; while bold small letters usually denoting vectorial quantities.

2.2 Kinematics of Motion, Strain and Stress Measures

As shown in Figure 2.1, let a material body occupy space κ_0 at time $t = 0$; and κ_t at a later time like $t = t$. The motion $\mathbf{x} = \mathcal{X}(X, t)$ is a one-to-one mapping for each particle X and its current location $\mathbf{x} = (x_1, x_2, x_3)$ in Euclidean space. Usually, particle X is *labeled* with its Cartesian coordinates at $t = 0$ which is $\mathbf{X} = (X_1, X_2, X_3)$.

$$\mathbf{x} = \mathcal{X}(\mathbf{X}, t) \tag{2.1}$$

There are two ways to describe the motion of the body in terms of basic independent variables. First, when \mathbf{X} and t are selected as variables then the *Lagrangian* description or *material* or *referential* description is used; however, adopting \mathbf{x} and t as independent variables, results in *spatial* or *Eulerian* description. For example, velocity and acceleration in Lagrangian description is defined as:

$$\mathbf{V}(\mathbf{X}, t) = \frac{\partial \mathcal{X}(\mathbf{X}, t)}{\partial t} \tag{2.2}$$

$$\mathbf{A}(\mathbf{X}, t) = \frac{\partial^2 \mathcal{X}(\mathbf{X}, t)}{\partial t^2} \tag{2.3}$$

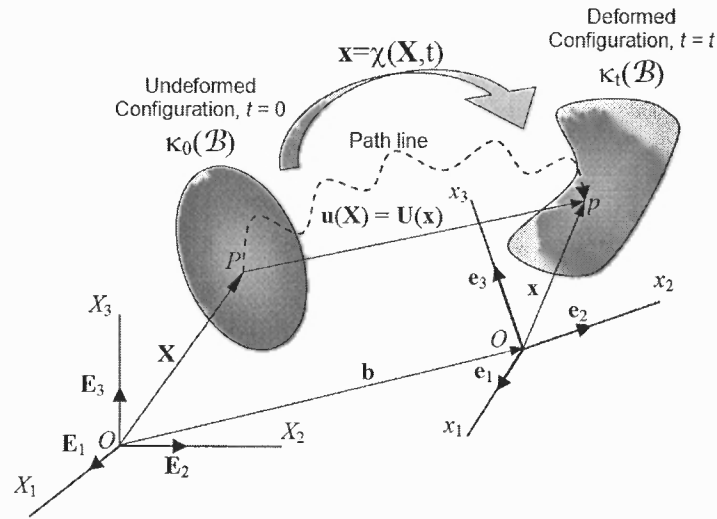


Figure 2.1 Motion of A Body

while, in Eulerian description, velocity and acceleration are:

$$\mathbf{v}(\mathbf{x}, t) = \mathbf{V}(\mathcal{X}^{-1}(\mathbf{x}, t), t) \quad (2.4)$$

$$\mathbf{a}(\mathbf{x}, t) = \mathbf{A}(\mathcal{X}^{-1}(\mathbf{x}, t), t) \quad (2.5)$$

The *deformation gradient* tensor \mathbf{F} is defined as the gradient of the motion:

$$\mathbf{F} = \frac{\partial \mathcal{X}(\mathbf{x}, t)}{\partial \mathbf{X}}. \quad (2.6)$$

Using *polar decomposition theorem*, it is possible to decompose \mathbf{F} into product of a proper orthogonal tensor \mathbf{R} and a symmetric positive-definite tensor \mathbf{U} , or \mathbf{V} as:

$$\mathbf{F} = \mathbf{R}\mathbf{U} = \mathbf{V}\mathbf{R} \quad (2.7)$$

the physical interpretation of Equation 2.7 is motion can be locally seen as a pure stretch followed by a rotation or equivalently a rotation followed by a pure stretch. A pictorial representation of the polar decomposition is shown in Figure 2.2.

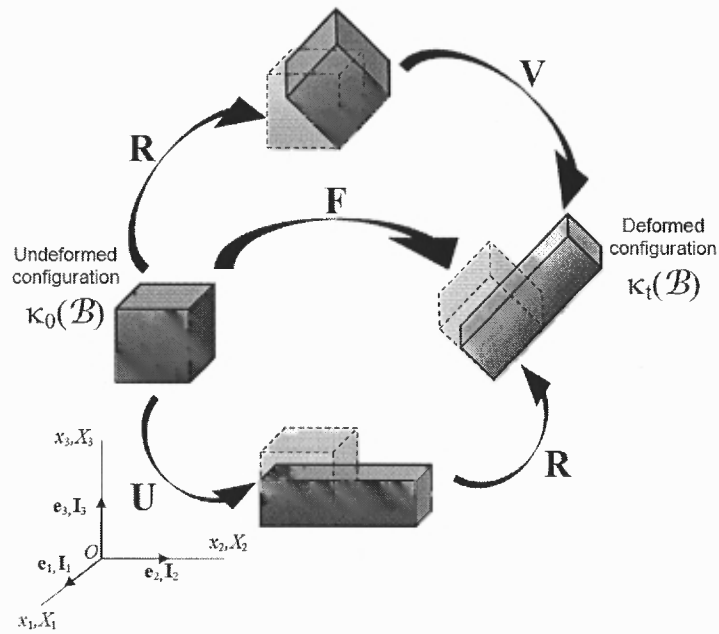


Figure 2.2 Polar Decomposition of Deformation Gradient \mathbf{F}

Left Cauchy-Green stretch tensor \mathbf{B} as well as *Right Cauchy-Green stretch tensor* \mathbf{C} are defined as:

$$\mathbf{B} = \mathbf{V}^2 = \mathbf{F}\mathbf{F}^T \quad (2.8)$$

$$\mathbf{C} = \mathbf{U}^2 = \mathbf{F}^T\mathbf{F} \quad (2.9)$$

It is useful to define the *spatial velocity gradient tensor* as:

$$\mathbf{L} = \frac{\partial \mathbf{v}}{\partial \mathbf{x}} \quad (2.10)$$

velocity gradient is related to deformation gradient through following:

$$\mathbf{L} = \dot{\mathbf{F}}\mathbf{F}^{-1} \quad (2.11)$$

\mathbf{L} can be decomposed into its symmetric part \mathbf{D} which represents *deformation-rate*

tensor and its skew-symmetric part \mathbf{W} called *spin tensor*.

$$\mathbf{L} = \mathbf{D} + \mathbf{W} \quad (2.12)$$

The deformation rate, \mathbf{D} characterizes the instantaneous rate of *distortion*. The spin tensor, \mathbf{W} represents the instantaneous rate of *rigid-body rotation*. Motions in which $\mathbf{W} = 0$ are called *irrotational*.

Strain tensor: The *Green-St Venant* or *Green-Lagrange* strain in Lagrangian description is defined as:

$$\mathbf{E} = \frac{1}{2} \frac{d\mathbf{x} \cdot d\mathbf{x} - d\mathbf{X} \cdot d\mathbf{X}}{d\mathbf{X} \cdot d\mathbf{X}} \quad (2.13)$$

$$= \frac{1}{2} (\mathbf{F}^T \mathbf{F} - \mathbf{I}) \quad (2.14)$$

$$= \frac{1}{2} (\mathbf{C} - \mathbf{I}) \quad (2.15)$$

where, \mathbf{I} is the identity tensor; and $d\mathbf{X}$ is an infinitesimal material filament in reference coordinate, while $d\mathbf{x}$ is its corresponding deformed filament in the current coordinate; note that $d\mathbf{x} = \mathbf{F} d\mathbf{X}$ in limits. Similarly, the *Almansi-Hamel* strain, which is an Eulerian description of strain measure, is defined as:

$$\mathbf{e} = \frac{1}{2} \frac{d\mathbf{x} \cdot d\mathbf{x} - d\mathbf{X} \cdot d\mathbf{X}}{d\mathbf{x} \cdot d\mathbf{x}} \quad (2.16)$$

$$= \frac{1}{2} (\mathbf{I} - \mathbf{F}^{-T} \mathbf{F}^{-1}) \quad (2.17)$$

$$= \frac{1}{2} (\mathbf{I} - \mathbf{B}^{-1}) \quad (2.18)$$

Left and right Cauchy-Green stretch tensors, \mathbf{B} , and \mathbf{C} only contain stretch information, then the effect of rigid body rotation will not be taken into account in strain – As seen in Equation 2.8, and 2.9 the rotation tensor \mathbf{R} diminishes by multiplying \mathbf{F} and \mathbf{F}^T .

Stress tensor: Based on Cauchy's fundamental lemma, stress is a tensor $\mathbf{T}(\mathbf{x}, t)$ such that the traction \mathbf{t} is a linear homogeneous function of the outer normal \mathbf{n} in the current configuration $\mathcal{X}(\mathbf{X}, t)$:

$$\mathbf{t}(\mathbf{x}, t, \mathbf{n}) = \mathbf{T}(\mathbf{x}, t) \mathbf{n}.$$

It is possible to decompose the stress tensor \mathbf{T} into a volumetric part $-p \mathbf{I}$ and a deviatoric part like \mathbf{s} ; i.e.

$$\mathbf{T} = -p \mathbf{I} + \mathbf{s}$$

where, p is the mean pressure and defined as $p = -\frac{1}{3} \mathbf{T} : \mathbf{I}$. Symbol $:$ denotes the tensorial internal product, i.e. $\mathbf{A} : \mathbf{B} = A_{ij} B_{ij}$.

Stresses are physical quantities and hence there are certain invariants associated with them independent of the coordinate system chosen to represent them. There are three invariants associated with Cauchy's stress:

$$\begin{aligned} I_1 &= \text{tr}(\mathbf{T}) = T_{ii} \\ I_2 &= \frac{1}{2} \mathbf{T} : \mathbf{T} = \frac{1}{2} T_{ij} T_{ij} \\ I_3 &= \det(\mathbf{T}) = \frac{1}{3} T_{ij} T_{jk} T_{ki} \end{aligned}$$

in which, $\text{tr}()$ denotes the trace of a tensor which is the sum of the diagonal elements. Note, $\text{tr}(\mathbf{T}) = \mathbf{T} : \mathbf{I} = -3p$. Similarly, it is possible to define the three invariants of the deviatoric stress as:

$$\begin{aligned} J_1 &= \text{tr}(\mathbf{s}) = 0 \\ J_2 &= \frac{1}{2} \mathbf{s} : \mathbf{s} = \frac{1}{2} s_{ij} s_{ji} \\ J_3 &= \det(\mathbf{s}) = \frac{1}{3} s_{ij} s_{jk} s_{ki} \end{aligned}$$

Stress invariants are widely used in defining *failure or yield surfaces* in material strength models; Specifically, I_1 , J_2 and J_3 . In strength of materials, the von-Mises stress T_e is defined as $T_e = \sqrt{3J_2}$; hence, von-Mises yield criterion is based on only J_2 invariant. Also, pressure hardening failure criteria include I_1 ; note that $I_1 = -3p$.

On a different note, since the first invariant of the stress deviator is zero $J_1 = 0$, then no change in volume occurs due to deviatoric stress and deviators only causes pure shear state.

2.3 Constitutive Equations

A constitutive equation is a relation between forces and motions; or in continuum mechanics terms, it is a function relates *stress* and *motion (or strain)* for a material. For example, stress in *elastic* materials, only depends on deformation gradient \mathbf{F} , or more precisely only on B or C tensors:

$$\mathbf{T} = \mathbf{g}(\mathbf{F})$$

or in *linearly viscous* material, stress is a function of the symmetric part of the velocity gradient D . This class is also referred to as *Navier-Stokes* fluid and takes the form:

$$\mathbf{T} = (-p + \lambda \text{tr}D) \mathbf{I} + 2\mu D \quad (2.19)$$

in which, λ and μ are viscosity parameters; and pressure p is a function of density ρ . In the case of an incompressible Navier-Stokes it will be shown that $\text{tr}D = 0$ - refer to Equation 2.22 - hence, the constitutive equation takes the following form:

$$\mathbf{T} = -p \mathbf{I} + 2\mu D$$

here, p is a Lagrange multiplier to enforce the incompressibility constraint.

In dynamic explicit analysis for highly dynamic phenomena like high speed impacts, it is usual to adopt two constitutive models; the constitutive model that governs the volumetric part of stress is called *equation of state* and it is in the form of $p = f(\rho, e)$. where specifies that pressure depends on density and specific energy. In this study, Ideal-gas equation of state is used for air. Also, for high energetic materials like explosives, Jones-Wilkins-Lee (JWL) equation of state have been adopted. Constitutive model for stress deviator is described via a *strength model*. Strength model is often related to the first stress invariant I_1 and the second deviatoric stress invariant J_2 and sometimes the third deviatoric stress invariant J_3 . In chapter 7, dynamic material models for concrete and steel have been described based on yield surfaces expressed as functions of deviatoric stress invariants.

2.4 Balance Laws

Balance laws in mechanics describe conservation of mass, momentum, and energy and they can be derived via general *transport theorem*. Transport theorem governs the material rate of change of a scalar like $f(\mathbf{x}, t)$ in a time-evolving volume like Ω_t and bounded by surface $\partial\Omega_t$ where \mathbf{n} denotes its unit outward normal vector. The general form of the transport theorem can be presented in following forms:

$$\begin{aligned} \frac{d}{dt} \int_{\Omega_t} f \, dv &= \int_{\Omega_t} \dot{f} + f \operatorname{div} \mathbf{v} \, dv \\ &= \int_{\Omega_t} \frac{\partial f}{\partial t} + \operatorname{div}(f\mathbf{v}) \, dv \\ &= \int_{\Omega_t} \frac{\partial f}{\partial t} \, dv + \int_{\partial\Omega_t} f\mathbf{v} \cdot \mathbf{n} \, da \end{aligned}$$

where, the dot represent material time derivative. $\dot{\square} = \frac{d\square}{dt}$ The transport theorem is employed in deriving mechanics' balance laws; namely, conservation of *mass*, *momentum* and *energy*.

2.4.1 Conservation of Mass

Conservation of mass or continuity equation stipulates that mass can not be created nor destroyed in a time varying material volume.

$$0 = \frac{d}{dt}M = \frac{d}{dt} \int_{\Omega_t} \rho dv$$

substituting $f(\mathbf{x}, t)$ with density ρ in transport theorem, one can get conservation of mass in integral form as following:

$$\int_{\Omega_t} \dot{\rho} + \rho \operatorname{div} \mathbf{v} dv = \int_{\Omega_t} \frac{\partial \rho}{\partial t} + \operatorname{div}(\rho \mathbf{v}) dv = 0$$

since the above integral holds for any arbitrary choice of the volume Ω_t , the integrand must be identically zero at each point. Hence, *conservation of mass* or *continuity equation* is obtained as:

$$\dot{\rho} + \rho \operatorname{div} \mathbf{v} = 0 \quad (2.20)$$

$$\frac{\partial \rho}{\partial t} + \operatorname{div}(\rho \mathbf{v}) = 0 \quad (2.21)$$

In a volume preserving motion or *isochoric motion*, the density ρ is constant or $\dot{\rho} = 0$; then based on Equation 2.20, in such a motion $\operatorname{div} \mathbf{v} = 0$. Also, it can be shown that $\operatorname{div} \mathbf{v} = \operatorname{tr} \mathbf{L} = \operatorname{tr} \mathbf{D}$; Hence, in an isochoric motion following holds:

$$\operatorname{div} \mathbf{v} = \operatorname{tr} \mathbf{L} = \operatorname{tr} \mathbf{D} = 0 \quad (2.22)$$

2.4.2 Conservation of Momentum

The momentum equation relates the rate of change of momentum in a material volume Ω_t to the sum of all forces acting on that volume; forces include body force \mathbf{b} (force

per unit mass) and traction \mathbf{t} .

$$\frac{d}{dt} \int_{\Omega_t} \rho \mathbf{v} dv = \int_{\Omega_t} \rho \mathbf{b} dv + \int_{\partial\Omega_t} \mathbf{t} da \quad (2.23)$$

$$= \int_{\Omega_t} \rho \mathbf{b} + \nabla \cdot \mathbf{T} dv \quad (2.24)$$

In the above, traction \mathbf{t} has been substituted by $\mathbf{t} = \mathbf{T}\mathbf{n}$; in next, using the transport theorem equation in vector form, the left-hand side of equation 2.24 is equivalent to:

$$\frac{d}{dt} \int_{\Omega_t} \rho \mathbf{v} dv = \int_{\Omega_t} \frac{\partial \rho \mathbf{v}}{\partial t} + \nabla \cdot (\rho \mathbf{v} \otimes \mathbf{v}) dv \quad (2.25)$$

in which, $[\mathbf{v} \otimes \mathbf{v}] = v_i v_j$; furthermore, using continuity equation it can be shown the left-hand side of Equation 2.25 is equal to:

$$\frac{d}{dt} \int_{\Omega_t} \rho \mathbf{v} dv = \int_{\Omega_t} \rho \frac{d\mathbf{v}}{dt} dv \quad (2.26)$$

After substituting for left-hand side of Equation 2.24 from Equation 2.26, the integral form of momentum equation is derived as:

$$\int_{\Omega_t} \rho \frac{d\mathbf{v}}{dt} dv = \int_{\Omega_t} (\rho \mathbf{b} + \nabla \cdot \mathbf{T}) dv \quad (2.27)$$

Again, due to arbitrary choice of material volume v_t , two above integrands must be identically equal, which yields the momentum equation in its differential form as:

$$\rho \dot{\mathbf{v}} = \rho \mathbf{b} + \nabla \cdot \mathbf{T} \quad (2.28)$$

$$\frac{\partial \rho \mathbf{v}}{\partial t} + \nabla \cdot (\rho \mathbf{v} \otimes \mathbf{v}) = \rho \mathbf{b} + \nabla \cdot \mathbf{T} \quad (2.29)$$

2.4.3 Conservation of Energy

Conservation of energy in its general form is:

$$\rho \dot{e} + \nabla \cdot \mathbf{q} = \mathbf{T} \cdot \mathbf{L} + \rho r \quad (2.30)$$

where, e is *internal energy*; and \mathbf{q} denotes the *heat flux* and r stands for *radiational heat*. If defining *total energy* as sum of the internal energy and kinetic energy as:

$$E = e + \frac{1}{2} \mathbf{v} \cdot \mathbf{v} \quad (2.31)$$

then the material time derivative of total energy is:

$$\dot{E} = \dot{e} + \dot{\mathbf{v}} \cdot \mathbf{v} \quad (2.32)$$

pre-multiplying both sides of above by ρ and using momentum equation to substitute for $\rho \dot{\mathbf{v}}$ then, it can be shown the following holds:

$$\rho \dot{E} = \rho \dot{e} + \rho \mathbf{b} \cdot \mathbf{v} + \mathbf{v} \cdot \nabla \cdot T \quad (2.33)$$

using the above relation, the energy equation in terms of total energy E can be re-cast as:

$$\rho \dot{E} + \nabla \cdot (\mathbf{q} - T\mathbf{v}) = \rho r + \rho \mathbf{b} \cdot \mathbf{v} \quad (2.34)$$

$$\frac{\partial \rho E}{\partial t} + \nabla \cdot (\rho E \mathbf{v}) + \nabla \cdot (\mathbf{q} - T\mathbf{v}) = \rho r + \rho \mathbf{b} \cdot \mathbf{v} \quad (2.35)$$

2.5 The Euler's Equations

This section is devoted to derivation of Euler equations of gas dynamics which govern compressible flow. Euler equations are categorized as nonlinear hyperbolic equations. Hyperbolic equations may give rise to discontinuities (shocks) in the solution even starting from continuous initial data. This is due to the directional propagation of characteristics with different propagation speeds.

2.5.1 Strong Form of the Euler's Equations

The Euler equations express conservation of mass, momentum and energy in a compressible, inviscid $\mu = \lambda = 0$ and non-conducting fluid $\mathbf{q} = 0$. In inviscid fluid, the

Cauchy stress \mathbf{T} only contains the pressure term $-p\mathbf{I}$ - refer to Equation 2.19. In the absence of the body force \mathbf{b} , Euler equations read as following:

$$\frac{\partial \rho}{\partial t} + \nabla \cdot (\rho \mathbf{v}) = 0 \quad (2.36)$$

$$\frac{\partial \rho \mathbf{v}}{\partial t} + \nabla \cdot (\rho \mathbf{v} \otimes \mathbf{v} + p\mathbf{I}) = 0 \quad (2.37)$$

$$\frac{\partial \rho E}{\partial t} + \nabla \cdot ((\rho E + p)\mathbf{v}) = 0 \quad (2.38)$$

Euler equations can be recast in vector form as:

$$\mathbf{u}_t + \frac{\partial \mathbf{f}_1}{\partial x_1} + \frac{\partial \mathbf{f}_2}{\partial x_2} + \frac{\partial \mathbf{f}_3}{\partial x_3} = 0 \quad (2.39)$$

where \mathbf{u} is the vector of the conservation variables, and \mathbf{f}_i is the associated flux vector in i -th spatial dimension:

$$\mathbf{u} = \begin{pmatrix} \rho \\ \rho \mathbf{v} \\ \rho E \end{pmatrix} \quad (2.40)$$

$$\mathbf{f}_i = \begin{pmatrix} \rho v_i \\ \rho \mathbf{v} v_i + p \\ (\rho E + p)v_i \end{pmatrix} \quad i = 1, 2, 3 \quad (2.41)$$

The vector form of Euler equations in 2.39 can be further compacted using the divergence of the flux vector

$$\nabla \cdot \mathbf{f} = \frac{\partial \mathbf{f}_1}{\partial x_1} + \frac{\partial \mathbf{f}_2}{\partial x_2} + \frac{\partial \mathbf{f}_3}{\partial x_3} \quad (2.42)$$

$$\mathbf{f} = \begin{pmatrix} \mathbf{f}_1 \\ \mathbf{f}_2 \\ \mathbf{f}_3 \end{pmatrix}; \quad (2.43)$$

Then, the Euler equations along with appropriate boundary conditions and initial condition reduce to:

$$\mathbf{u}_t + \nabla \cdot \mathbf{f} = 0 \quad (2.44)$$

$$\mathbf{f}^{in} \cdot \mathbf{n} = \mathbf{g} \quad (2.45)$$

$$\mathbf{u}(\mathbf{x}, 0) = \mathbf{u}_0(x) \quad (2.46)$$

where, \mathbf{f}^{in} denotes the boundary condition only for the inflow portion of the boundary. In hyperbolic equations only inflow components of the flux vector can be prescribed. In order to close above equations, also we need to define the equation of state. The equation of state relates pressure p to internal energy e and density ρ , i.e. $p = f(e, \rho)$. In an ideal gas, internal energy is only a function of temperature; specifically, for a polytropic gas, the internal energy is proportional to temperature: $e = c_v T$, where c_v is constant and known as the specific heat at constant volume.

$$p = R\rho T = \frac{R}{c_v} \rho e \quad (2.47)$$

where R is the gas constant per unit mass, which is equal to the universal gas constant \mathcal{R} divided by the molecular mass of the fluid.

2.5.2 Euler's Equations in One-dimension

In one-dimensional geometry, Euler's equations reduce to:

$$\frac{\partial \rho}{\partial t} + \frac{\partial \rho v}{\partial x} = 0 \quad (2.48)$$

$$\frac{\partial \rho v}{\partial t} + \frac{\partial (\rho v^2 + p)}{\partial x} = 0 \quad (2.49)$$

$$\frac{\partial \rho E}{\partial t} + \frac{\partial (\rho E + p)v}{\partial x} = 0 \quad (2.50)$$

also, in conservative form, they can be shown as:

$$\frac{\partial \mathbf{u}}{\partial t} + \frac{\partial \mathbf{f}}{\partial x} = 0 \quad \text{where } x \in [0, L] \quad (2.51)$$

in which, conservative variables \mathbf{u} and flux vector \mathbf{f} are:

$$\mathbf{u} = \begin{pmatrix} \rho \\ \rho v \\ \rho E \end{pmatrix}, \quad (2.52)$$

$$\mathbf{f} = \begin{pmatrix} \rho v \\ \rho v^2 + p \\ (\rho E + p)v \end{pmatrix}, \quad (2.53)$$

2.5.3 Characteristic Form of the Euler Equations

In one-dimensional Euler Equations, it is possible to define the *Jacobian* \mathbf{A} of the flux \mathbf{f} as following:

$$\mathbf{A}(\mathbf{u}) = \frac{\partial \mathbf{f}}{\partial \mathbf{u}}$$

using the chain rule, it is possible to show that:

$$\frac{\partial \mathbf{f}}{\partial x} = \frac{\partial \mathbf{f}}{\partial \mathbf{u}} \frac{\partial \mathbf{u}}{\partial x} = \mathbf{A} \frac{\partial \mathbf{u}}{\partial x}$$

using above, the Euler Equations in quasi-linear form is:

$$\frac{\partial \mathbf{u}}{\partial t} + \mathbf{A} \frac{\partial \mathbf{u}}{\partial x} = 0$$

It can be shown that the above form of Euler Equations in conservative form can be transformed to equivalent Equations through *diagonalization* of Jacobian \mathbf{A} ; this form of Euler Equations is called *characteristic form*:

$$\frac{\partial \mathbf{w}}{\partial t} + \Lambda \frac{\partial \mathbf{w}}{\partial x} = 0 \quad (2.54)$$

in which the characteristic variables \mathbf{w} and Λ are:

$$\mathbf{w} = \begin{pmatrix} s \\ v + \frac{2a}{\gamma-1} \\ v - \frac{2a}{\gamma-1} \end{pmatrix}, \quad (2.55)$$

$$\Lambda = \begin{bmatrix} v & 0 & 0 \\ 0 & v+a & 0 \\ 0 & 0 & v-a \end{bmatrix} \quad (2.56)$$

in above s denotes the entropy and a represents the wave speed. The characteristic form is very appealing since it decouples the basic variables; The physical interpretation of characteristic form is Euler equations give rise to the propagation of three signals in characteristic directions. These three signals travel with velocities of v , $v + a$, and $v - a$. Values of characteristic variables \mathbf{w} along their corresponding characteristics are constant. The three characteristics are $dx = vdt$ and $dx = (v \pm a)dt$.

2.6 Thermodynamical Aspects of Euler Equation

While balance laws ensures equilibrium of mass, momentum, and energy in *macroscopic* level, *equations-of-state* (EOS) satisfies the equilibrium of thermodynamical properties in *molecular* level. For example in an ideal gas law, the thermal equation-of-state:

$$p = \rho RT \quad (2.57)$$

satisfies the conservation of momentum providing that large numbers of molecules interact only upon direct collision; and *caloric equation-of-state* satisfies the conservation of energy on the microscopic level:

$$e = c_v T \quad (2.58)$$

where c_v is the *constant volume specific heat*. An equivalent expression is as following:

$$h = c_p T \quad (2.59)$$

where h is enthalpy being defined as $h = e + p/\rho$ and c_p is the *constant pressure specific heat*. A fluid that satisfies both thermal and caloric equations-of-state is called a *perfect gas*. In this work, air has been assumed to behave like a perfect gas. In following a number of useful definitions or identities for perfect gas have been mentioned:

- The *ratio of specific heats* is defined as $\gamma = c_p/c_v$. For sea-level air, $c_p = 1004 \text{ N.m/kg.K}$ and $c_v = 717 \text{ N.m/kg.K}$; then $\gamma = 1.4$ at sea-level.
- The gas constant and specific heats are related by $c_p = R + c_v$ or $c_v = R/(\gamma - 1)$.
- The thermal equation-of-state can be recast in other useful forms $p = \rho RT = (\gamma - 1)\rho e = (\gamma - 1)(\rho E - \frac{1}{2}\rho v^2)$.
- The *speed of sound* is the speed at which small disturbances propagate through a medium measured relative to the movement of the medium. For a perfect gas, it can be shown that $a^2 = \gamma RT = \frac{\gamma p}{\rho}$. In a linear elastic solid, the speed of sound is $a^2 = E/\rho$ where E is the Elastic Modulus.
- The *shock front velocity* U_s that overpressure p_s propagates relative to the medium is $U_s = a_0 \sqrt{1 + \frac{\gamma+1}{2\gamma}(\frac{p_s}{p_0} - 1)}$ where $a_0 = \sqrt{\frac{\gamma p_0}{\rho_0}}$. Subscript $_0$ denotes ambient air properties.
- *Mach number* $M = u/a$ is defined as the ratio of particle velocity to the speed of sound. When $M > 1$, the flow known as supersonic. In supersonic flows, particles travel with velocities faster than the speed of sound.

CHAPTER 3

EXPLICIT AND IMPLICIT FINITE ELEMENT

In the previous chapter, the Euler's equations were discussed. In this chapter, the technology to solve the Euler's equations with finite element methods will be presented. In doing so, the concepts of spatial and temporal discretization of the linearized weak form of the equations will be elaborated. The model equation that will be used in describing different methods is Burger's equation which is a scalar equation that is very similar to Euler's equations.

3.1 Burger's Equation

One of the basic nonlinear partial differential equations (PDE) that provides a reach introduction to nonlinearity is Burgers equation. In fact Euler's equations are a set of three Burger's-like equations. Similar to Euler's equations, Burger's equation can can develop nonlinear phenomena such as shocks, wave-breaking, as well as multi-valuedness even from smooth initial values.

In one dimensional setting, $x \in \Omega$ and $\Omega \subset R$, Burger's equation reads:

$$\phi_t + \phi\phi_x = 0 \quad \text{in } \Omega \times]0, T] \quad (3.1)$$

$$\phi(x, 0) = \phi_0 \quad (3.2)$$

$$\phi(0, t) = \phi_D \quad \text{on } \Gamma_D^{in} \times]0, T] \quad (3.3)$$

It should be mentioned the Dirichlet boundary condition should be prescribed only on inflow part of boundary (Γ_D^{in}).

From conservation point of view, Burgers equation governs the conservation of a flux in the form of $f(\phi) = \frac{1}{2}\phi^2$. Applying flux conservation in the vicinity

of shock/discontinuity results in Rankine-Hugoniot jump condition. From Rankine-Hugoniot condition, the velocity for shock propagations in Burger's Equation is:

$$U = \frac{f(\phi_R) - f(\phi_L)}{\phi_R - \phi_L} = \frac{\phi_R + \phi_L}{2} \quad (3.4)$$

where R , and L subscripts denote right and left side of the discontinuity.

3.1.1 Linearizing Weak Form and Newton-Raphson Method

In this section, weak (variational) form of the Burgers equation is established. Then, it is tried to solve the weak form via using Newton-Raphson method. The weak form is obtained through multiplying the governing equation by a weighting (test) function like w and then integrating over the computational domain. For example weak form for Burger's equation is:

$$\delta W(w, \phi) = \int_0^L w (\phi_t + \phi \phi_x) dx = 0$$

We wish to solve the weak form for ϕ for any admissible test function w . The weak form is a nonlinear equation and a widely used method to solve nonlinear equations is Newton-Raphson (N-R) method. Newton-Raphson method require to linearize the weak form. The linearization can be done via Taylor expansion.

$$\delta W(w, \phi^{k+1}) \approx \delta W(w, \phi^k) + \nabla_{\phi} \delta W(w, \phi^k) \cdot \Delta \phi = 0$$

where k is the iteration number. After having linearized form, steps in Table 3.1 should be done to get an acceptable approximation like ϕ^* .

The Newton-Raphson method in above is presented in a quite general context. For the Burgers problem at hand, linearization of the weak form is:

$$\delta W(w, \phi^{k+1}) \cong \delta W(w, \phi^k) + \int_0^L w (\Delta \phi_t + \Delta \phi \phi_x + \phi \Delta \phi_x) dx = 0 \quad (3.5)$$

Table 3.1 Newton-Raphson Iteration

-
-
1. set iteration counter $k \leftarrow 0$,
 2. initialize ϕ^0 ,
 3. linearize $\delta W(w, \phi^{k+1}) = 0$ about ϕ^k ,
 4. solve for increment $\Delta\phi$ from step 3,
 5. update ϕ^{k+1} with $\phi^k + \Delta\phi$,
 6. check convergence criterion $\|\phi^{k+1} - \phi^k\| \leq tol.$,
 7. if converged, $\phi^* = \phi^{k+1}$ and stop; otherwise, $k \leftarrow k + 1$ and go to step 3.
-

3.1.2 Spatial Finite Element Discretization

Here, Galerkin finite element spatial discretization is performed for the linearized weak form of the Burger's equation. Adopting appropriate shape function N_A for node such as A , then trial solution ϕ can be approximated with the piece-wise finite element approximation ϕ^h as following:

$$\phi(x) \approx \phi^h(x) = \sum_{A \in \eta/\eta_D} N_A(x)\phi_A + \sum_{A \in \eta_D} N_A(x)\phi_D \quad (3.6)$$

where, ϕ_A denotes the unknown nodal value at node A and ϕ_D are known nodal values at Dirichlet boundaries. Also, choosing the test function as:

$$w^h(x) = \sum_{A \in \eta/\eta_D} N_A(x)w_A \quad (3.7)$$

In above, it is implied that domain Ω is discretized with non-overlapping elements like Ω^e , where $1 \leq e \leq n_{el}$. Furthermore, substituting the finite element approximations – Equations 3.6, and 3.7 – in the weak form – Equation 3.5 – yields following semi-discretized equation:

$$\mathbf{M} \frac{d}{dt} \Delta\Phi + \mathbf{C} \Delta\Phi = \mathbf{P} \quad (3.8)$$

in which, Φ lists all unknown nodal values like ϕ_A ; \mathbf{M} is the generalized mass matrix; \mathbf{C} is the convective matrix, and \mathbf{P} is the generalized force vector. All previous matrices are formed through element assembly:

$$\mathbf{M} = \sum \mathbf{M}^e \quad \mathbf{C} = \sum \mathbf{C}^e \quad \mathbf{P} = \sum \mathbf{P}^e$$

where superscript e denotes element-wise contribution of matrices and Σ represents assembly procedure. Element matrices are calculated as following:

$$\mathbf{M}^e = \int_{\Omega^e} \mathbf{N}^T \mathbf{N} \, dx \quad (3.9)$$

$$\mathbf{C}^e = \int_{\Omega^e} (\mathbf{N}^T \mathbf{B} \Phi \mathbf{N} + \mathbf{N}^T \mathbf{N} \Phi \mathbf{B}) \, dx \quad (3.10)$$

$$\mathbf{P}^e = \int_{\Omega^e} (\mathbf{N}^T \mathbf{N} \Phi_t + \mathbf{N}^T \mathbf{N} \Phi \mathbf{B} \Phi) \, dx + \text{natural boundary terms} \quad (3.11)$$

where, matrix \mathbf{N} contains all nodal shape functions for all of the nodes in element e . Matrix \mathbf{B} contains the spatial derivatives of \mathbf{N} . All above integrations can be evaluated via numerical methods like Gauss quadrature. In Gauss quadrature method, the integrand is evaluated at Gauss points and the integral is approximated by appropriate weighting of the integrand at Gauss points. For example for n_{gp} Gauss points, the integration is done as:

$$\int_{-1}^{+1} I(x) \, dx \approx \sum_{i=1}^{n_{gp}} \omega_i I(x_i)$$

in which, ω_i is the weighting coefficient for the gauss point like i .

3.2 Temporal Discretization

So far, the spatial discretization of the weak form has been performed as shown in Equation 3.8. To fully solve semi-discretized equation, we should also perform temporal discretization. In order to get accurate results, the accuracy order of

Table 3.2 The θ Family of Time Integration Methods

θ	Method	Stability	Order of Accuracy
$\theta = 0$	Euler	conditionally stable	first order
$\theta = 1/2$	Crank-Nicolson	unconditionally stable	second order
$\theta = 3/2$	Galerkin	unconditionally stable	first order
$\theta = 1$	Backward Euler	unconditionally stable	first order

temporal discretization needs to be at least of that of spatial discretization. The schemes for solving first order differential equations in Equation 3.8 include *the θ family of methods*, and *the Lax-Wendroff method*. Also, for second-order differential equations, *Newmark* scheme is one of the most popular time integration methods.

The θ family of methods: This family of methods is highly used in integrating the first-order differential equations. The value of the time derivative is approximated by a weighted average of ϕ_t^n and ϕ_t^{n+1} :

$$\frac{\phi(t^{n+1}) - \phi(t^n)}{\Delta t} = \theta \phi_t^{n+1} + (1 - \theta) \phi_t^n + \text{H.O.T} \quad (3.12)$$

The parameter θ is in the interval $[0, 1]$. For some specific values of θ , some well-known methods will be recovered as summarized in Table 3.2. For $\theta = 0$, the well-known Euler's scheme will be recovered. Euler's scheme is conditionally stable. The stability condition is known as Courant-Friedrichs-Lewy or CFL condition. The CFL condition for Euler's method is $\frac{a\Delta t}{\Delta x} \leq 1$, in which a is the speed of sound. Based on the CFL condition, time step Δt should be small enough that the wave signal travel at most one element Δx . CFL condition should be respected for all explicit time integration schemes.

Other schemes in Table 3.2 such as Crank-Nicolson, Galerkin, and Backward Euler, are unconditionally stable regardless of the size of time step Δt . These methods are implicit.

Lax-Wendroff Method: This method is based on a truncated Taylor series expansion. It is second order accurate like Crank-Nicolson; however, it is explicit.

$$\frac{\phi(t^{n+1}) - \phi(t^n)}{\Delta t} = \phi_t^n + \frac{1}{2} \Delta t \phi_{tt}^n + \text{H.O.T} \quad (3.13)$$

the first and second derivative ϕ_t, ϕ_{tt} are substituted from the differential equation.

Newmark Methods: One of the widely used time integration methods for first and second order ordinary differential equations is the Newmark methods. Providing values of a scalar at instance t , i.e., $\phi(t)$ as well as its first and second time derivatives, i.e. $\phi_t(t)$, and $\phi_{tt}(t)$ are known, then it is possible to estimate values of $\phi(t + \Delta t)$ and $\phi_t(t + \Delta t)$ according to following Taylor-like approximations:

$$\phi(t + \Delta t) \approx \phi(t) + \Delta t \phi_t(t) + \Delta t^2 [(0.5 - \alpha)\phi_{tt}(t) + \alpha \phi_{tt}(t + \Delta t)]$$

$$\phi_t(t + \Delta t) \approx \phi_t(t) + \Delta t [(1 - \beta)\phi_{tt}(t) + \beta\phi_{tt}(t + \Delta t)]$$

If one introduces an increment in $\phi_{tt}(t + \Delta t)$ in the above equation, following equalities can be obtained:

$$\Delta\phi(t + \Delta t) \approx \alpha \Delta t^2 \Delta\phi_{tt}(t + \Delta t) \quad (3.14)$$

$$\Delta\phi_t(t + \Delta t) \approx \beta \Delta t \Delta\phi_{tt}(t + \Delta t) \quad (3.15)$$

It is easy to observe following equation when dividing each side of above equations respectively:

$$\Delta\phi_t(t + \Delta t) \approx \frac{\beta}{\alpha \Delta t} \Delta\phi(t + \Delta t) \quad (3.16)$$

At this point, we proceed to temporally discretize Equation 3.8. Substituting for ϕ_t from Equation 3.16, following linear system of equations is obtained:

$$\left(\frac{\beta}{\alpha \Delta t} \mathbf{M} + \mathbf{C} \right) \Delta \Phi = \mathbf{P} \quad (3.17)$$

Above linear system may be solved with direct or iterative methods depending on the size of the unknowns. It is noted that the resulting coefficient matrix is not symmetric since \mathbf{C} is not symmetric.

Following Table summarizes procedures should be carried out in solving Burgers equation. If the time domain is sampled at n equal time span Δt , then we denote time at the end of the step i as $t_i = i \Delta t$ which $i = 1, \dots, n$:

Table 3.3 Newmark Method

1. initialize $\Phi(t = 0)$,
2. set time step counter $i \leftarrow 1$,
3. call Newton-Raphson routine to solve $(\beta/(\alpha \Delta t) \mathbf{M} + \mathbf{C}) \Delta \Phi = \mathbf{P}$
4. get $\Delta \Phi^*$ from Newton-Raphson routine
5. assign $\Phi(t_i) = \Phi(t_{i-1}) + \Delta \Phi^*$
6. if $i < n$ then $i \leftarrow i + 1$ and go to step 3; otherwise stop.

3.3 The Euler's Equations

As discussed, Eulers's equations are a collection of mass, linear momentum, and energy conservation for an inviscid and compressible fluid with no heat-conduction involved. As shown in Chapter 2, in one-dimensional geometry, Euler's equations reduce to:

$$\frac{\partial \mathbf{u}(x, t)}{\partial t} + \frac{\partial \mathbf{f}(x, t)}{\partial x} = 0 \quad \text{where } x \in [0, L] \quad (3.18)$$

In which,

$$\mathbf{u} = \begin{pmatrix} u_1 \\ u_2 \\ u_3 \end{pmatrix} = \begin{pmatrix} \rho \\ \rho v \\ \rho E \end{pmatrix}, \quad \mathbf{f} = \begin{pmatrix} f_1 \\ f_2 \\ f_3 \end{pmatrix} = \begin{pmatrix} \rho v \\ \rho v^2 + p \\ (\rho E + p)v \end{pmatrix},$$

Defining the Jacobian of the Flux vector \mathbf{f} as $\mathbf{A}(\mathbf{u}) = \frac{\partial \mathbf{f}}{\partial \mathbf{u}}$, the Euler equations can be written in the quasi-linear form:

$$\frac{\partial \mathbf{u}(x, t)}{\partial t} + \mathbf{A}(\mathbf{u}) \frac{\partial \mathbf{u}(x, t)}{\partial x} = 0$$

Substituting for conservative variables \mathbf{u} in the above equation will give rise to the following expanded form of the Euler's equations:

$$\begin{aligned} \frac{\partial u_1}{\partial t} + \frac{\partial u_2}{\partial x} &= 0 \\ \frac{\partial u_2}{\partial t} + \frac{\gamma - 3}{2} \left(\frac{u_2}{u_1}\right)^2 \frac{\partial u_1}{\partial x} + (3 - \gamma) \left(\frac{u_2}{u_1}\right) \frac{\partial u_2}{\partial x} + (\gamma - 1) \frac{\partial u_3}{\partial x} &= 0 \\ \frac{\partial u_3}{\partial t} + (\gamma - 1) \left(\frac{u_2}{u_1}\right)^3 - \gamma \frac{u_2 u_3}{u_1^2} \frac{\partial u_1}{\partial x} + \left(\gamma \left(\frac{u_3}{u_1}\right) - \frac{3}{2} (\gamma - 1) \left(\frac{u_2}{u_1}\right)^2\right) \frac{\partial u_2}{\partial x} + \gamma \frac{u_2}{u_1} \frac{\partial u_3}{\partial x} &= 0 \end{aligned}$$

In order to solve Euler's equation with finite element methods, weak form should be obtained for above equations. Next, spatial and temporal discretization should be performed for the linearized weak form. The procedure is very similar to the one explained for Burgers equation. Also, numerical stabilization techniques such as artificial viscosity should be employed in order to remove un-physical oscillations that occur in the vicinity of shocks. One of the techniques to damp the un-physical oscillations is Flux Corrected Transport (FCT) method which is being used in Autodyn. This method was introduced by Book and Boris [14].

This chapter concludes the theoretical discussion on the procedures to solve Euler's equations. From the next chapter, the results of solving Euler's equation for

different problems of blast wave loading with Autodyn are presented.

CHAPTER 4

ASSESSING AUTODYN RESULTS ACCURACY AND LIMITATIONS

In this chapter, spherical blast *detonation* and its *propagation* in free air is discussed. Detonation and propagation of shock waves are simulated with Autodyn and results are compared with ConWep program as the benchmark. ConWep is calibrated based on extensive number of tests and used frequently in engineering practice. Capabilities and limitations of Autodyn in capturing accurate results will be discussed.

4.1 Spherical Blast Simulation with Autodyn

Here, the detonation of a spherical charge and its propagation in open air is modeled in Autodyn. In doing so, a wedge shaped geometry is filled with air and the explosive charge is positioned at the vertex with a proper radius. It is possible to take advantage of axi-symmetric nature of the geometry and only model a slice as shown in Figure 4.1. The two dimensional wedge (slice) will be discretized with only one cell in circumferential direction and very fine size cell in radial direction. The detonation starts at the vertex and energy gets released and propagates in the air in form of shock waves.

In terms of materials, air is considered as ideal gas and explosive charges are modeled with Jones-Wilkins-Lee (JWL) equation of state. The JWL equation of state is used to calculate the pressure of the detonation products of explosives. A typical pressure-specific volume $p - v$ curve for JWL equation of state is shown in Figure 4.2. When the charge detonates the specific volume v increases and pressure drops in the expanded detonated materials. The JWL equation of state is expressed as following:

$$p(\rho, e) = A \left(1 - \frac{\omega\rho}{R_1\rho_0}\right) \exp\left(\frac{-\rho R_1}{\rho_0}\right) + B \left(1 - \frac{\omega\rho}{R_2\rho_0}\right) \exp\left(\frac{-\rho R_2}{\rho_0}\right) + \omega\rho e \quad (4.1)$$

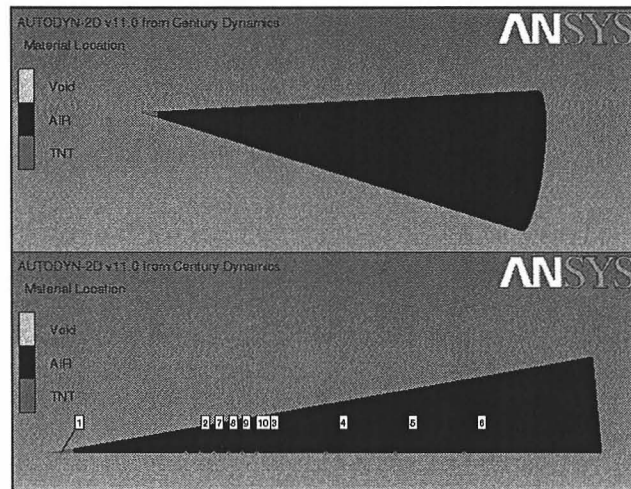


Figure 4.1 Free Air Blast Model

In above, JWL contains five parameters A , B , R_1 , R_2 , ω which have to be determined

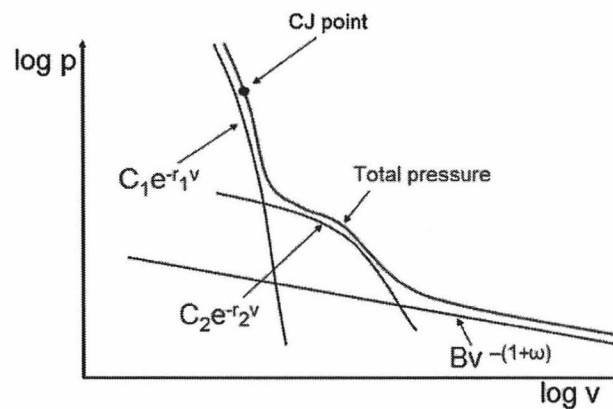


Figure 4.2 Pressure versus Specific Volume in JWL

for different materials experimentally. For example, these parameters for TNT are reported in Table 4.1.

4.2 ConWep Program

ConWep is a software developed to calculate the blast parameters in different blast environments; i.e. internal or external explosions. ConWep does not solve for gov-

Table 4.1 JWL Parameters for TNT

Density, ρ_0	1630 [kg/m ³]
Parameter, A	3.74e8 [kPa]
Parameter, B	3.75e6 [kPa]
Parameter, R_1	4.15
Parameter, R_2	0.90
Parameter, ω	0.35
C-J Detonation Velocity,	6.93e3 [m/s]
C-J Energy / unit volume,	6.00e6 [kJ/m ³]
C-J Pressure,	2.10e7 [kPa]

erning physics equation; however, it is based on a compilation of results of extensive number of blast tests. ConWep contains polynomial equations for blast parameters which are derived from curve-fitting of scaled explosive test using charge weights from less than 1 kg to over 400,000 kg.

The pressure-time history curve in ConWep has been taken as a combined linear and exponential decay form as following:

$$p(t) = p_s \left(1 - \frac{t - T_a}{T_s}\right) \exp\left(\frac{t - T_a}{-\alpha}\right) \quad 0 \leq t \leq T_a + T_s \quad (4.2)$$

The blast parameters in above, namely peak pressure p_s , time-of-arrival T_a , duration T_s and the decay parameter α are determined from experimental equations or graphs available in manual TM-855-1 [?]. All four parameters (or scaled form of them) are functions of scaled distance z . For example peak overpressure p_s , and scaled impulse $i/w^{\frac{1}{3}}$ versus scaled distance z are shown in Figure 4.3 and Figure 4.4, respectively. Also, scaled arrival time $T_a/w^{\frac{1}{3}}$ and scaled duration $T_s/w^{\frac{1}{3}}$ are depicted in Figure 4.5.

All the mentioned graphs are prepared from ConWep results.

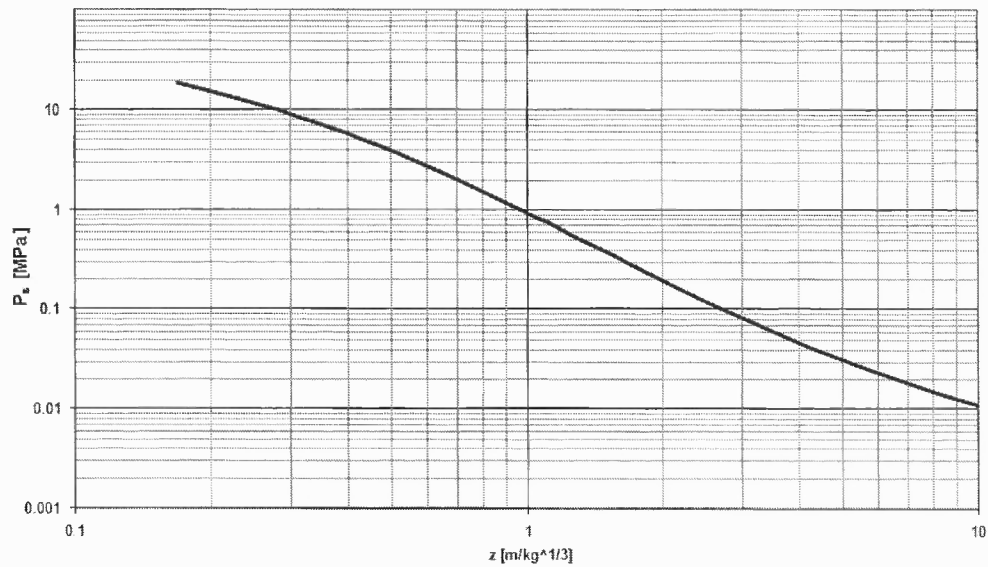


Figure 4.3 Peak Pressure as a Function of Scaled Distance

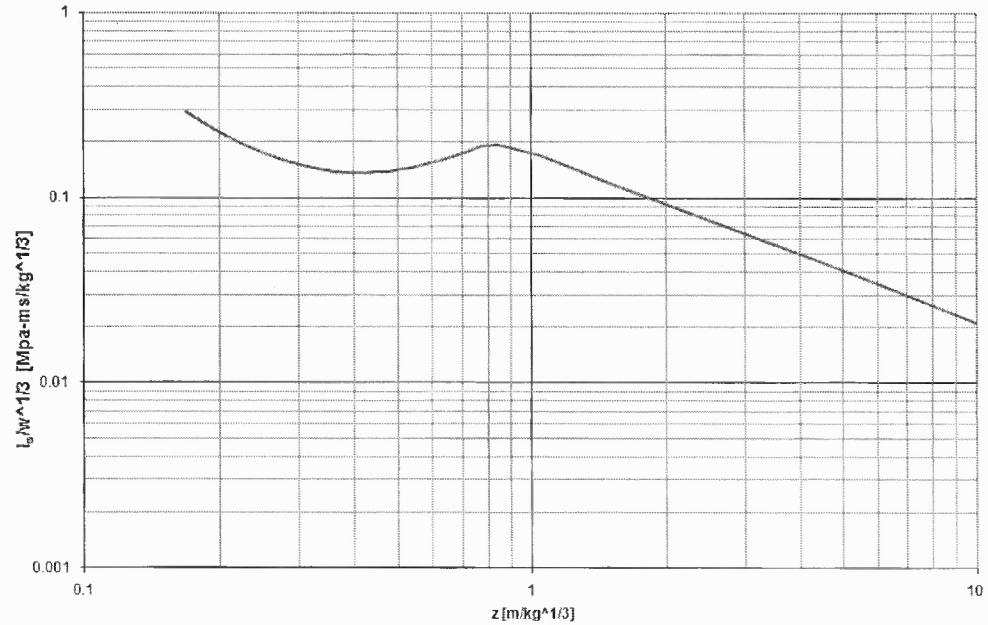


Figure 4.4 Scaled Impulse as a Function of Scaled Distance

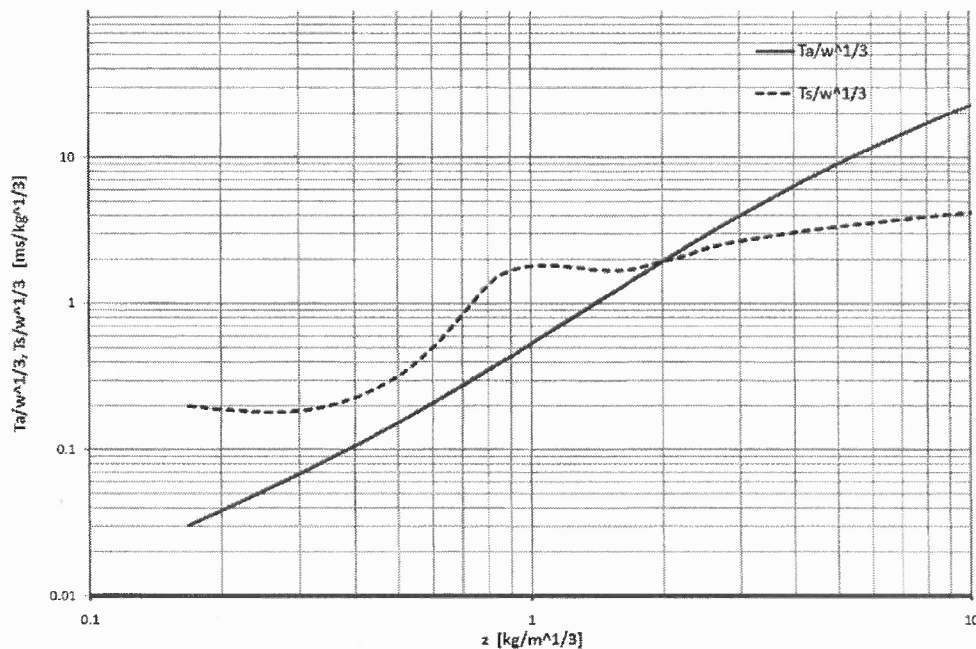


Figure 4.5 Scaled Arrival Time and Scaled Duration versus Scaled Distance

As it is seen in Figure 4.3, peak pressure decreases uniformly as scaled distance increases. However, the impulse trend in Figure 4.4 is not uniformly decreasing and there is a local maximum around $z = 0.8$. Scaled arrival time keeps longer for larger scaled distances; also, scaled duration increases as scaled distance increases.

To explain these facts, it should be noted in large scaled distances - i.e. less intense shock waves - the shock front velocity is smaller comparing with small scaled distances. In fact shock front velocity U_s as shown in chapter 2 reads:

$$U_s = a_0 \sqrt{1 + \frac{\gamma + 1}{2\gamma} \left(\frac{p_s}{p_0} - 1\right)} \quad (4.3)$$

It takes longer for less intense shocks, i.e. smaller p_s , to travel a certain distance as well as it takes longer for them to get cleared at a point. This translates to larger arrival time and longer durations.

Impulse as the area under pressure history depends not only on peak pressure

but also on duration time T_s . As scaled distance z increases the peak pressure decreases; on the other hand, duration time increases as scaled distance z increases. This means the pressure disturbance lingers longer despite the decrease of peak pressure. The opposite effects of variation of pressure and duration time result in the impulse trend shown in Figure 4.4.

4.3 Comparing Autodyn and ConWep

As mentioned, blast parameters for characterizing pressure history profile include peak overpressure p_s , positive-phase duration T_s , time-of-arrival T_a , and positive impulse i_s . For verification purpose of Autodyn, the above parameters are calculated with Autodyn and they are compared with ConWep program.

In designing simulations, three different TNT charge weights w are selected; namely, 0.454 kg, 4.54 kg, 45.4 kg. Blast parameters are measured at 0.5, 1.0, 1.5, 2.0, 2.5 meter standoff distances R . Based on standoff distances R and charge weights w , a range of scaled distances between $z = 0.140 \text{ m/kg}^{\frac{1}{3}}$ and $z = 3.255 \text{ m/kg}^{\frac{1}{3}}$ are considered. Each model is discretized with three different grid sizes; namely 5, 10, 20 mm. Totally 9 simulations (3 different charge weights \times 3 different mesh sizes) are performed and in each simulation, parameters are obtained for 5 stand-off distances (or equivalently scaled distances).

It is noteworthy to mention the above range for scaled distance z is quite in practical range. It has been documented in [17] that for blasts in scaled distance ranges smaller than $z = 0.2 \text{ m/kg}^{\frac{1}{3}}$ the shock is such intense that it can cause the total brisance of concrete columns. In scaled distances larger than $z = 4.0 \text{ m/kg}^{\frac{1}{3}}$, the overpressure is less than 0.05 MPa (around 7 psi) and insignificant. In following sections, blast parameters are compared for Autodyn and ConWep.

Peak Overpressure: The overpressures obtained from Autodyn are overlaid on the graph obtained from ConWep as shown in Figure 4.6. Comparison between Autodyn and ConWep overpressures shows that Autodyn is able to predict overpressures with less than 20% error even for the coarsest mesh. Autodyn predictions generally underestimate those of ConWep. To explain this, in general, numerical methods smear the shock over at least one element. The smaller the element is, the better the peak pressure is resolved. The true peak overpressure can be resolved at the limits when element sizes and time-steps tend to infinitesimal values.

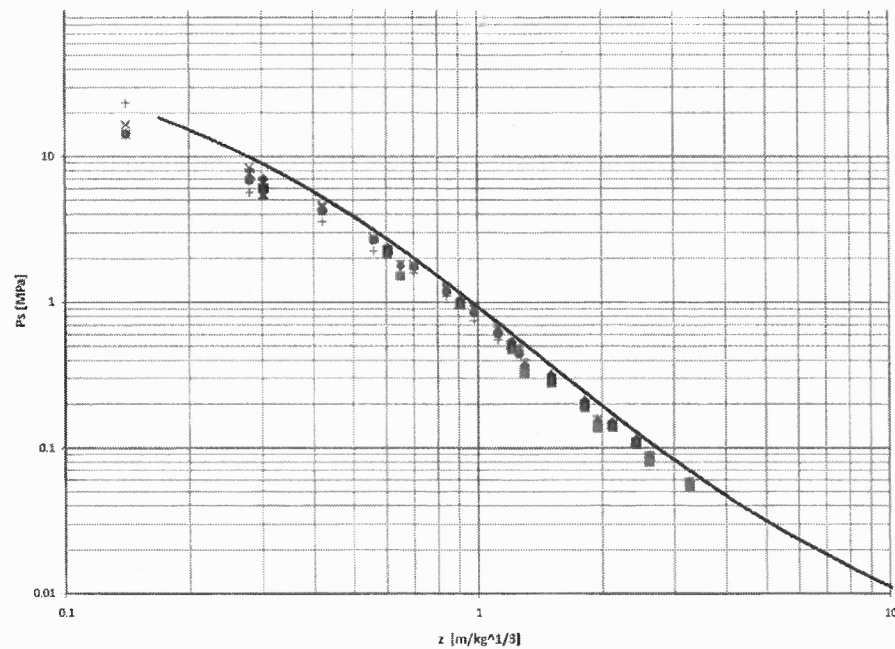


Figure 4.6 Overpressure versus scaled distance.

Time of Arrival: Time-of-arrival T_a represents elapsed time for shock wave to travel the stand-off distance. Scaled arrival times $T_a/w^{1/3}$ are shown in Figure 4.7 for results obtained from Autodyn. Autodyn is successful in predicting correct arrival times.

The success of Autodyn in predicting correct times of arrival is a proof that Autodyn Multi-Material Euler solver is able to capture shock front velocity correctly. As shown in Equation 4.3, shock front velocity U_s depends on the sound-speed a_0 as well as on the intensity of the shock p_s .

In order for a numerical scheme to correctly capture shock wave velocities, it should be numerically conservative in terms of fluxes; i.e. mass, momentum and energy fluxes. Non conservative numerical methods consistently under- or overestimates the shock velocities. [15]

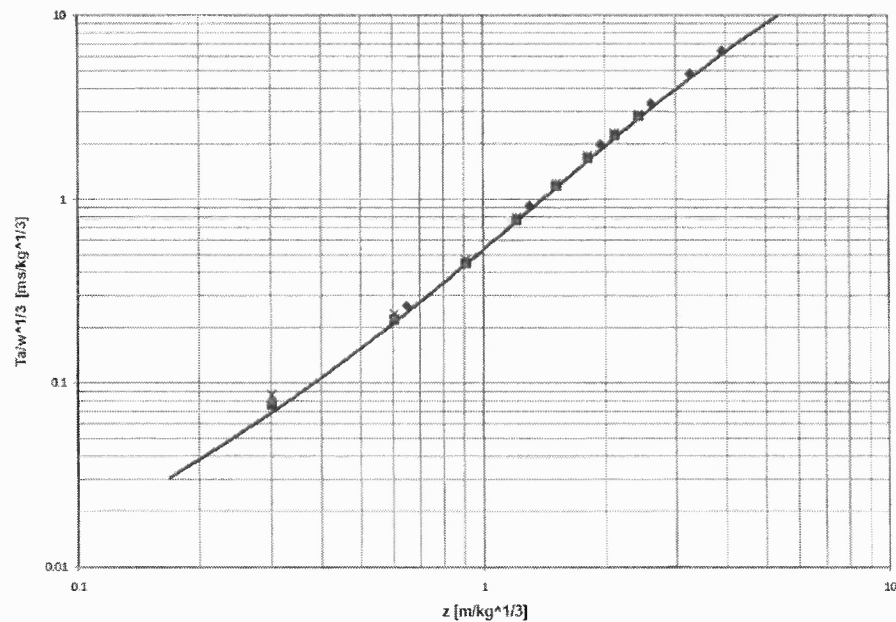


Figure 4.7 Scaled Arrival Time versus Scaled Distance.

Positive Impulse: Scaled positive impulses $i/w^{1/3}$ versus scaled distance z are shown in Figure 4.8. As observed, Autodyn impulses is less conforming with ConWep results comparing with previous blast parameters.

As mentioned, ConWep adopts an idealized profile for pressure time history

as shown in Equation 4.2. This curve is the product of a linear decay as well as exponential decay functions. Specifically, the exponential decay contains a decay parameter α which is provided by the ConWep. The impulse in ConWep has been determined through integrating the idealized profile.

In reality, wave reflections at the interface of explosive materials and air occur due to different impedance properties of air and explosive materials. As a results, a portion of the overpressure propagates into the air at the interface and some reflects back into the explosive materials. Pressure travels back into the explosives till gets reflected from the center of the wedge. It is understood that the reflections at the interfaces modify the idealized pressure history and hence affecting the impulse which is the area under pressure history profile.

A sample pressure history at standoff distance 2.00 m and charge weight 45.4 kg is shown in Figure 4.9. As seen, Autodyn profile clearly bulges out at two instants as compared with Idealized profile of ConWep. These pressure bulges are due to pressure reflections at the interface.

4.4 Conclusion

Blast parameters obtained from Autodyn one-dimensional simulations are discussed and compared with ConWep results. For peak overpressures and arrival times, a fairly good agreement between results are observed. For impulse, it is believed that the idealized pressure history profile adopted in ConWep might be over simplifying and neglecting some aspects of the physics of the problem including pressure reflections at the interface between the explosive materials and air.

Clearly, more experimental research is needed to assess the pressure history profile. On the other hand, due to the inherent uncertainties and erratic nature of blast loading, current approximations can be tolerated.

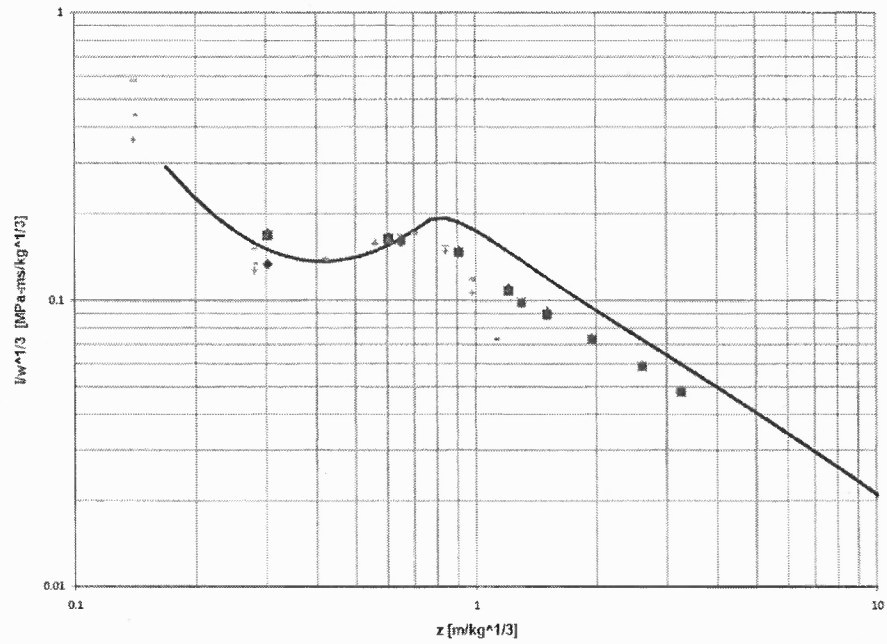


Figure 4.8 Scaled Positive Impulse versus Scaled Distance

Pressure history at standoff 2.00 meter and weight 45.4 kg (grid 5 mm)

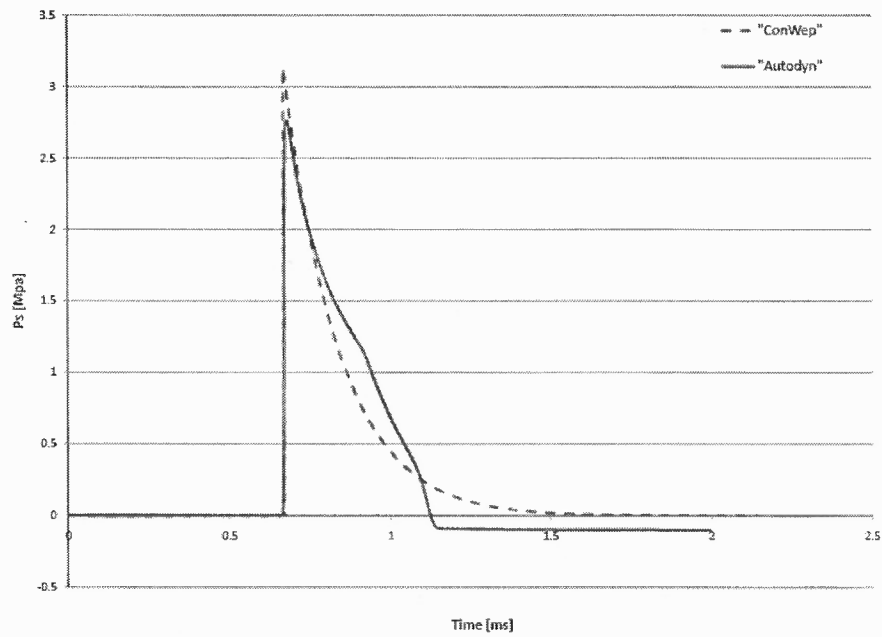


Figure 4.9 Autodyn and ConWep Pressure Time Histories

CHAPTER 5

BLAST LOAD CHARACTERIZATION ON COLUMNS

In Chapter 4, the free air blast modelings are discussed. In this chapter, it is intended to study loading experienced by columns in blast events. To this end, the *shock wave reflection* and *expansion fans* phenomena are used to qualitatively explain the *pressure distribution* around columns with different shapes. The discussion is further confirmed by Autodyn simulations. The pressure distribution study is performed with two dimensional models. Next, to estimate the total *force* and *impulse* on columns, three dimensional models are prepared. Based on the results of the three dimensional simulations, equations have been suggested to estimate force and impulse loads on columns as functions of their size as well as the intensity of the blast load for both circular and square columns.

5.1 Fluid Forces on Solid Objects

There are two mechanisms by which fluid forces are transmitted to a solid object submerged in the fluid flow; they are namely pressure p and shear stress τ . Considering an infinitesimal surface area da on which pressure p in normal direction $\mathbf{n} = (n_x, n_y, n_z)$ and shear τ in tangential direction $\mathbf{m} = (m_x, m_y, m_z)$ are present, the total force acting on the area is:

$$d\mathbf{f} = -p\mathbf{n}da + \tau\mathbf{m}da$$

In other words, $d\mathbf{f}$ is the infinitesimal force due to traction $\mathbf{t} = \mathbf{T}\mathbf{n}$ on the area da . The total force \mathbf{f} on the object is the sum of the elemental forces $d\mathbf{f}$ over the object's

surface $\partial\Omega$:

$$\mathbf{f} = \int_{\partial\Omega} d\mathbf{f} = - \int_{\partial\Omega} p \mathbf{n} da + \int_{\partial\Omega} \tau \mathbf{m} da$$

Assuming the fluid flows in x-direction, in aerodynamics terminology, the component of the force \mathbf{f} along the wind (flow) direction (f_x) is called *drag* D ; while *lift* L is the component perpendicular to the wind (flow) direction (say f_y):

$$D = \underbrace{- \int_{\partial\Omega} p n_x da}_{\text{pressure drag}} + \underbrace{\int_{\partial\Omega} \tau m_x da}_{\text{skin friction drag}}$$

$$L = \underbrace{- \int_{\partial\Omega} p n_y da}_{\text{pressure lift}} + \underbrace{\int_{\partial\Omega} \tau m_y da}_{\text{skin friction lift}}$$

In above equation for drag D , both contributions from *pressure drag* and *friction drag* are present. However, in lift, the major contribution comes from *pressure lift* and contribution from shear stress on lift is usually negligible in engineering applications. For inviscid fluid with viscosity $\mu = 0$, shear stress vanishes and drag and lift contain only pressure components:

$$D = - \int p n_x da \quad (5.1)$$

$$L = - \int p n_y da \quad (5.2)$$

Drag force in practical applications is approximated with following:

$$D = C_D \frac{1}{2} \rho_\infty u_\infty^2 A$$

in which ρ_∞ , u_∞ are free-stream density and velocity measured in far upstream and A is a reference area for the object which is the *planform area* i.e. the projected area as seen by the flow. C_D is *drag coefficient*

In compressible flow context, it can be shown via dimensional analysis that drag coefficient only depends on free-stream Mach number M_∞ and specific heat ratios γ [1].

$$C_D = f(M, \gamma)$$

Drag coefficient does not depend on the size of the body (not shape), nor the free-stream density, pressure, or velocity.

5.2 Fluid Flow Around a Solid Object

The flow field - streamlines - in the presence of a solid object will vary depending on the flow regime, i.e. *subsonic* or *supersonic*. Different regimes affect the flow field around the body. A comparison between flow fields in subsonic and supersonic flow streamlines is shown in Figure 5.1.

As observed, in the subsonic flow, i.e. where Mach number is smaller than unity $M = u/a < 1$, the presence of the body propagates everywhere in the flow, including upstream through sound waves. The disturbance due to presence of the object can propagate in all directions including upstream since sound speed a is larger than fluid particle velocity u . Consequently, streamlines in a subsonic flow regime are forewarned of the disturbance and they prepare to conform to the body's geometry in advance.

On the other hand, in a supersonic flow where Mach number is larger than unity $M = u/a > 1$, sound waves can no longer propagate upstream, since flow particles travel toward down-stream faster than sound waves; as a result, streamlines at upstream are not aware of the disturbance. Fluid particles continue their path as though no disturbance is present until a short distance ahead of the body; then

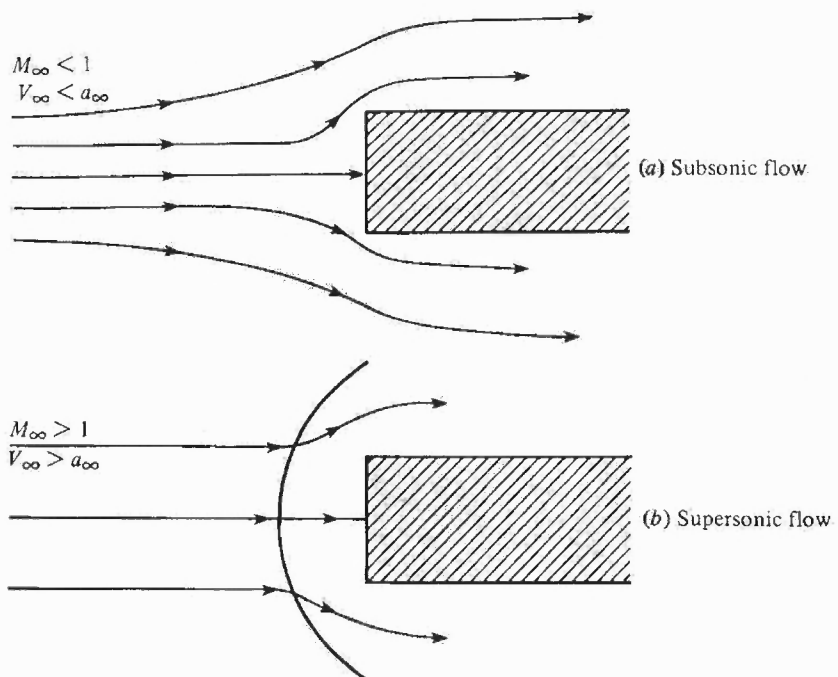


Figure 5.1 Subsonic and Supersonic Flow Field Around a Rectangular Object [1]

streamlines are forced to change their path abruptly to conform to the body. The abrupt change (discontinuity) in the flow field happens via a thin layer of shock wave. It should be noted that the flow renders subsonic after passing through the shock.

5.2.1 Supersonic Flow Over a Corner

The main thrust of this chapter is to investigate the flow field around columns in supersonic regime. Before studying the flow around an object with arbitrary shape like columns, it is helpful to examine the supersonic flow over a corner. Depending on whether the corner is bent upward or downward, two very different flow fields are observed over the corner as depicted in Figure 5.2.

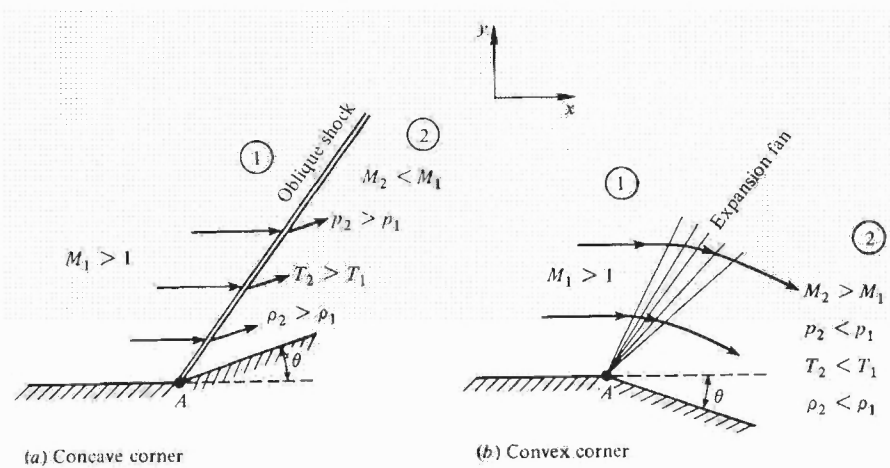


Figure 5.2 Flow Over Concave(a) and Convex(b) Corners.

In a concave corner, when a supersonic flow is turned into itself, an *oblique shock* develops and pressure, density and temperature of the flow increases. Different types of oblique shock reflection (regular and irregular reflections) have been discussed exhaustively in Courant [7].

Conversly, when a supersonic flow is turned away from itself through a convex corner, an *expansion fan* occurs and consequently pressure, density and temperature

decrease smoothly through the expansion fan.

Since shock waves increase the intensity of the flow, they are more of concern rather than expansion fans in blast loading context. On the other hand, expansion waves are imperative when blast waves reach the convex corner of the columns. Expansion waves considerably decrease the strength of the shock waves. In following, a brief review of the theory of oblique shocks and expansion fans are presented.

Oblique Shock: When a supersonic flow sweeps over a concave corner with a deflection angle of θ , following observations can be made: (subscripts 1, and 2 denote states of fluid before and ahead of the shock wave respectively)

- Mach number of the flow decreases through an oblique shock. $M_2 < M_1$
- Pressure, density, and temperature increase through a shock wave. $p_2/p_1 > 1$, $\rho_2/\rho_1 > 1$, $T_2/T_1 > 1$

specifically, it can be shown the pressure increases as following:

$$\frac{p_2}{p_1} = 1 + \frac{2\gamma}{\gamma + 1}(M_{n1}^2 - 1)$$

where, $M_{n1} = M_1 \sin \beta$, and β denotes the obliquity of the reflected shock; it is possible to prove the following relation holds among $\theta - \beta - M$:

$$\tan \theta = 2 \cot \beta \frac{M_1^2 \sin^2 \beta - 1}{M_1^2(\gamma + \cos 2\beta) + 2}$$

The $\theta - \beta - M$ curves for a number of values of M_1 is depicted in Figure 5.3; as observed, for a specific value of M_1 , there is a maximum deflection angle θ_{max} . If $\theta > \theta_{max}$, then no solution exists for a straight oblique shock wave; in contrast the shock will be curved and detached. It should be mentioned that closed form solution does not exist for detached shocks to obtain the flow properties; the only resort to

calculate the flow properties and obtain the curved geometry of the shock including the detachment length is via employing numerical simulations.

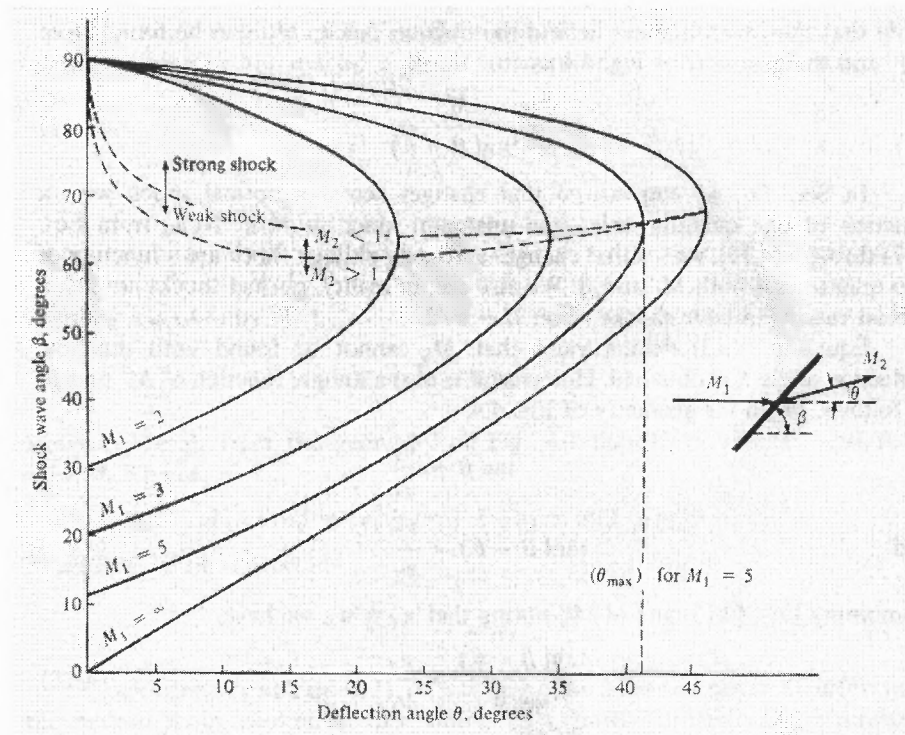


Figure 5.3 $\theta - \beta - M$ Curves.

Expansion Waves: When a supersonic flow is turned away from itself via a convex corner with deflection angle of θ , an expansion wave is formed as shown in Figure 5.2. An expansion wave is directly in contrast with a shock wave. Some distinguishing features of flow through an expansion wave are:

- Mach number of the flow increases through an expansion wave. $M_2 > M_1$
- Pressure, density, and temperature decrease through an expansion wave. $p_2/p_1 < 1$, $\rho_2/\rho_1 < 1$, $T_2/T_1 < 1$

Due to the work of Prandtl and Meyer on developing theory on the subject of expansion waves, expansion waves are also referred to as Prandtl-Meyer expansion waves. When an expansion wave originates from a sharp convex corner, it is called a *centered* expansion fan.

The properties of the flow downstream the expansion fan p_2, ρ_2, T_2, M_2 are obtained provided the upstream flow properties are known. The downstream Mach number M_2 is implicitly calculated from

$$\nu(M_2) = \nu(M_1) + \theta \quad (5.3)$$

where $\nu(M)$ is the Prandtl-Meyer function:

$$\nu(M) = \sqrt{\frac{\gamma+1}{\gamma-1}} \tan^{-1} \sqrt{\frac{\gamma-1}{\gamma+1}(M^2-1)} - \tan^{-1} \sqrt{M^2-1}$$

After solving for M_2 from Equation 5.3, obtaining other quantities is straight-forward, for instance pressure can be obtained from:

$$\frac{p_1}{p_2} = \left[\frac{1 + \frac{\gamma-1}{2} M_2^2}{1 + \frac{\gamma-1}{2} M_1^2} \right]^{\gamma/(\gamma-1)} \quad (5.4)$$

5.3 Flow Field Around Column Sections

5.3.1 Qualitative Discussion

Based on the discussions on oblique shock and expansion fans mentioned in the preceding sections, it is possible to qualitatively describe the flow field around columns with different cross-sectional shape. Here, columns with square and circular shapes are considered. The orientation of the square column to the blast source will affect the flow field. Hence, two different *orientations* or *angles-of-attack* will be discussed for square column as shown in Figure 5.4. In first case, column is oriented side-wise with regard to the charge; while in second case, vertex of the column is facing the charge.

The former square column represents zero angle-of-attack and the latter represents the 45° angle-of-attack.

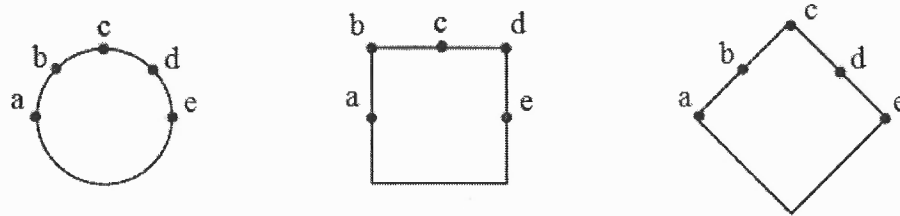


Figure 5.4 Circular Column and Square Columns in 0 and 45° angles-of-attack

Flow Field Around Square Columns: A sketch of the square column with zero angle-of-attack is shown in Figure 5.5. As the incident shock wave encounters the column, a reflected shock bounces off the column; the front face of the column continue experiencing high reflected pressures, until the shock front reaches the two corners. Afterwards, shock wave fans out at the corners and substantially loses its strength. Relief waves (or rarefaction waves) propagates back to the front side and alleviate pressure on the front side.

While the pressure on the lateral sides are much less intense compared with front side, they also cancel out each other. It is worth mentioning that the lateral dimension of the rectangular column is not affecting forces experienced by the column. Those simulations performed for square columns can be extended to rectangular columns with similar front side dimension. At the back corners, again expansion fans develop and the pressure on the back side is very small. The idealized pressure load on the square column is depicted in Figure 5.5.

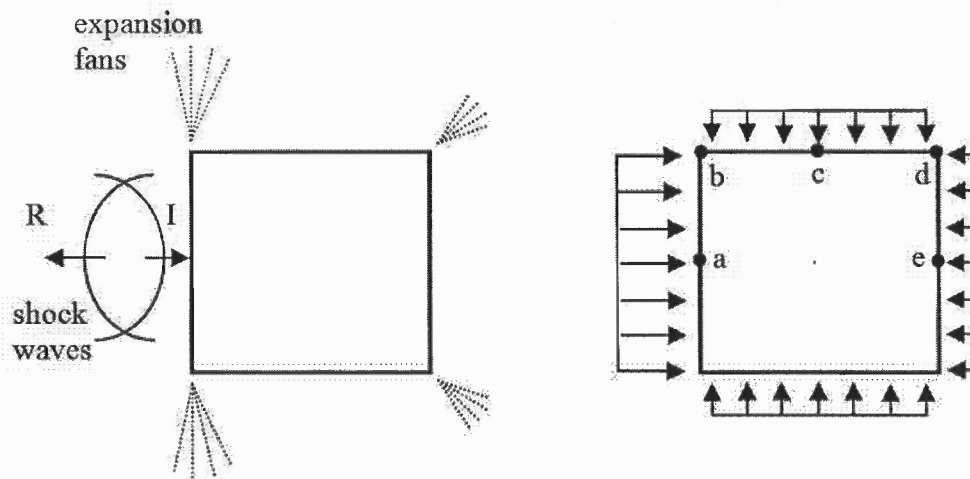


Figure 5.5 Qualitative Flow Field Around a Square Column and Idealized Pressure Distribution

Flow Field Around Rotated Square Columns: A sketch of the 45° rotated square column is depicted in Figure 5.6. In this situation, as incident wave impinges on the column, oblique reflections develop. Comparing oblique reflection with normal reflection occurred in zero angle-of-attack orientation, the pressure on the two sides are less intense; hence the rotated column experience less intense pressures relatively. The shock waves are trapped before the column, until they sweep the two front sides and find their ways to the two back sides. Afterwards, expansion waves develop at the corners and the pressure decrease on two back sides markedly. The idealized pressure on rotated square is shown in Figure 5.6.

Although, pressures are expected to be less intense comparing with zero angle-of-attack orientations, the reference area for rotated square is $\sqrt{2}$ times larger than the area of that of the column with zero angle-of-attack. In terms of total force experienced by the column, the larger area considerably offsets the reduction in pressure and forces on the two cases are almost comparable.

The reflected pressure ratio for different angles of incidents was shown in Figure

1.6. As seen, the reflected pressure ratio for normal reflection ($\alpha_I = 0$) for the most intense incident pressure reads slightly larger than 12. Also, for angles-of-attack around 45° , reflected pressure ratio varies from 8 to 9. The reduction in reflected pressure for rotated square is about 30% which is well compensated with 40% larger area when comparing force on square and rotated square columns.

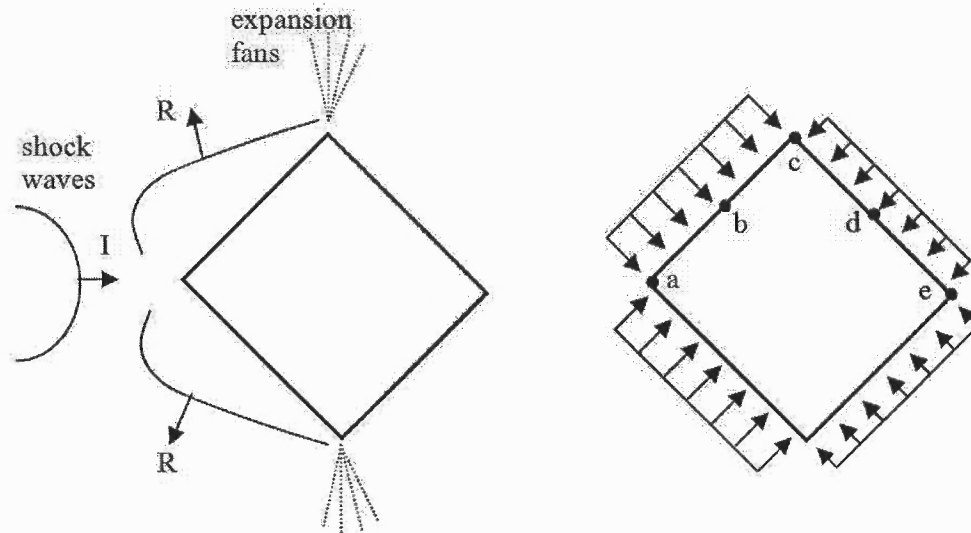


Figure 5.6 Qualitative Flow Field Around a Rotated Square Column and Idealized Pressure

Flow Field Around Circular Columns: Due to the unique geometry of the circular columns, the wave reflections and expansions at each point occur simultaneously. After shock wave reaches the crown of the circular section, then wave expansion is the dominant phenomenon. In all circular and rectangular columns, the reflected shocks are expected to be detached and consequently using numerical modeling is the tool at our disposal.

5.3.2 Quantitative Discussion

In the previous section, flow field developed around column sections were discussed qualitatively. In this section flow fields around different cross sections are further studied with numerical simulations. The objective of simulations are to understand the pressure distribution around column sections; hence, modelings are performed in two-dimensional domain. However, in the next section, the simulations will be performed in three-dimensional domain to study the effects of the height of columns on the force and impulse imparted to the columns.

Cross sectional shape of a column determine the flow field and pressure distribution around the column perimeter. To evaluate the effects of shape on shock wave loading of columns, two-dimensional simulations of circular and square columns under similar scenarios of explosion – i.e. similar scaled distance z – have been performed and pressure distribution over cross sections are monitored.

Here, the charge is assumed as a point and the incident shock will propagate as concentric circles. In theories that mentioned in preceding sections, the incident shock wave are assumed as planar wave for simplicity. In following simulations, the results of the one-dimensional blast detonation of $w = 45.4 \text{ kg}$ of TNT are mapped into two-dimensional domain as initial condition. The clear stand-off distance in all simulations is $R = 2000 \text{ mm}$ which corresponds to a scaled distance of $z = 0.561 \text{ m/kg}^{\frac{1}{3}}$.

In terms of geometry, the diameter of the circular column is 1000 mm ; and the dimension of the square is $1000 \times 1000 \text{ mm}$. A sketch of column sections is shown in Figure 5.7

Since the charge is located on the symmetric axis of columns, it is possible to model only half of the domain provided appropriate symmetry boundary condition is prescribed. The air domain is discretized with Eulerian grids as small as $20 \times 20 \text{ mm}$.

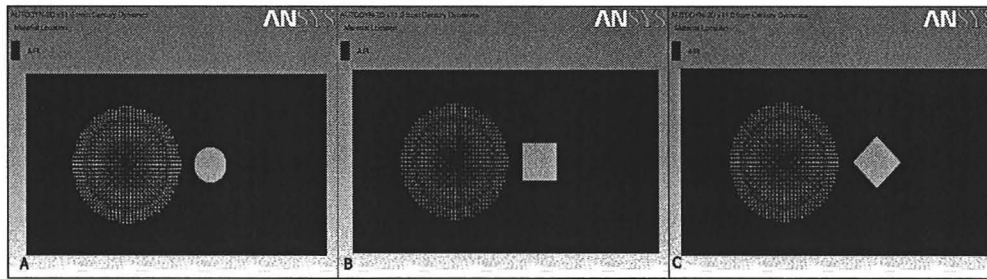


Figure 5.7 Circular Column(A), Square Column(B), and Rotated Square Column(C)

In order to record pressure history in different locations adjacent to the columns, a number of gauge points are embedded in each simulation. The number and location of gauges are reported for each model.

Flow Field Around Circular Columns: Here, blast wave loading on a circular column with diameter of 1000 mm is simulated. A sketch of the domain along with locations of gauges is presented in Figure 5.8. Also, Table 5.1 shows the peak overpressure and impulse at gauge points for circular section. Based on these results, the front points of the section - gauge 1, 2, and 3 - are experience high reflected pressure values, while the points on the back side are experiencing relatively low pressures due to the expansion fans starting to occur at point 5. The isobar contours at different time instants are depicted in Figure 5.9, and 5.10. The reflected shock front are well captured. Also, it is worth noting that it takes less than 2 ms for the shock wave to completely engulf the column.

Flow Field Around Square Column In this simulation, the flow around a square column with dimensions of 1000 by 1000 mm is calculated. The geometry of the problem is depicted in Figure 5.11.

To obtain history of the quantities that we are interested in, seven gauges have

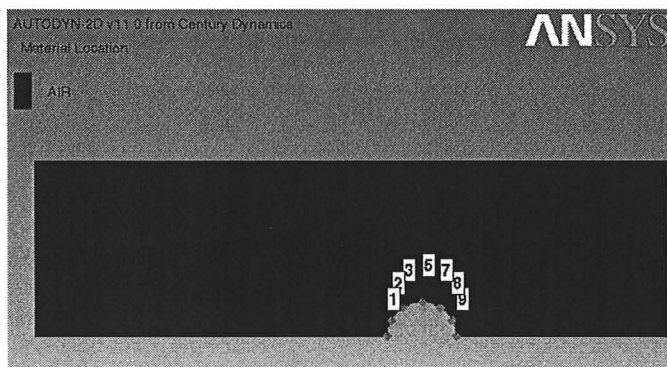


Figure 5.8 Gauge Locations in Circular Column

Table 5.1 Peak Overpressure and Impulse for Circular Column

Gauge no.	Pressure [MPa]	Impulse [kPa-s]
1	17.904	5.288
2	14.277	3.955
3	7.713	1.815
5	1.934	0.472
7	0.836	0.243
8	0.440	0.258
9	0.822	0.481

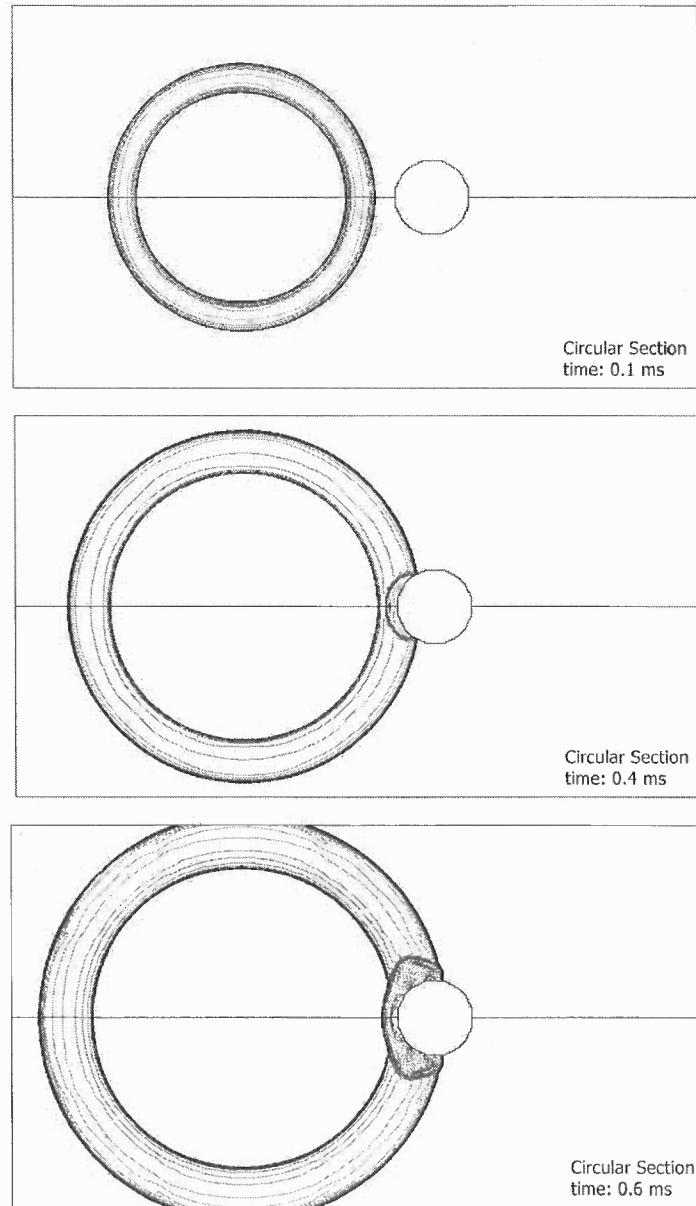


Figure 5.9 Shock Wave Propagation Around Circular Column

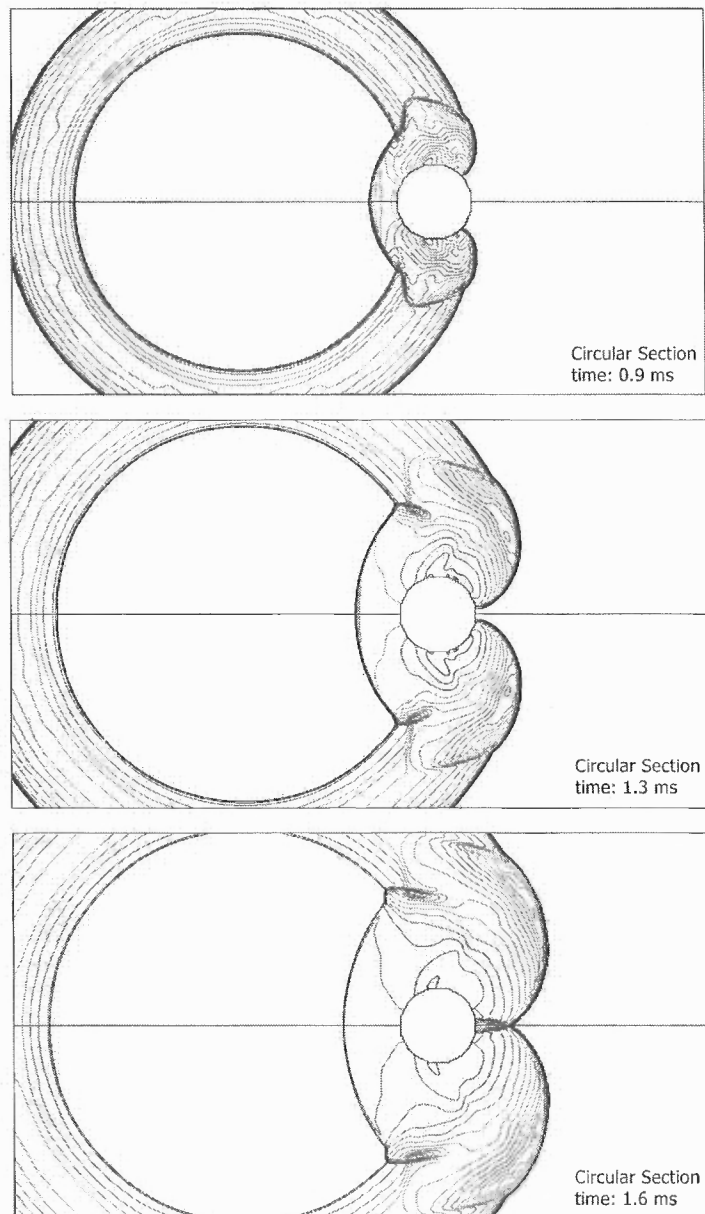


Figure 5.10 Shock Wave Propagation Around Circular Column (Continued)

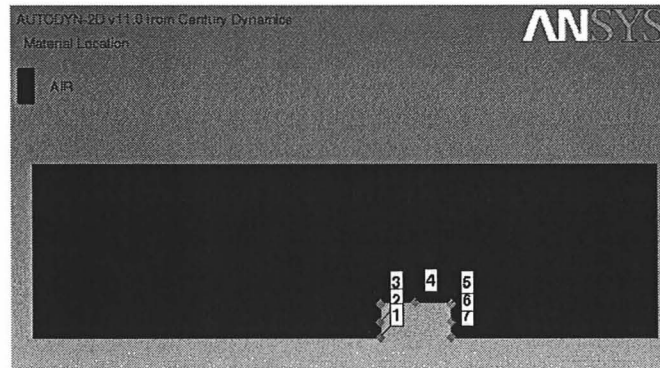


Figure 5.11 Gauge Locations in Rectangular Column

been embedded in cells adjacent to the column; gauge locations are shown in Figure 5.11. Gauges labeled as 1 to 3 are located on windward side of the column; gauges 4 and 5 are on lateral side and on leeward side, gauges 6 and 7 are placed. Peak overpressure and impulse are reported for square column in Table 5.2. As observed, the pressure considerably drops on the lateral side due to expansion fan occurs at the corner. The isobar contours around the square columns are depicted in Figure 5.12, and 5.13.

Flow Field around Rotated Square Column: In Figure 5.14, locations of embedded gauges in the 45° degree rotated square column is shown. Overpressure and impulses in gauge points around the 45° rotated square is shown in Table 5.3.

Two-dimensional Simulation Results In order to compare distributions of pressure and impulse on columns surface, five geometrically related points on the surface of the circular and square columns have been picked; pressure and impulse histories at these points are monitored. A sketch of these points is shown in Figure 5.15. As shown, these locations are labeled with a, b, c, d, and e which geometrically correspond to the front, mid front, lateral side, mid rear and rear of each column. The

Table 5.2 Peak Overpressure and Impulse for Square Column

Gauge no	Pressure [MPa]	Impulse [kPa-s]
1	18.065	6.375
2	17.782	6.095
3	15.842	4.048
4	1.977	0.541
5	0.425	0.036
6	0.275	0.236
7	0.618	0.398

Table 5.3 Peak Overpressure and Impulse for Rotated Square Column

Gauge no.	Pressure [MPa]	Impulse [kPa-s]
1	11.696	4.572
2	11.380	2.988
3	3.269	0.268
4	0.555	0.163
5	0.686	0.401

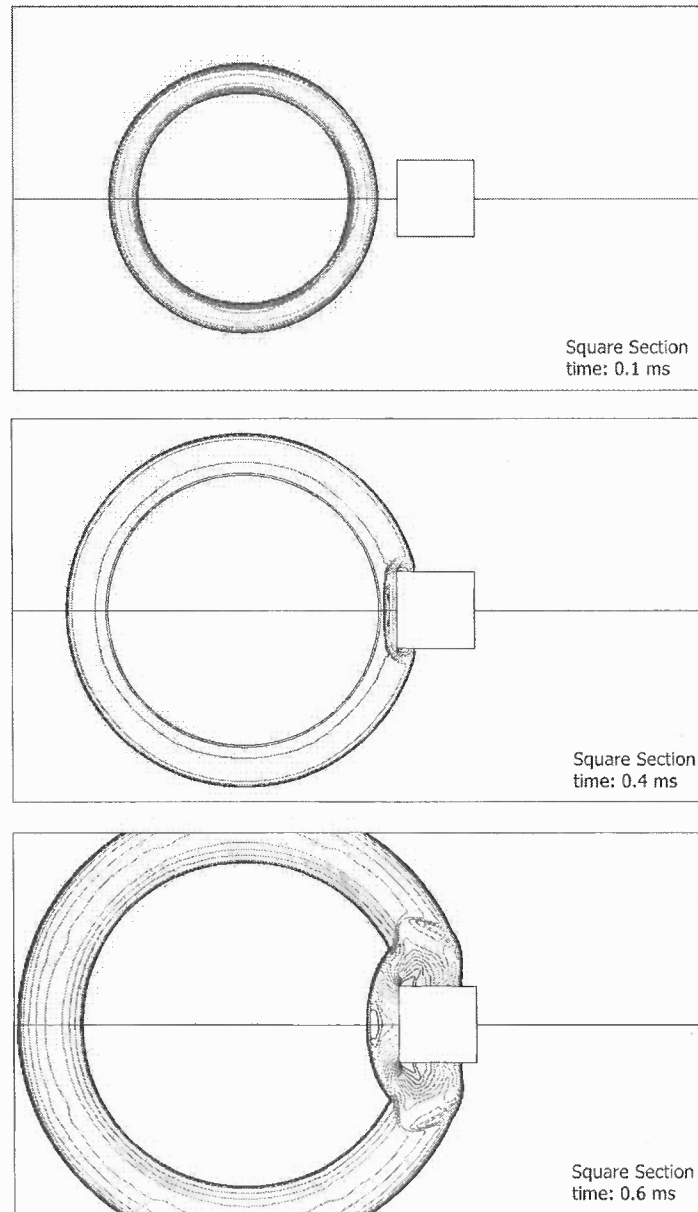


Figure 5.12 Shock Wave Propagation Around Square Column

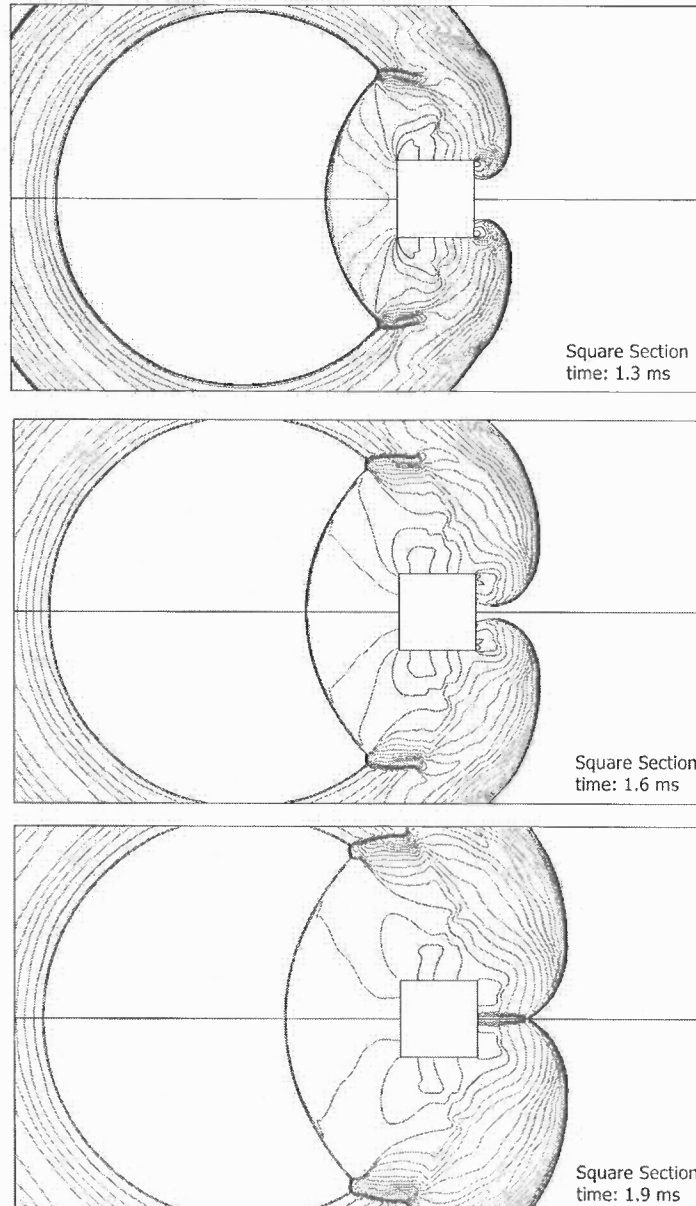


Figure 5.13 Shock Wave Propagation Around Square Column (Continued)

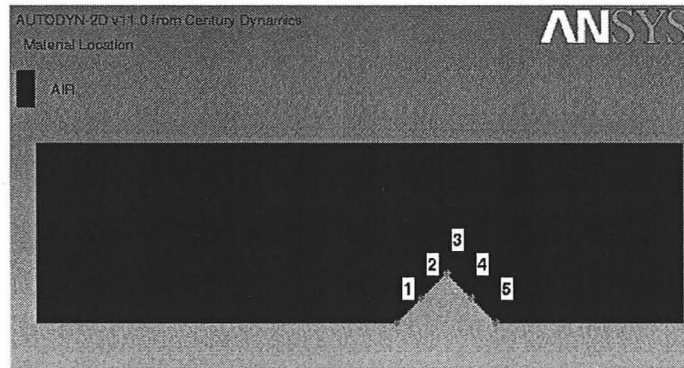


Figure 5.14 Gauge Locations in Rotated Square Column

maximum reflected pressure occurs at point a, while point c represents the pressure values corresponding to expansion waves. The Pressure and impulse histories for points a, b, c, d, and e are shown in Figures 5.16, 5.17, 5.18, 5.19, and 5.20 respectively.

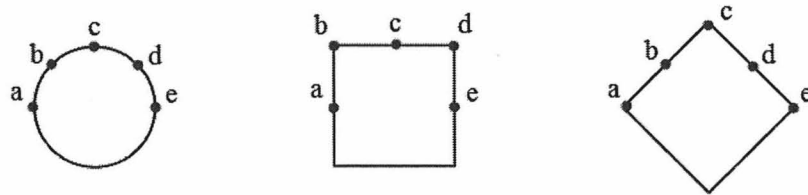


Figure 5.15 Locations of point a, b, c, d, and e.

It is clearly seen that the cross sectional shape and geometry of a column considerably affects the blast wave propagation pattern. Based on the current simulation, following conclusions can be made.

- Peak reflected pressure experienced at the point immediately in front of the blast (point a) by circular and square sections are almost equal; however, there is a 20% reduction in impulse experienced by circular column relative to square.
- Comparing square and rotated square shows that orientation of the column

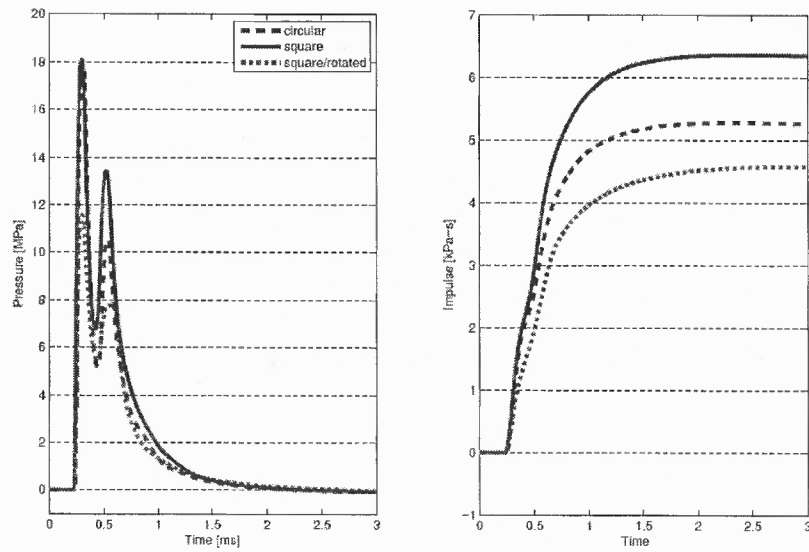


Figure 5.16 Pressure and impulse histories at point “a”

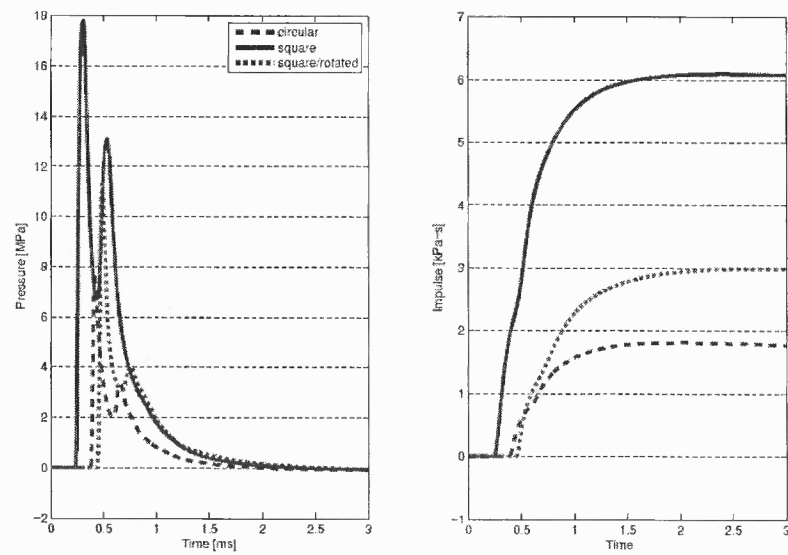


Figure 5.17 Pressure and impulse histories at point “b”

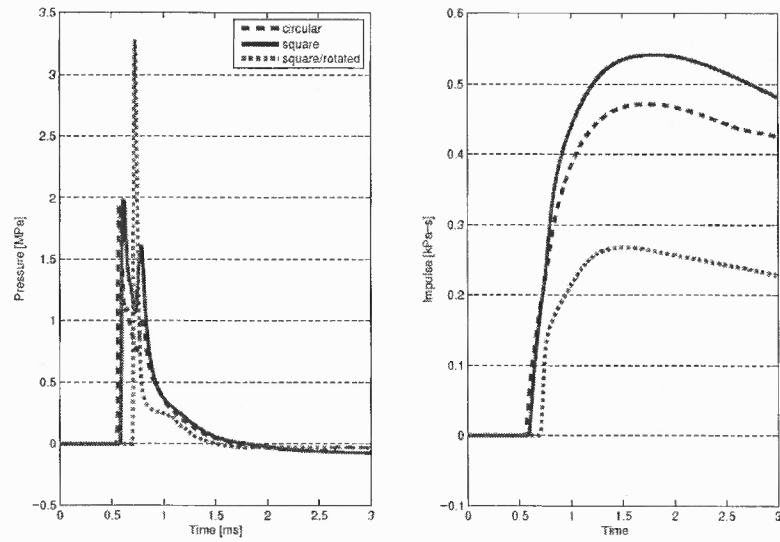


Figure 5.18 Pressure and impulse histories at point “c”

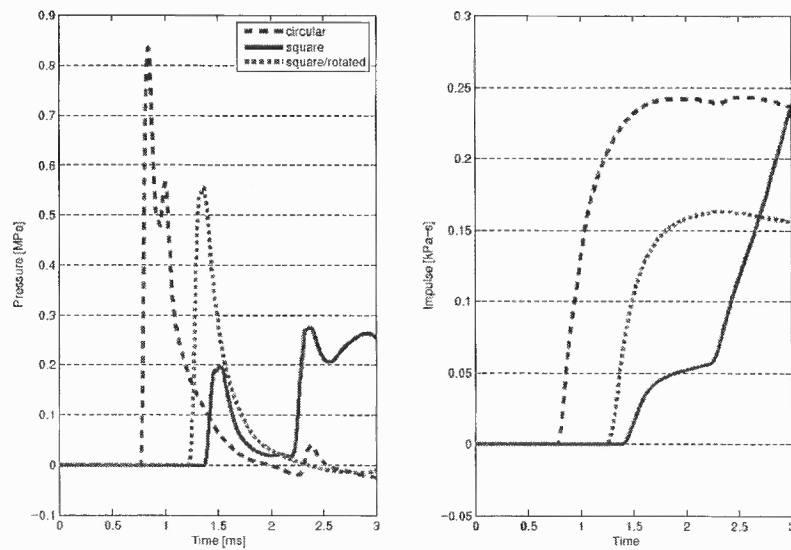


Figure 5.19 Pressure and impulse histories at point “d”

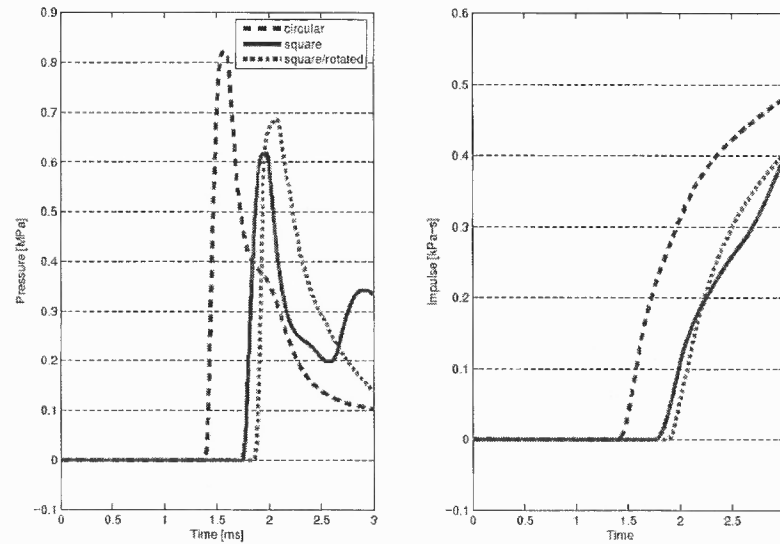


Figure 5.20 Pressure and impulse histories at point “e”

toward the blast has significant effect on pressure and impulse distribution. Rotated square column experiences less pressure and impulse by amounts of 35% and 28% in comparison with square section.

- pressure and impulse built up in rear of columns are negligible in comparison to the front side pressure and impulse as a result of pressure drops due to occurring expansion fans

5.4 Characterizing Blast Loads on Columns

Force and impulse imparted to a column during a blast accident vary with the shape and size of the column as well as with the intensity of the blast. In this section, it is attempted to quantify force and impulse. To achieve this end, a set of simulations with different input parameters are designed to study correlations of force and impulse with shape, size, and intensity. It is tried to propose approximate equations for the force and impulse based on simulation results.

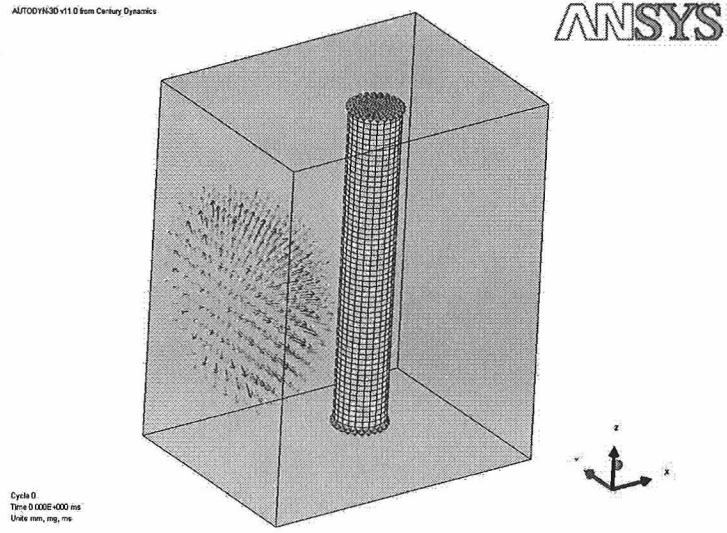


Figure 5.21 3D Modeling of Circular Column

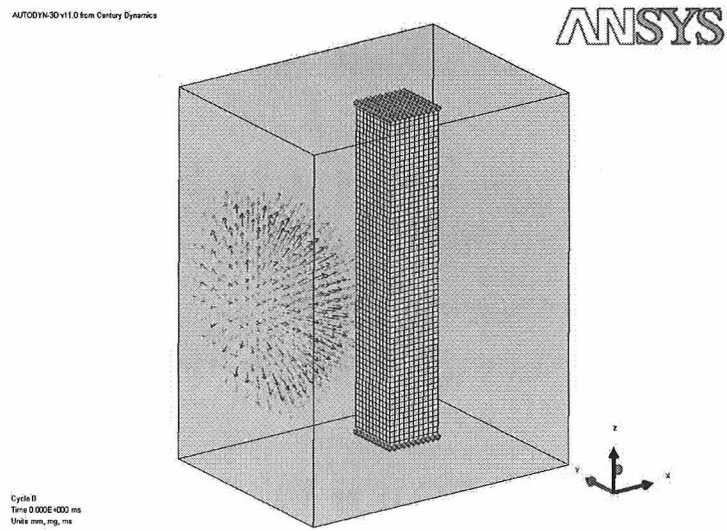


Figure 5.22 3D Modeling of Square Column

5.4.1 Three-Dimensional Simulations

Sketches of typical simulations are shown in Figure 5.21, and Figure 5.22 for circular and rectangular columns respectively. As seen, the column is exposed to a blast wave located at its mid-height level with a specific stand-off distance. The objective is to calculate the force exerted on the column due to the air blast. Assuming the detonation point and column are located on x-axis, the components of the drag f_x and lift f_y at time t are:

$$f_x(t) = - \int_{\partial\Omega} p(t; x, y, z) n_x da$$

$$f_y(t) = - \int_{\partial\Omega} p(t; x, y, z) n_y da$$

in which $\partial\Omega$ represents the outer surface of the column with outward normal vector $\mathbf{n}(x, y)$. The lift force is zero $f_y = 0$, due to symmetry in the loading with respect to the y-axis. So, the only component of force will be the drag force f_x . From now on, the x-subscript will be omitted for sake of simplicity in the notations and drag force will be denoted by f .

Also, another quantity of interest is the impulse $i(t)$ experienced by the column. The impulse is defined as:

$$i(t) = - \int_0^t \int_{\partial\Omega} p(t; x, y, z) n_x da dt \quad (5.5)$$

Impulse will be only due to drag force f_x . In all simulations, the total net *force* and *impulse* imparted to the column is calculated via integration of pressure over the wet surfaces, i.e. column's element surfaces that are in contact with the air domain.

Columns are discretized with Lagrangian hexahedral brick elements as small as 75 mm in size. Columns material is concrete and linear elastic model is used for concrete behavior. The results relevant to structural response of column is studied in

next chapter; here, it suffice to mention that the flexibility of columns has been taken into account in simulations. The air domain is discretized with Eulerian elements as small as 75 *mm* in size. The Flux Corrected Transport (FCT) algorithm is used.

Blast intensity is again represented through scaled distance z , which is a parameter that combines the weight of explosives and stand-off distance in one single number. As mentioned, the explosives are located in the mid-height level of columns with a clear stand-off distance of 2000 *mm* in all simulations. However, the weight of explosives are varying to change scaled distances for each simulation. The weight of explosives used are equivalent of 22.7 *kg* (50.0 *lb*) of TNT, 45.4 *kg* (100.0 *lb*) of TNT, and 113.5 *kg* (250.0 *lb*) of TNT which correspond to scaled distances of $z = 0.706 \text{ m/kg}^{\frac{1}{3}}$, $z = 0.561 \text{ m/kg}^{\frac{1}{3}}$, and $z = 0.413 \text{ m/kg}^{\frac{1}{3}}$ respectively. equal to a car/truck...

Three dimensional modelings are performed to consider the effect of columns' length on loading. In doing so, circular and square shape columns with heights of 3000, 4500, and 6000 *mm* and cross sectional size of 500, 750, 1000 *mm* are studied under the above three scenarios of blast explosions. In total, 54 simulations have been performed (2 shapes \times 3 sections \times 3 heights \times 3 scaled distances.)

5.4.2 Three-Dimensional Simulation Results

In order to investigate the effect of column heights, the results for net force and impulse for similar section size but different height length are shown in Figures 5.23, 5.24, and 5.25 for circular columns and in Figures 5.26, 5.27, and 5.28 for square columns. These results presents the net force and impulse imparted to columns during the blast intensity of $z = 0.561 \text{ m/kg}^{\frac{1}{3}}$. In each Figure, top graph corresponds to net force experienced by columns of different lengths; however, the bottom graph corresponds to net impulse imparted to the mentioned columns. Based on presented simulation results, following observations can be made :

- *Maximum force* imparted to the columns with similar cross sections in terms of shape and size is not sensitive to column heights for the range of heights in this study. This means that height is not a factor in determining the maximum force experienced by the column. Maximum force occurs while certain length of columns are swept by the pressure wave. Apparently, even for the shortest column with height of 3000 mm, the length has been enough for the maximum force to develop.
- *Maximum impulse* experienced by the columns increases as the height of columns increases. In taller columns, pressure wave can sweep larger area and hence more impulse would be experienced by columns.
- In the next chapter, it has been shown the structural response of columns depends on the maximum impulse and not the maximum force. Also, it will be mentioned how the total net force and impulse can be used to predict the maximum deflections.

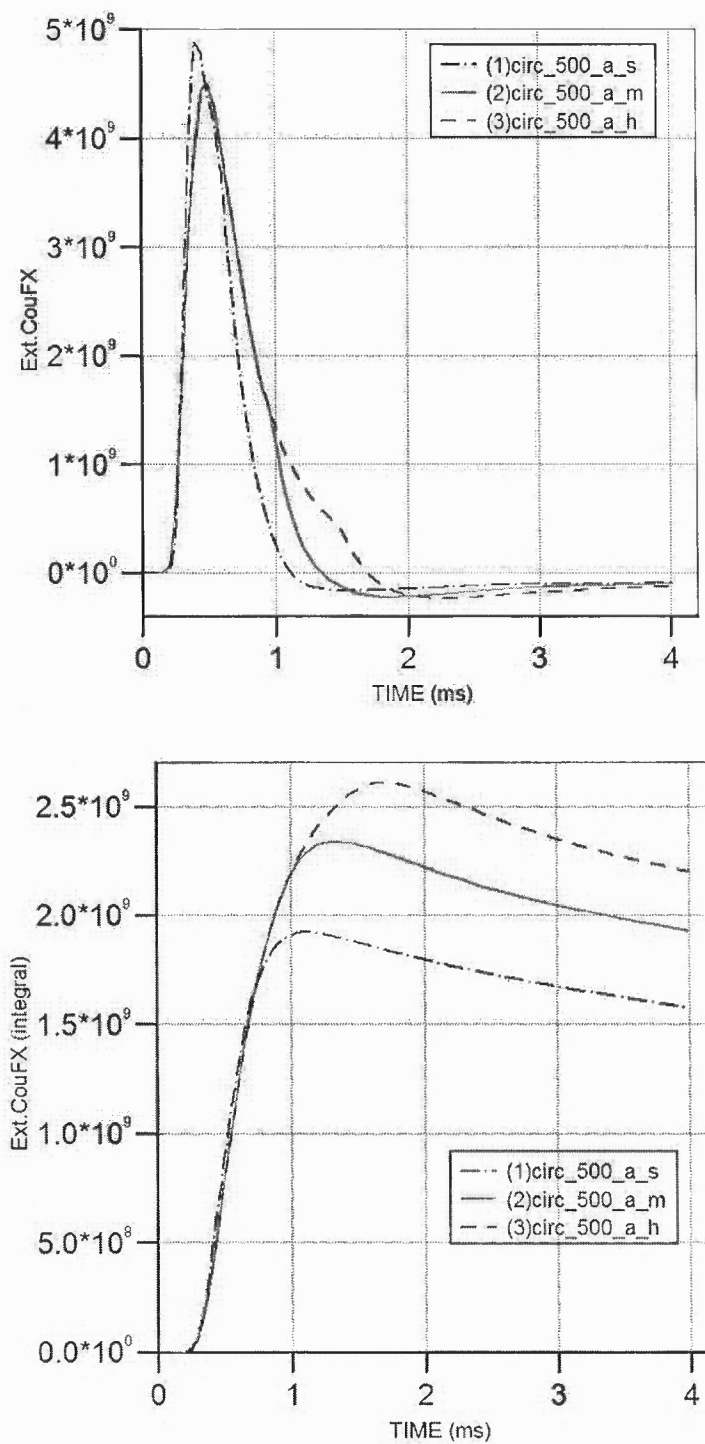


Figure 5.23 Force f (top) and Impulse i (bottom) for Circular Sections with Diameter of 500 mm and Lengths of 3000, 4500, and 6000 mm (denoted as s, m, and h respectively.)

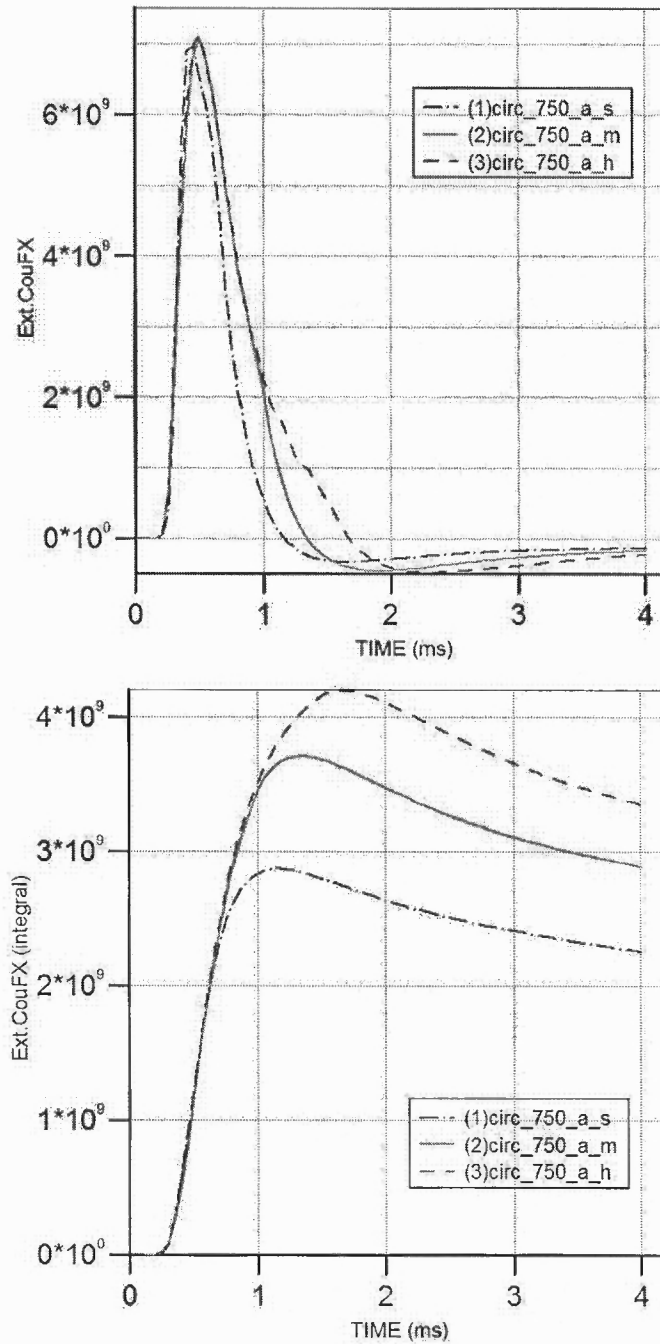


Figure 5.24 Force f (top) and Impulse i (bottom) for Circular Sections with Diameter of 750 mm and Lengths of 3000, 4500, and 6000 mm (denoted as s, m, and h respectively.)

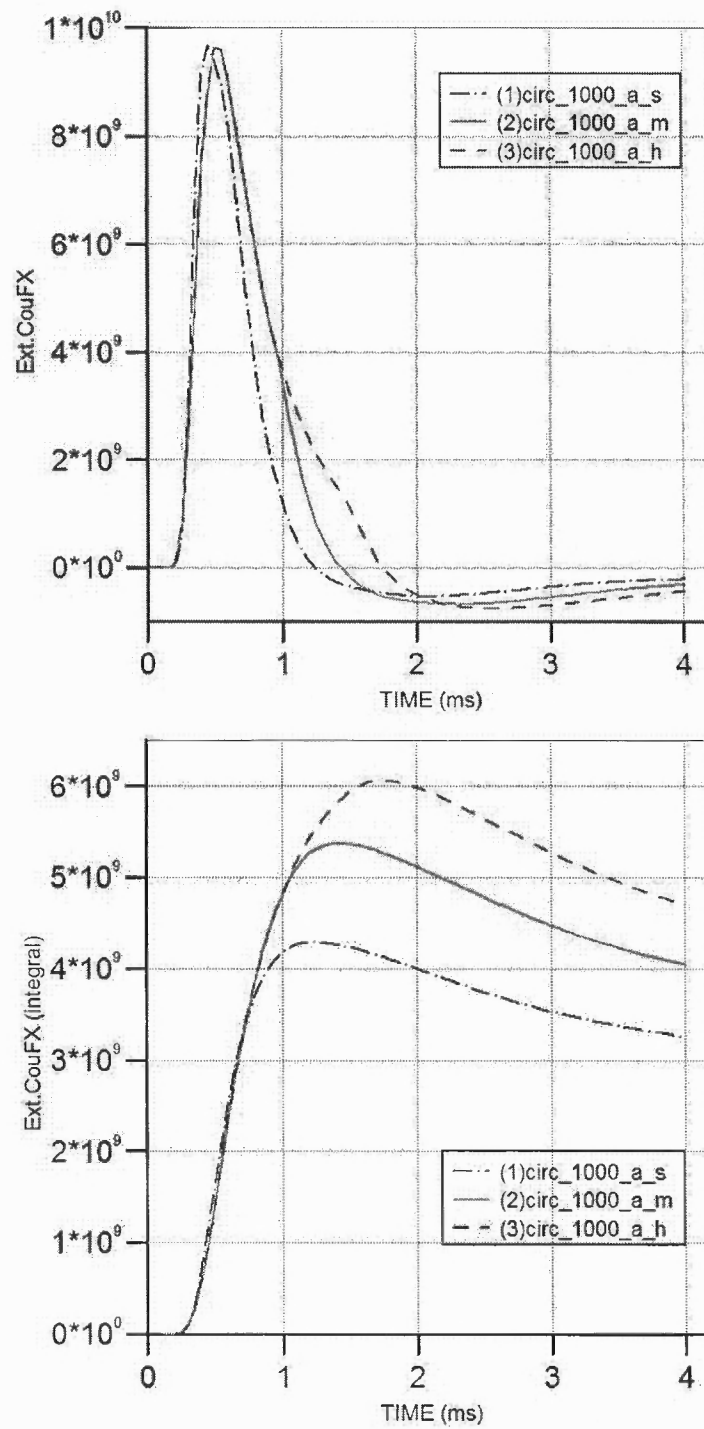


Figure 5.25 Force f (top) and Impulse i (bottom) for Circular Sections with Diameter of 1000 mm and Lengths of 3000, 4500, and 6000 mm (denoted as s , m , and h respectively.)

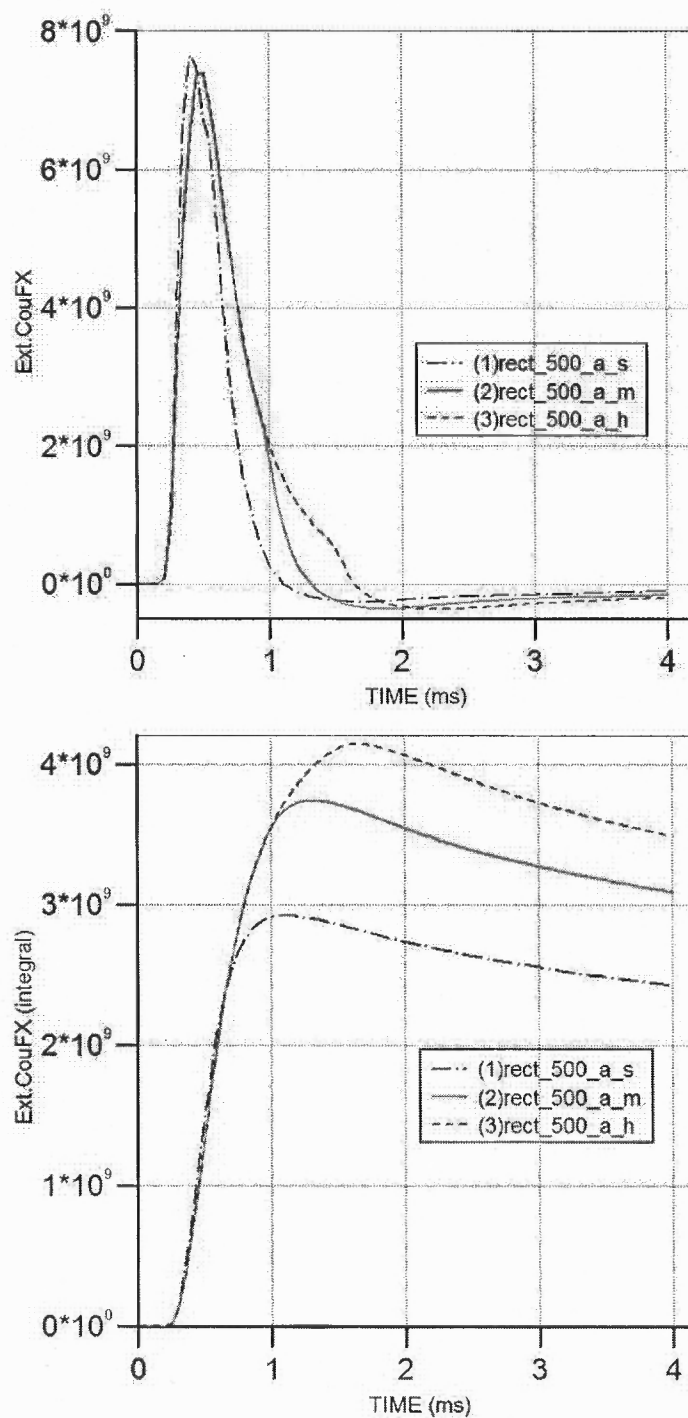


Figure 5.26 Force f (top) and Impulse i (bottom) for Square Sections with Diameter of 500 mm and Lengths of 3000, 4500, and 6000 mm (denoted as s, m, and h respectively.)

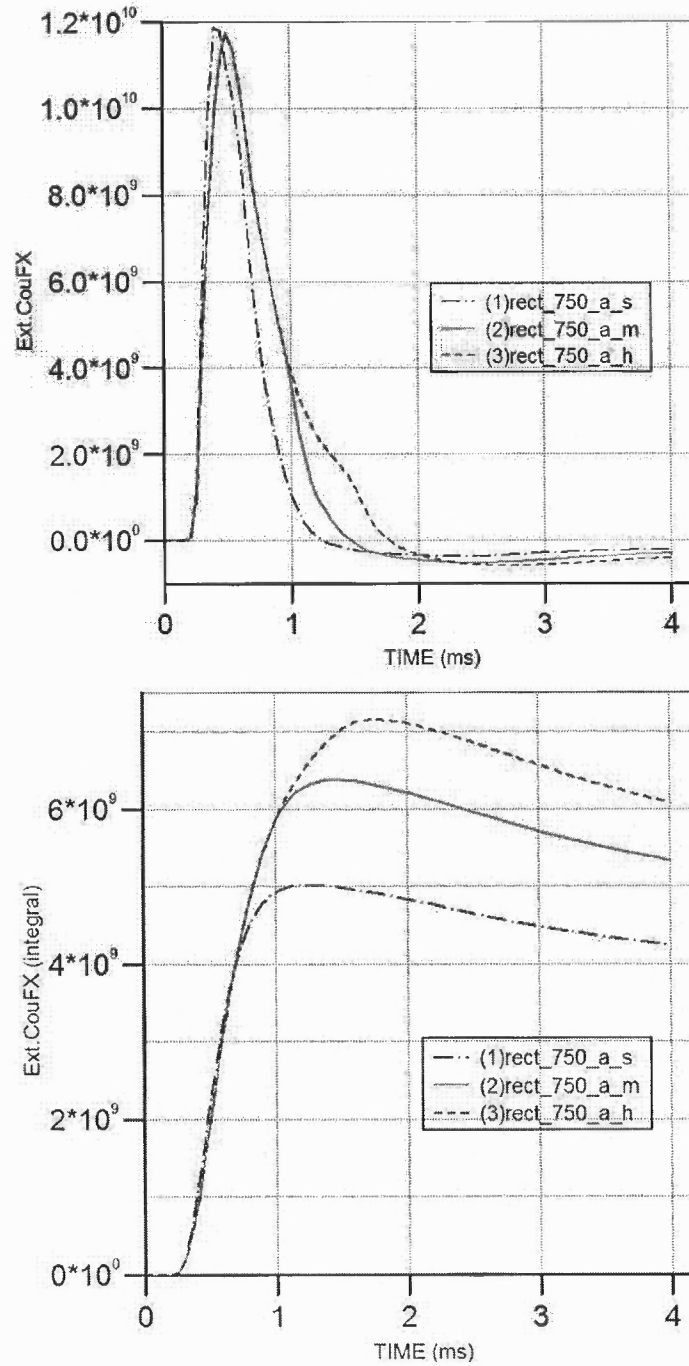


Figure 5.27 Force f (top) and Impulse i (bottom) for Square Sections with Diameter of 750 mm and Lengths of 3000, 4500, and 6000 mm (denoted as s, m, and h respectively.)

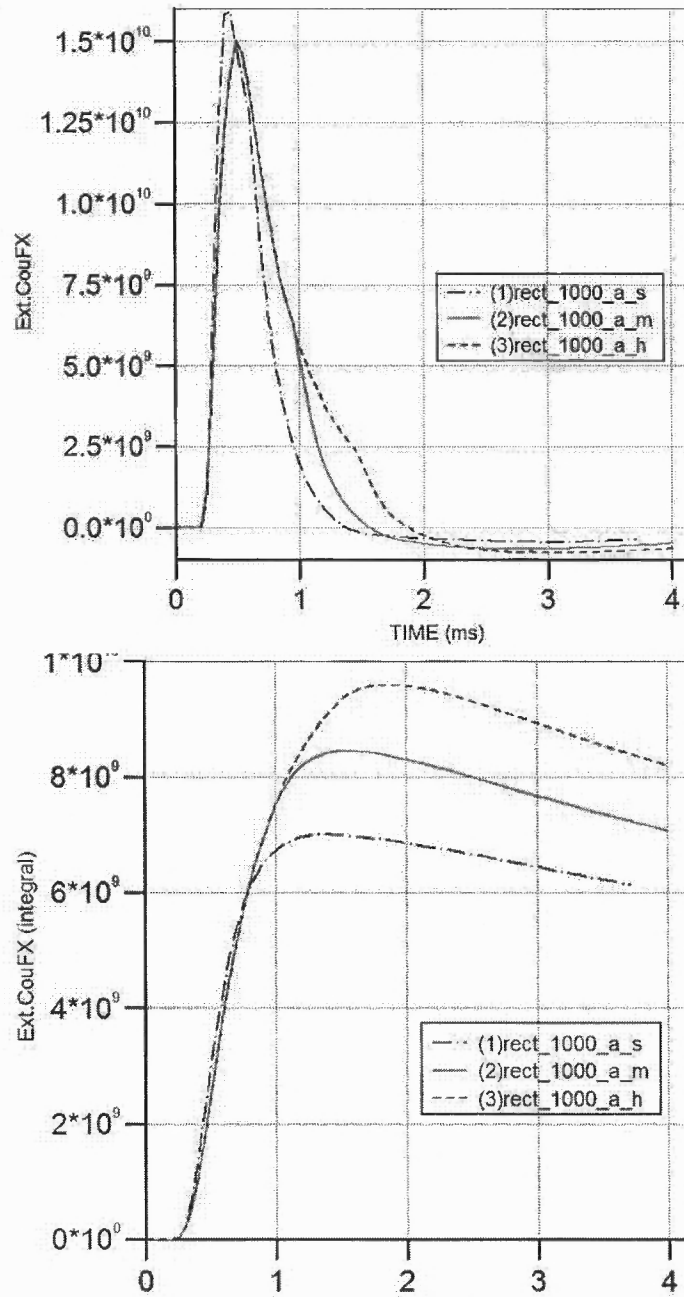


Figure 5.28 Force f (top) and Impulse i (bottom) for Square Sections with Diameter of 1000 mm and Lengths of 3000, 4500, and 6000 mm (denoted as s , m , and h respectively.)

5.4.3 Proposed Equations

In this section, it is tried to find correlations among variables in order to propose equations for force f , and impulse i . The variables include height h , cross-sectional size a , and blast intensity z .

Any formulas proposed for force and impulse values should have certain properties. For instance, force and impulse should diminish while either height or width approach zero; also, as scaled distance z tends to zero (corresponding to very intensive blast), then force and impulse should blow up.

The functional form considered for force $f(h, a, z)$, and impulse $i(h, a, z)$ are assumed to be in the form of multiplication of effects of height, width, and scaled distance. Specifically, it is presumed that force and impulse are proportional to a power of h , and a but inversely proportional to a power of z . For convenience, results are normalized with arbitrary data corresponding to $f_0 = f(h_0, a, z_0)$, and $i_0 = i(h_0, a, z_0)$:

$$\frac{f}{f_0} = \left(\frac{h}{h_0}\right)^\alpha \times \left(\frac{a}{a_0}\right)^\beta \times \left(\frac{z_0}{z}\right)^\gamma \quad (5.6)$$

$$\frac{i}{i_0} = \left(\frac{h}{h_0}\right)^{\alpha'} \times \left(\frac{a}{a_0}\right)^{\beta'} \times \left(\frac{z_0}{z}\right)^{\gamma'} \quad (5.7)$$

in which , values of exponents α, β, γ as well as α', β', γ' should be found from fitting the best curve from the results obtained from simulations. The optimal values for exponents represent the fittest formula for simulation results. For curve-fitting purpose, the sum of squares of errors has been minimized with respect to exponents. The detail of curve-fitting technique has been presented in Appendix A.

The optimal values of exponents for force and impulse equations are shown in Table 5.4, and Table 5.5 respectively. Each table shows optimal exponents for both circular and rectangular sections. As mentioned before, force f , is not sensitive to

Table 5.4 Parameter Values for Force Equation f

cross-section	α	β	γ
Circular	0.	0.9558	2.3059
Rectangular	0.	0.9283	2.4538

Table 5.5 Parameter Values for Impulse Equation i

cross-section	α'	β'	γ'
Circular	0.4775	1.1576	2.1332
Rectangular	0.5024	1.2387	2.1822

column height; accordingly, the exponent for height effects α should be taken as zero.

Comparing the force and impulse experienced by circular and square columns, the square columns usually attract at least 60% more force and impulse compared to the column of circular section. However, when it comes to deflection, rectangular columns benefits from larger section moment of inertia. It will be shown in next chapter that rectangular columns can make up the higher force and impulse with benefiting from better section properties in terms of deflection. This will be elaborated in next chapter.

After obtaining the optimal values for exponents, the simulation results and equation prediction are compared in Table 5.6 for circular sections and in Table 5.7 for square sections. In each Table, the first three columns show the input parameters of height h , cross section size a , and scaled distance z . The fourth and fifth columns report the force f and impulse i obtained from simulations. In the last two columns the f/f_0 and i/i_0 are compared for both simulation and equation predictions. For

circular column, the results are normalized with f_0 and i_0 which are corresponding to:

$$f_0 = f(h_0 = 3000, a_0 = 500, z_0 = 0.706) = 2.88e9 \text{ mN}$$

$$i_0 = i(h_0 = 3000, a_0 = 500, z_0 = 0.706) = 1.18e9 \text{ mN-ms}$$

also, for square columns, the results are normalized with f_0 and i_0 which are corresponding to:

$$f_0 = f(h_0 = 3000, a_0 = 500, z_0 = 0.706) = 4.62e9 \text{ mN}$$

$$i_0 = i(h_0 = 3000, a_0 = 500, z_0 = 0.706) = 1.81e9 \text{ mN-ms}$$

The proposed equations for impulse yield good predictions with an error around 5% or less. The difference between simulations and predictions from equations can reach up to 10%. It will be shown in next chapter that the structural response is impulse-sensitive rather than pressure-sensitive.

For convenience purposes, it is possible to further simplify the equations and substitute for normalizing quantities (those with $_0$ subscripts) as well as rounding exponents. In doing so, following exponents are proposed for force f on circular column $\alpha = 0$, $\beta = 1$, and $\gamma = 2.3$. Additionally for force on square columns, following values are proposed: $\alpha = 0$, $\beta = 1$, and $\gamma = 2.4$. Based on these values both for circular and square column, following approximate equations are suggested for force:

$$f_{\text{O}} = 2.41e6 a z^{-2.3} \text{ mN} \quad (5.8)$$

$$f_{\text{□}} = 3.87e6 a z^{-2.4} \text{ mN} \quad (5.9)$$

Table 5.6 Simulation Results and Equation Prediction for Circular Section.

h	a	z	f	i	$\frac{h}{h_0}$	$\frac{a}{a_0}$	$\frac{z_0}{z}$	$\frac{f}{f_0}$		$\frac{i}{i_0}$	
<i>mm</i>	<i>mm</i>	<i>m/kg^{1/3}</i>	<i>mN</i>	<i>mN - ms</i>				<i>sim</i>	<i>prdct</i>	<i>sim</i>	<i>prdct</i>
3000	500	0.706	2.88E09	1.18E09	1.0	1.0	1.0000	1.00	1.00	1.00	1.00
3000	500	0.561	4.89E09	1.92E09	1.0	1.0	1.2599	1.70	1.70	1.63	1.64
3000	500	0.413	9.97E09	3.93E09	1.0	1.0	1.7100	3.47	3.45	3.33	3.14
4500	500	0.706	2.54E09	1.43E09	1.5	1.0	1.0000	0.88	1.00	1.22	1.21
4500	500	0.561	4.49E09	2.33E09	1.5	1.0	1.2599	1.56	1.70	1.98	1.99
4500	500	0.413	9.29E09	4.64E09	1.5	1.0	1.7100	3.23	3.45	3.93	3.81
6000	500	0.706	2.54E09	1.57E09	2.0	1.0	1.0000	0.88	1.00	1.33	1.39
6000	500	0.561	4.49E09	2.61E09	2.0	1.0	1.2599	1.56	1.70	2.21	2.28
6000	500	0.413	9.29E09	5.25E09	2.0	1.0	1.7100	3.23	3.45	4.45	4.37
3000	750	0.706	4.15E09	1.79E09	1.0	1.5	1.0000	1.44	1.47	1.51	1.60
3000	750	0.561	6.96E09	2.87E09	1.0	1.5	1.2599	2.42	2.51	2.43	2.62
3000	750	0.413	1.45E10	5.62E09	1.0	1.5	1.7100	5.03	5.08	4.76	5.02
4500	750	0.706	3.94E09	2.33E09	1.5	1.5	1.0000	1.37	1.47	1.97	1.94
4500	750	0.561	7.06E09	3.71E09	1.5	1.5	1.2599	2.45	2.51	3.14	3.18
4500	750	0.413	1.49E10	7.22E09	1.5	1.5	1.7100	5.16	5.08	6.12	6.09
6000	750	0.706	3.97E09	2.55E09	2.0	1.5	1.0000	1.38	1.47	2.16	2.23
6000	750	0.561	7.12E09	4.19E09	2.0	1.5	1.2599	2.48	2.51	3.55	3.64
6000	750	0.413	1.49E10	8.21E09	2.0	1.5	1.7100	5.19	5.08	6.96	6.99
3000	1000	0.706	5.62E09	2.68E09	1.0	2.0	1.0000	1.95	1.94	2.27	2.23
3000	1000	0.561	9.67E09	4.29E09	1.0	2.0	1.2599	3.36	3.30	3.64	3.65
3000	1000	0.413	2.04E10	8.15E09	1.0	2.0	1.7100	7.09	6.68	6.91	7.01
4500	1000	0.706	5.27E09	3.39E09	1.5	2.0	1.0000	1.83	1.94	2.87	2.71
4500	1000	0.561	9.62E09	5.37E09	1.5	2.0	1.2599	3.34	3.30	4.55	4.43
4500	1000	0.413	2.05E10	1.01E10	1.5	2.0	1.7100	7.12	6.68	8.56	8.50
6000	1000	0.706	5.27E09	3.78E09	2.0	2.0	1.0000	1.83	1.94	3.20	3.11
6000	1000	0.561	9.62E09	6.06E09	2.0	2.0	1.2599	3.34	3.30	5.14	5.08
6000	1000	0.413	2.05E10	1.15E10	2.0	2.0	1.7100	7.12	6.68	9.77	9.76

Table 5.7 Simulation Results and Equation Prediction for Square Section.

h	a	z	f	i	$\frac{h}{h_0}$	$\frac{a}{a_0}$	$\frac{z_0}{z}$	$\frac{f}{f_0}$		$\frac{i}{i_0}$	
mm	mm	$m/kg^{\frac{1}{3}}$	mN	$mN - ms$				<i>sim</i>	<i>prdct</i>	<i>sim</i>	<i>prdct</i>
3000	500	0.706	4.62E09	1.81E09	1.0	1.0	1.0000	1.00	1.00	1.00	1.00
3000	500	0.561	7.65E09	2.92E09	1.0	1.0	1.2599	1.66	1.76	1.61	1.66
3000	500	0.413	1.67E10	5.82E09	1.0	1.0	1.7100	3.61	3.73	3.21	3.22
4500	500	0.706	4.08E09	2.30E09	1.5	1.0	1.0000	0.88	1.00	1.27	1.23
4500	500	0.561	7.38E09	3.74E09	1.5	1.0	1.2599	1.60	1.76	2.06	2.03
4500	500	0.413	1.63E10	7.41E09	1.5	1.0	1.7100	3.53	3.73	4.09	3.95
6000	500	0.706	4.08E09	2.51E09	2.0	1.0	1.0000	0.88	1.00	1.38	1.42
6000	500	0.561	7.38E09	4.14E09	2.0	1.0	1.2599	1.60	1.76	2.28	2.35
6000	500	0.413	1.63E10	8.29E09	2.0	1.0	1.7100	3.53	3.73	4.57	4.57
3000	750	0.706	6.94E09	3.07E09	1.0	1.5	1.0000	1.50	1.46	1.69	1.65
3000	750	0.561	1.18E10	5.02E09	1.0	1.5	1.2599	2.56	2.57	2.77	2.74
3000	750	0.413	2.74E10	1.01E10	1.0	1.5	1.7100	5.93	5.43	5.55	5.33
4500	750	0.706	6.34E09	3.92E09	1.5	1.5	1.0000	1.37	1.46	2.16	2.03
4500	750	0.561	1.17E10	6.37E09	1.5	1.5	1.2599	2.54	2.57	3.52	3.35
4500	750	0.413	2.63E10	1.22E10	1.5	1.5	1.7100	5.70	5.43	6.71	6.53
6000	750	0.706	6.34E09	4.40E09	2.0	1.5	1.0000	1.37	1.46	2.43	2.34
6000	750	0.561	1.17E10	7.15E09	2.0	1.5	1.2599	2.54	2.57	3.94	3.88
6000	750	0.413	2.63E10	1.38E10	2.0	1.5	1.7100	5.70	5.43	7.61	7.55
3000	1000	0.706	9.34E09	4.37E09	1.0	2.0	1.0000	2.02	1.90	2.41	2.36
3000	1000	0.561	1.59E10	7.00E09	1.0	2.0	1.2599	3.45	3.35	3.86	3.91
3000	1000	0.413	3.51E10	1.37E10	1.0	2.0	1.7100	7.58	7.10	7.57	7.61
4500	1000	0.706	8.13E09	5.27E09	1.5	2.0	1.0000	1.76	1.90	2.90	2.89
4500	1000	0.561	1.50E10	8.45E09	1.5	2.0	1.2599	3.25	3.35	4.66	4.79
4500	1000	0.413	3.34E10	1.64E10	1.5	2.0	1.7100	7.22	7.10	9.03	9.33
6000	1000	0.706	8.13E09	5.95E09	2.0	2.0	1.0000	1.76	1.90	3.28	3.34
6000	1000	0.561	1.50E10	9.59E09	2.0	2.0	1.2599	3.25	3.35	5.29	5.53
6000	1000	0.413	3.34E10	1.86E10	2.0	2.0	1.7100	7.22	7.10	10.24	10.78

Furthermore, for impulse imparted to the circular and square columns following equations have been suggested:

$$i_{\circ} = 5780 h^{0.5} a^{1.2} z^{-2.1} \text{ mN-ms} \quad (5.10)$$

$$i_{\square} = 8870 h^{0.5} a^{1.2} z^{-2.2} \text{ mN-ms} \quad (5.11)$$

Comparing the force and impulse imparted to the square and circular columns, it can be observed from above equations that square columns absorb 60% more force and almost 50% more impulse comparing with a circular column with similar size, i.e. height, and section size.

CHAPTER 6

SINGLE DEGREE-OF-FREEDOM MODEL FOR COLUMNS

In this chapter, the procedure to approximate structural members like a column with an equivalent single degree-of-freedom (SDOF) or lumped mass-spring model is discussed with reference to the pioneering work of Biggs [3]. Next, the deflection results of simulations done in Chapter 5 is employed to fine-tune the transformation factors for blast loading.

6.1 Elastic Response of a SDOF to Dynamic Loading

Assuming a SDOF system with mass m and spring stiffness k subjected to a dynamic load $f(t)$; then the equation of motion for position of the mass $v(t)$ reads as following:

$$m\ddot{v} + kv = f(t) \quad (6.1)$$

In blast context, the load $f(t)$ may be idealized by a triangular pulse with positive phase of $T^+ = t_d$, i.e. $f(t) = f_{max}(1 - \frac{t}{t_d})$ for $t \leq t_d$. In Equation 6.1, the left-hand side represents the *total* structural resistance which consists of inertial term $m\ddot{v}$ as well as the elastic restoring force kv . Generally speaking, restoring force may represent a nonlinear inelastic behavior. Restoring force is also known as *resistance function* and denoted with R . So, in Equation 6.1 resistance function is assumed as linear elastic force $R = kv$.

The vibration damping is not included in Equation 6.1 due to the fact that in impulse type loading, the maximum displacement will be reached in a very short time and the damping force can not absorb much energy accordingly.

The response of SDOF described in Equation 6.1 can be divided into two phases.

In phase one, while force is present $t \leq t_d$ the response is forced vibration. However, in second phase, the response will be free vibrations. Provided at-rest state for initial conditions is assumed, then the response $v(t)$ in phase one is:

$$v(t) = \frac{f_{max}}{k} \left(\frac{\sin \omega t}{\omega t_d} - \cos \omega t - \frac{t}{t_d} + 1 \right)$$

where, $\omega = \sqrt{k/m}$; If loading is of very short duration, say $t_d/T < 0.4$, the maximum response occurs during the free vibration phase. Otherwise, maximum response is observed in phase one. The ratio of maximum displacement v_{max} to static displacement v_{st} is known as *dynamic magnification factor* D : [4]

$$D = \frac{v_{max}}{v_{st}} = \frac{v_{max}}{f_{max}/k}$$

Dynamic magnification factor depends only on the ratio of the positive phase t_d to natural period T . Based on t_d/T , three different loading regimes can be identified. Namely, they are *impulsive loading*, *dynamic loading*, and *quasi-static loading*.

$$\left\{ \begin{array}{ll} \text{Impulsive Loading:} & t_d/T < 0.4 \\ \text{Dynamic Loading:} & 0.4 < t_d/T < 4 \\ \text{Quasi-static Loading:} & t_d/T > 4 \end{array} \right.$$

Herein, the maximum deflection for each type of loading will be discussed.

Impulsive loading: This happens when the loading is such quick comparing with the structure's period that the structure does not significantly respond to the loading until the loading is well expired. In Figure 6.1, a schematic representation of impulsive loading and resistance function is included. As seen, it takes much longer time for the resistance function to respond to the loading.

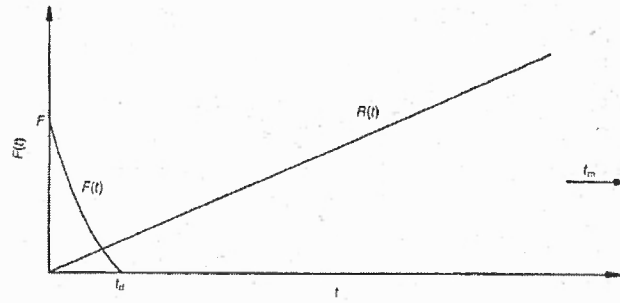


Figure 6.1 Impulsive Loading Compared with Resistance Function [16].

In impulsive loading, the loading changes the momentum of the structure and consequently the structure acquires a velocity of $\dot{v} = i/m$, where i is the impulse. This initial velocity delivers a kinetic energy equal to:

$$\text{KE} = \frac{1}{2}m\dot{v}_0^2 = \frac{i^2}{2m}$$

the strain energy Π stored during maximum displacement v_{max} is:

$$\Pi = \frac{1}{2}kv_{max}^2$$

equating the kinetic energy with the strain energy, maximum displacement is obtained as:

$$v_{max} = \frac{i}{m\omega} \quad (6.2)$$

As observed, in impulsive regime, displacement is a function of the impulse i . The peak of the force f_{max} does not appear explicitly. Equation 6.2 can be specialized for triangular pulse. In this case, impulse is $i = \frac{1}{2}f_{max}t_d$ and Equation 6.2 reduces to:

$$v_{max} = \frac{1}{2} \frac{f_{max}t_d}{m\omega}$$

accordingly, dynamic magnification factor for triangular loading in impulsive regime

will be:

$$D = \frac{v_{max}}{f_{max}/k} = \frac{1}{2}\omega t_d$$

Quasi-static loading: This occurs when positive phase is much longer than natural period T . In the extreme case, load may be considered as almost constant while the structure displaces to its maximum as shown in Figure 6.2, i.e $f(t) \approx f_{max}$. Here, work done on the structure due to the load f is approximated as:

$$WD = f_{max} v_{max}$$

the strain energy is also $\Pi = \frac{1}{2}k v_{max}^2$; equating the work done on the mass with the strain energy and solving for v_{max} :

$$v_{max} = 2 \frac{f_{max}}{k}$$

As seen, the peak deformation is only a function of the peak force $f = f_{max}$ and stiffness k . Also, dynamic magnification factor D for quasi-static loading will be:

$$D = \frac{v_{max}}{f_{max}/k} = 2$$

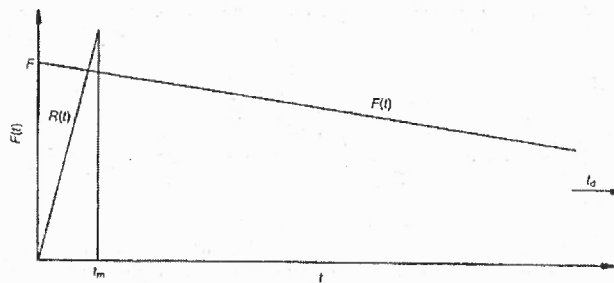


Figure 6.2 Quasi-Static Loading

Dynamic loading: This is observed when the order of the positive impulse is comparable with the period T . The response under dynamic loading depends on the whole time history of the applied load $f(t)$. In this regime, the response can be determined from *shock spectrum* graphs. The shock spectrum for triangular pulse is shown in Figure 6.3 [16]. Shock spectrum provides dynamic magnification factor D for a range of loading durations or ωt_d .

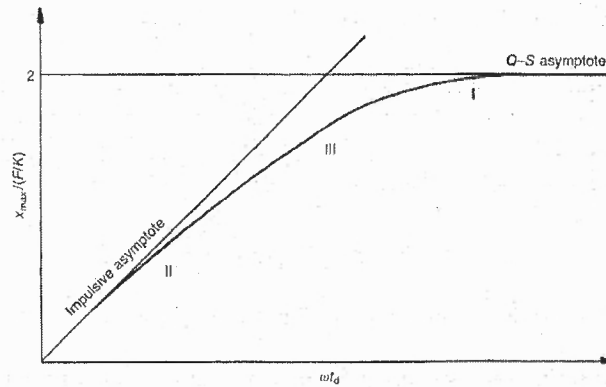


Figure 6.3 Shock Spectrum for Triangular Load

As it was discussed, the dynamic magnification factor D for an impulsive loading is $\frac{1}{2}\omega t_d$. Similarly, for quasi-static response the D would be simply 2. The asymptotes for the two limiting cases are shown in Figure 6.3. In between the limiting cases, the region which is known as dynamic response loading, the whole time history of loading will affect the response; however, the magnification factor D is always less than 2.

6.2 Elastic-Plastic Response of a SDOF to Dynamic Loading

In the preceding section, it was assumed the spring behaves elastically; however, in reality the spring loses its stiffness in relatively large displacements. To consider this issue, an elastic-plastic resistance function R will be adopted, as depicted in Figure 6.4. As seen, after certain elastic displacement v_E , the resistance remains constant

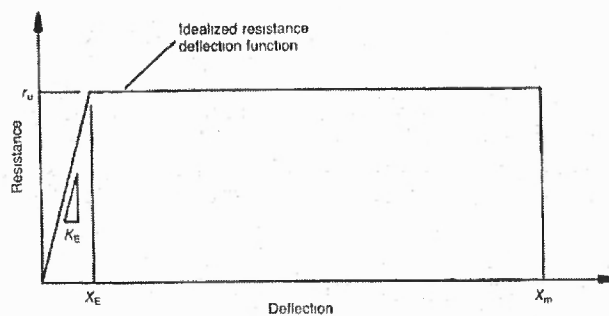


Figure 6.4 Idealized Resistance-Deflection Curve [16]

$R_u = K_E v_E$; also, after certain ultimate deformation v_u , failure occurs. The ratio of $\mu = v_u/v_E$ is known as ductility.

It is again possible to find the response of an elastic-plastic system in limiting cases of impulsive and quasi-static loadings. The only difference in derivation of response compared with elastic response is the strain energy which is calculating the area under the resistance function. For elastic-plastic resistance function, the strain energy is

$$\Pi = R_u(v_u - \frac{1}{2}v_E) = R_u v_E (\mu - \frac{1}{2})$$

Impulsive response: here, by equating the kinetic energy with strain energy, one can obtain the required ductility μ to withstand a certain amount of impulse.

$$\mu = \frac{v_u}{v_E} = \frac{1}{2} \left(\frac{i^2 \omega^2}{R_u^2} + 1 \right)$$

or equivalently, the required resistance R_u for design purpose is:

$$R_u = \frac{i\omega}{\sqrt{2\mu - 1}}$$

Based on the above, following observations can be made:

- For a system to respond elastically ($\mu = 1$), resistance $R_u = I\omega$ should be

provided.

- For very ductile systems (large μ), required resistance R_u approaches zero.

Quasi-static response: here, the work done on the system $WD = f v_u$ should be equal to the strain energy. Doing so results in the required amount of ductility or the required amount of resistance.

$$\mu = \frac{1}{2(1 - \frac{f}{R_u})} \quad (6.3)$$

$$R_u = f \left(\frac{1}{1 - \frac{1}{2\mu}} \right) \quad (6.4)$$

Based on above, following points are obtained:

- For a system to respond elastic ($\mu = 1$), resistance R_u should be twice of the loading $R_u = 2f$.
- For very ductile systems (large μ), required resistance R_u can be equal to the load.

6.3 Equivalent SDOF

Responses of complex structures can be approximated with an equivalent SDOF. Complex structures with multiple degrees of freedom (MDOF) or distributed mass and stiffness properties like structural members (beam-column, slabs, etc.) can be reduced to an equivalent SDOF in terms of a specific response quantity like maximum deflection. Figure 6.5, shows the SDOF representations of a beam and a one bay frame.

In Clough and Penzien [4], the concept of equivalent SDOF is elaborated under *generalized SDOF systems* and it has been discussed rigorously with general application. However, in blast context, the pioneering work of John M. Biggs (1964) on

equivalent SDOF is well known [3]. Biggs discusses the procedure to transform a member to its equivalent SDOF via defining *transformation factors*.

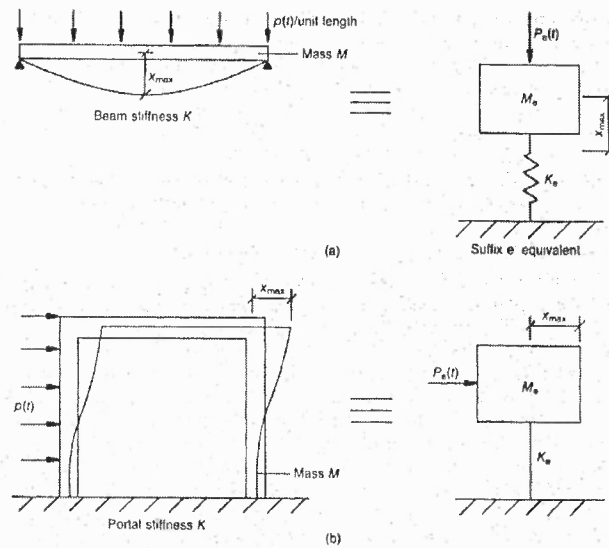


Figure 6.5 Actual and SDOF representation

The equation of motion for the equivalent system is shown as:

$$m_e \ddot{y}(t) + k_e y(t) = f_e(t)$$

where m_e , k_e and f_e are equivalent mass, stiffness and load respectively. In order to find these parameters, the energy components (KE, Π , WD) of the actual structure are equated with those of equivalent SDOF. Next, in order to be able to reduce the actual structure into a SDOF, an approximate *shape function* or *mode shape* like $\phi(x)$ for deformed shape should be adopted. The deflection of actual system is related to the SDOF via:

$$v(x, t) = \phi(x) y(t)$$

Shape functions represent the deflected shape of the actual structure. Also, shape

functions should satisfy geometrical boundary conditions. Moreover, shape function should yield unit displacement at the point of interest which is usually point of maximum deflection like $x = L^*$, i.e. $\phi(L^*) = 1$:

$$v(L^*, t) = \phi(L^*)y(t) = y(t)$$

The shape function can be adopted for example from statically deformed shape.

Having shaping function, then the equivalent quantities can be estimated as:

$$\begin{aligned} m_e &= \int \bar{m}(x)\phi^2 dx \\ k_e &= \int EI(x)\phi''^2 dx \\ f_e &= \int \bar{q}(x)\phi dx \end{aligned}$$

where, $\bar{m}(x)$ is mass per unit length; $EI(x)$ is bending stiffness; and $\bar{q}(x)$ is uniformly distributed load per unit length on the member.

Transformation Factors It is possible to express the equivalent quantities as a ratio of the total/gross quantities of the distributed system via *transformation factors* as:

$$\begin{aligned} m_e &= K_M m \\ k_e &= K_K k \\ f_e &= K_L f, \end{aligned}$$

where K_M , K_K and K_L are mass, stiffness and load factors. For a presumed mode shape $\phi(x)$ and known mass, stiffness and load distributions, the transformation factors become a dimension-less number and hence very convenient to use.

Stiffness k_e being defined as the *force* required to introduce a unit deflection at the equivalent system, then Biggs assumes that the stiffness transformation factor

K_K is equal to load factor $K_K = K_L$. However as shown in Equations 6.5, this is not completely true; since K_e is related to ϕ''^2 but f_e depends on ϕ . Nevertheless, K_L usually provide an acceptable approximation of K_K .

Biggs calculates the transformation factors for a fixed-end beam under uniform pressure f , via presuming a fourth degree polynomial for the mode shape:

$$K_M = \frac{m_e}{m} = \frac{\int \bar{m}\phi^2 dx}{\bar{m}h} = 0.41$$

$$K_L = \frac{f_e}{f} = \frac{\int \bar{q}\phi dx}{\bar{q}h} = 0.53$$

Similarly, for other type of loading and end conditions, the transformation factors are tabulate in Figure 6.6. Also, stiffness is reported in Figure 6.7; as observed, stiffness k can be approximated as $k = \kappa EI/h^3$, where κ depends on support conditions as well as the load distribution. Biggs proposed these factors based on simple yet relatively accurate assumptions and tools available in his time. For example, he approximated the deformed shape with a single polynomial for the whole column, however, it is now possible to get better approximations via using piece-wise connected polynomials (or finite elements) approximations.

In selecting appropriate stiffness and transformation factors, not only assumptions should be made on support conditions but also valid presumption on the blast load distribution should be made. Although Biggs provides transformation factors for concentrated and uniform loading, blast load distribution does not corresponds to either of them. In practice, usually blast load is considered as uniformly distributed over columns or beams. Uniformly distributed assumption underestimates the deflection. On the other hand, assuming blast load as concentrated load at the mid-span proves conservative. For example comparing load factor K_L for columns with both end fixed shows the range of variation of load factors; for concentrated load $K_L = 1$, while, for distributed load $K_L = 0.53$. It is expected that K_L corresponding with

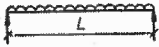
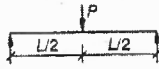
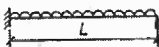
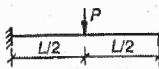
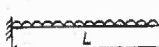
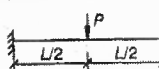

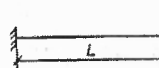
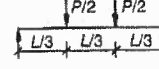
Edge conditions and loading diagrams	Range of behaviour	Load factor K_L	Mass factor K_M	Load-mass factor K_{LM}
	Elastic Plastic	0.64 0.50	0.50 0.33	0.78 0.66
	Elastic Plastic	1.0 1.0	0.49 0.33	0.49 0.33
	Elastic Elasto-plastic Plastic	0.58 0.64 0.50	0.45 0.50 0.33	0.78 0.78 0.66
	Elastic Elasto-plastic Plastic	1.0 1.0 1.0	0.43 0.49 0.33	0.43 0.49 0.33
	Elastic Elasto-plastic Plastic	0.53 0.64 0.50	0.41 0.50 0.33	0.77 0.78 0.66
	Elastic Plastic	1.0 1.0	0.37 0.33	0.37 0.33
	Elastic Plastic	0.40 0.50	0.26 0.33	0.65 0.66
	Elastic Plastic	1.0 1.0	0.24 0.33	0.24 0.33
	Elastic Plastic	0.87 1.0	0.52 0.56	0.60 0.56

Figure 6.6 Transformation Factors for Elastic and Plastic Behaviors

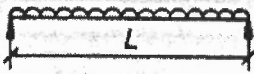
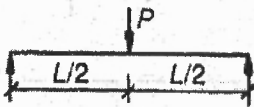
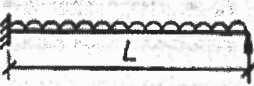
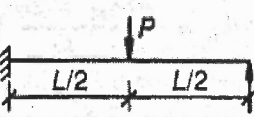
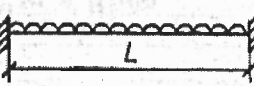
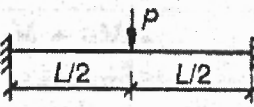
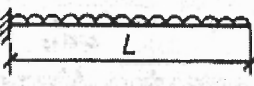
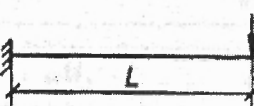
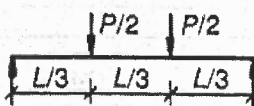
	$\frac{384EI}{5L^4}$
	$\frac{48EI}{L^3}$
	$\frac{185EI}{L^4}$
	$\frac{107EI}{L^3}$
	$\frac{384EI}{L^4}$
	$\frac{192EI}{L^3}$
	$\frac{8EI}{L^4}$
	$\frac{3EI}{L^3}$
	$\frac{56 \cdot 4EI}{L^3}$

Figure 6.7 Stiffness for beams $k = \frac{\kappa EI}{L^3}$

blast loading falls in between of that of for concentrated and uniform loading.

Regarding mass factor K_M , since distribution of mass is known, it does not pose any difficulties in selecting proper mass factor. In following sections, it is tried to get more accurate approximations for blast loading distribution based on the results of simulations reported in chapter 5.

After describing transformation factors, it is now possible to express the frequency and response of equivalent SDOF specialized for column or beams. First, frequency of the equivalent SDOF can be expressed as $\omega = \sqrt{k_e/m_e}$ based on equivalent parameters; also, the frequency may be recast based on total parameters via using transformation factors as:

$$\omega = \sqrt{\frac{K_L k}{K_M m}} = \sqrt{\frac{k}{K_{LM} m}}$$

where, $K_{LM} = K_M/K_L$ is the *load-mass factor*. For beams and columns, elastic stiffness can be written as $k = \kappa EI/h^3$ and total mass as $m = \bar{m}h = \rho Ah$; after substituting for k and m , frequency reads as:

$$\omega = \sqrt{\frac{k}{K_{LM} m}} = \sqrt{\frac{\kappa}{K_{LM}}} \sqrt{\frac{EI}{\bar{m}h^4}} \quad (6.5)$$

For response of SDOFs in impulsive-sensitive regime, maximum displacement $v_{max} = i_e/m_e\omega$ can be rewritten based on column's parameters via using transformation factors as

$$v_{max} = \frac{i_e}{m_e \omega} = \frac{K_L i}{K_M m \sqrt{k/(K_{LM} m)}} = \frac{1}{\sqrt{K_{LM}}} \frac{i}{\sqrt{k m}}$$

Substituting for elastic stiffness as $k = \kappa EI/h^3$ and total mass as $m = \bar{m}h =$

ρAh in above, maximum deflection v_{max} reads as:

$$v_{max} = \frac{1}{\sqrt{\kappa K_{LM}}} \frac{1}{\sqrt{\rho E}} \frac{h}{\sqrt{AI}} i \quad (6.6)$$

where, $\frac{1}{\sqrt{\rho E}}$ term accounts for material properties, the $\frac{h}{\sqrt{AI}}$ term represents the geometrical properties (section and height); and $\frac{1}{\sqrt{\kappa K_{LM}}}$ term contains transformation factors and it does not depend on geometrical properties. The κ and K_L factor can be determined through end support conditions as well as load distribution pattern. Mass factor K_M is not difficult to approximate, since usually mass is uniformly distributed along columns. In next section, it is attempted to back calculate $\frac{1}{\sqrt{\kappa K_{LM}}}$ through using simulation results for v_{max} .

The factors calculated from simulation results give better approximations. The merits of using simulation results in getting transformation factors are two folds. First, the deflected shape in simulations is estimated through calculating true deflected shape not prescribing an arbitrarily mode shapes. Secondly, the distribution of the blast load is not arbitrarily decided but it will be determined through solving air domain.

In next section, it will be shown the response of columns to blast is impulsive sensitive and not pressure-sensitive. However, in pressure sensitive regimes, maximum displacement for a beam/column is:

$$v_{max} = D \frac{f_e}{k_e} = D \frac{K_L f}{K_L k} = D \frac{f}{k} \quad (6.7)$$

6.4 Elastic Response of Columns

As a part of chapter 5, results of a number of 3-dimensional column simulations were presented with the focus on quantifying load and impulse on circular and rectangular columns. In those simulations, columns were modeled with linear elastic behavior. In this section, the responses of columns in previous simulations are

presented. Also, results have been used to propose specific transformation factors for blast load distributions.

If assuming the response of columns to blast loading is impulse-sensitive, then one should see the linear dependence between v_{max} and $\frac{i}{\sqrt{\rho E}} \times \frac{h}{\sqrt{AI}}$ as detailed in Equation 8.1. Actually, this line is very similar to the impulsive asymptote shown in Figure 6.3. The slope for the linear dependence is $\frac{1}{\sqrt{\kappa K_{LM}}}$. As it was mentioned, this slope does not depend on the geometry of columns.

The graph of v_{max} versus $\frac{i}{\sqrt{\rho E}} \times \frac{h}{\sqrt{AI}}$ will be plotted both for circular and square columns. By inspecting these graphs, the impulse-sensitivity of deflection can be verified. If the points follow a linear pattern, then the SDOF factors can be determined through determining the slope. The slopes determined for circular and square columns should be similar since they should not depend on geometrical properties including section shapes or sizes.

The support conditions for columns in all simulations is fixed support, since all degrees of freedom of boundary nodes are restricted. Considering fixed-end boundary condition in all simulations, the coefficient should remain constant.

In simulations, concrete properties are assumed with density of $\rho = 2400 \text{ kg/m}^3$ and Young's Modulus of $E = 27.8 \text{ GPa}$.

Circular Column: Maximum deflections at mid-height level of all 27 circular columns are reported in Table 6.1. Also v_{max} is plotted versus $\frac{1}{\sqrt{\rho E}} \times \frac{h}{\sqrt{AI}}$ in Figure 6.8. As observed, the simulation results follow a linear trend which proves that column response are impulsive sensitive. Also, the slope of the line which corresponds to $\frac{1}{\sqrt{\kappa K_{LM}}}$ is equal to 0.0787. For circular columns the $\frac{h}{\sqrt{AI}}$ term equals $\frac{h}{\frac{\pi}{16} a^3}$, where a is the diameter and h is the column height.

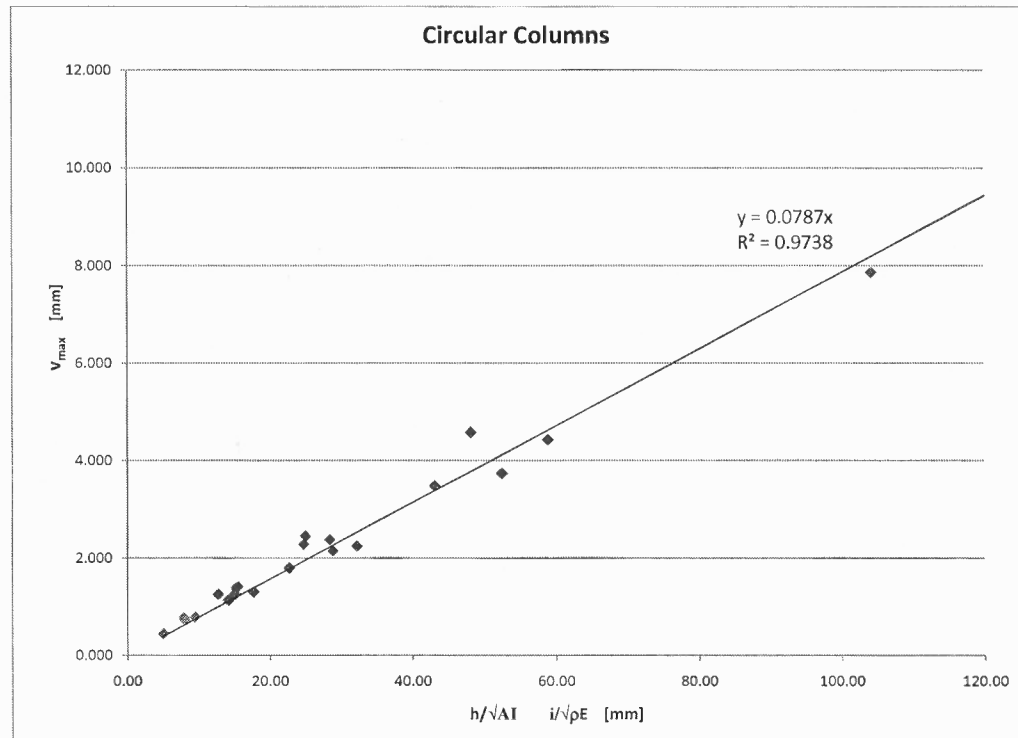


Figure 6.8 Circular Column Deflection

Square Column: Maximum deflections at mid-height level of all 27 square columns are reported in Table 6.2. Also v_{max} is plotted versus $\frac{i}{\sqrt{\rho E}} \times \frac{h}{\sqrt{AI}}$ in Figure 6.9. As observed, the simulation results follow a linear trend which proves that column response are impulsive sensitive. Also, the slope of the line which corresponds to $\frac{1}{\sqrt{\kappa K_{LM}}}$ is equal to 0.078. For square columns the $\frac{h}{\sqrt{AI}}$ term equals $\frac{h}{\sqrt{1/12 a^3}}$, where a is the section size and h is the column height.

Comparing the section properties $\frac{h}{\sqrt{AI}}$ for square and circular columns, square

Table 6.1 Deflection Results for Circular Section.

h	a	z	i	h/\sqrt{AI}	v_{max}
mm	mm	$m/kg^{\frac{1}{3}}$	$mN - ms$	m^{-2}	mm
3000	500	0.706	1.18E+09	122.23	1.300
3000	500	0.561	1.92E+09	122.23	2.145
3000	500	0.413	3.93E+09	122.23	4.440
4500	500	0.706	1.43E+09	183.35	2.247
4500	500	0.561	2.33E+09	183.35	3.739
4500	500	0.413	4.64E+09	183.35	7.863
6000	500	0.706	1.57E+09	244.47	NA
6000	500	0.561	2.61E+09	244.47	NA
6000	500	0.413	5.25E+09	244.47	NA
3000	750	0.706	1.79E+09	36.22	0.776
3000	750	0.561	2.87E+09	36.22	1.255
3000	750	0.413	5.62E+09	36.22	2.451
4500	750	0.706	2.33E+09	54.33	1.406
4500	750	0.561	3.71E+09	54.33	2.281
4500	750	0.413	7.22E+09	54.33	4.579
6000	750	0.706	2.55E+09	72.44	NA
6000	750	0.561	4.19E+09	72.44	NA
6000	750	0.413	8.21E+09	72.44	NA
3000	1000	0.706	2.68E+09	15.28	0.448
3000	1000	0.561	4.29E+09	15.28	0.722
3000	1000	0.413	8.15E+09	15.28	1.382
4500	1000	0.706	3.39E+09	22.92	0.791
4500	1000	0.561	5.37E+09	22.92	1.254
4500	1000	0.413	1.01E+10	22.92	2.381
6000	1000	0.706	3.78E+09	30.56	1.133
6000	1000	0.561	6.06E+09	30.56	1.797
6000	1000	0.413	1.15E+10	30.56	3.486

NA: Not Available. Maximum deflection did not developed during simulation duration.

columns are $\frac{1}{\sqrt{12}}/\frac{\pi}{16} \approx 1.47$ times stiffer than similar circular columns. In the previous chapter, it was shown that square columns absorbs almost 50% more impulse comparing with circular columns. Putting together these two piece of information, we can conclude the elastic deflection of square and circular columns are almost similar in a blast scenario.

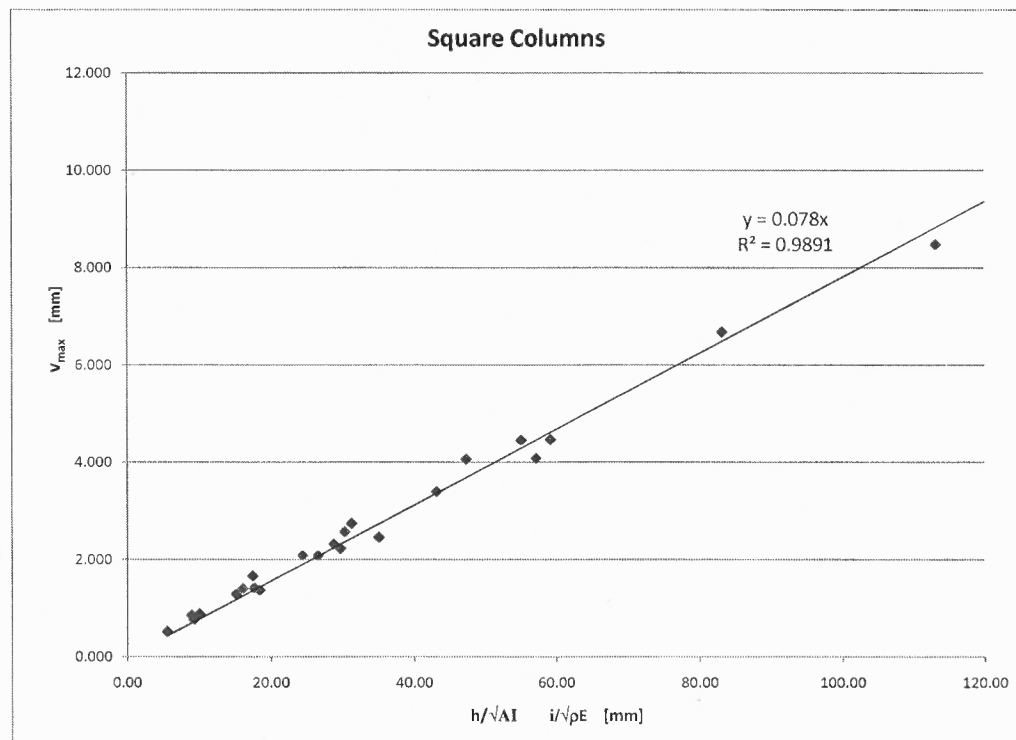


Figure 6.9 Square Column Deflection

Results Discussion: So far, the $\frac{1}{\sqrt{\kappa}K_{LM}}$ term is evaluated for fixed end columns. It was seen that this term is about 0.078 both for circular and rectangular columns.

Table 6.2 Deflection Results for Square Columns.

h	a	z	i	h/\sqrt{AI}	v_{max}
mm	mm	$m/kg^{\frac{1}{3}}$	$mN - ms$	m^{-2}	mm
3000	500	0.706	1.81E+09	83.14	1.374
3000	500	0.561	2.92E+09	83.14	2.231
3000	500	0.413	5.82E+09	83.14	4.467
4500	500	0.706	2.30E+09	124.71	2.463
4500	500	0.561	3.74E+09	124.71	4.081
4500	500	0.413	7.41E+09	124.71	8.487
6000	500	0.706	2.51E+09	166.28	NA
6000	500	0.561	4.14E+09	166.28	NA
6000	500	0.413	8.29E+09	166.28	NA
3000	750	0.706	3.07E+09	24.63	0.780
3000	750	0.561	5.02E+09	24.63	1.287
3000	750	0.413	1.01E+10	24.63	2.575
4500	750	0.706	3.92E+09	36.95	1.419
4500	750	0.561	6.37E+09	36.95	2.322
4500	750	0.413	1.22E+10	36.95	4.465
6000	750	0.706	4.40E+09	49.27	2.084
6000	750	0.561	7.15E+09	49.27	3.398
6000	750	0.413	1.38E+10	49.27	6.683
3000	1000	0.706	4.37E+09	10.39	0.523
3000	1000	0.561	7.00E+09	10.39	0.855
3000	1000	0.413	1.37E+10	10.39	1.671
4500	1000	0.706	5.27E+09	15.59	0.878
4500	1000	0.561	8.45E+09	15.59	1.407
4500	1000	0.413	1.64E+10	15.59	2.750
6000	1000	0.706	5.95E+09	20.78	1.295
6000	1000	0.561	9.59E+09	20.78	2.084
6000	1000	0.413	1.86E+10	20.78	4.061

NA: Not Available. Maximum deflection did not developed during simulation duration.

Here, this value is compared with corresponding values for uniformly distributed load as well as concentrated load in the mid-span. Assuming blast loading as concentrated in mid-span will be over estimating the deflection; however, uniformly distributing the load might be un-conservative in estimating the deflection. Based on transformation factors reported in Biggs [3], it can be shown the uniform loading and concentrated loading will provide lower and upper bounds for $\frac{1}{\sqrt{\kappa K_{LM}}} = 0.078$ that was calculated for blast loading based on simulation results.

- For concentrated loading $\kappa = 192$, and $K_{LM} = 0.37$ yields $\frac{1}{\sqrt{\kappa K_{LM}}} = 0.1186$.
- For uniform loading $\kappa = 384$, and $K_{LM} = 0.77$ yields $\frac{1}{\sqrt{\kappa K_{LM}}} = 0.0582$.

In fact, calculated value of 0.078 based on the simulation is less than the average of the factor for concentrated and distributed loading which are 0.1186 and 0.0582 respectively.

In current simulations, support conditions were taken as fixed-end. Consequently $\frac{1}{\sqrt{\kappa K_{LM}}} = 0.078$ is only applicable for fixed-end supports. Proposing appropriate factors customized for blast loading for other boundary conditions needs further simulations. From current results, it is reasonable to suggest using the average of the factors for concentrated and uniform loading obtained from the Biggs transformation factors. For example, if assuming two ends are hinged, then the factors for concentrated and distributed load will be:

- For concentrated loading $\kappa = 48$, and $K_{LM} = 0.49$ yields $\frac{1}{\sqrt{\kappa K_{LM}}} = 0.2062$.
- For uniform loading $\kappa = 384/5$, and $K_{LM} = 0.78$ yields $\frac{1}{\sqrt{\kappa K_{LM}}} = 0.1292$.

Accordingly, the proposed value for the factor $\frac{1}{\sqrt{\kappa K_{LM}}}$ would be the average of the above factors which is $\frac{1}{\sqrt{\kappa K_{LM}}} = 0.1677$ for blast loading. As compared with fixed end boundary condition, the factor is more than twice for the simply supported case;

hence, deflections for simply supported columns would be more than twice of that of fixed-end case.

We need just to have the product of κ and K_{LM} in order to calculate deformation; however, it is possible to approximate κ and K_{LM} separately. One way would be to find natural frequency from simulation results and then approximate the $\sqrt{\kappa/K_{LM}}$ coefficient in $\omega = \sqrt{\kappa/K_{LM}(EI/\bar{m}L^4)}$, say the coefficient is A. Again, assume $\sqrt{\frac{\kappa}{K_{LM}}}$ equals B. Then simply κ and K_{LM} can be evaluated via solving the following two equations; $\frac{1}{\sqrt{\kappa K_{LM}}} = A$, and $\sqrt{\frac{\kappa}{K_{LM}}} = B$. The values for κ and K_{LM} would be $\frac{B}{A}$ and $\frac{1}{AB}$, respectively.

CHAPTER 7

PERFORMANCE EVALUATION AND RETROFITTING OPTIONS

In this chapter, inelastic response of concrete columns under blast loading will be evaluated and the performance and adequacy of columns in surviving blast events will be assessed. In doing so, the true nonlinear and inelastic behavior of concrete and reinforcing steel is considered. The performance of columns will be evaluated based on the maximum deformation as well as sustained level of damage in materials. In the cases of under-performing or insufficient columns, appropriate retrofitting measures will be discussed in order to upgrade the response columns.

In the previous chapter, the elastic response of columns was discussed. This requires columns to be strong enough to withstand the blast loading in elastic range without any damage; however, in reality, structural members may undergo different levels of damage and failure. They might even get disintegrated and shattered on the instant that blast strikes. In this chapter three dimensional response of columns with true nonlinear material behaviors will be examined to study different types of damage and failure such as flexural and shear damage modes.

7.1 Background

Columns exposed to lateral blast loading are prone to different types of failures. Columns supporting lateral loading such as blast may undergo *flexural* failure due to the formation of excessive plastic hinges. In addition, *diagonal shear* failure is another possibility in the picture. Nevertheless, the presence of axial loads in columns increases the shear strength of columns. It should be noted that in short-duration dynamic loading like blast, the more common form of the shear failure is *direct*

shear which is caused by the high shear inertia forces that are not associated with flexure. Direct shear failure occurs in very localized zone as opposed to *diagonal shear* which happens under static or slow dynamic loads. The damage in columns due to blast loading can be a combination of flexural and direct shear failure. When excessive lateral deformations occur in columns, then *p-delta* instabilities can cause further damage and can cause total failure. In *p-delta* effect, secondary moments are generated due to the combined effect of axial load and lateral bending deflections. The secondary moments can further increase the lateral deflection and cause the collapse of the column.

In order to quantify the damage sustained by structural members, there are a couple of parameters that can be employed to identify the extent of the damage. For example in TM5-1300 [2], the extent of the damage is described for different element types. As shown in Figure 7.1, for beams with the ratio of lateral deflection to span smaller of 4% the flexural damage is *light*; while for ratios of larger than 15% flexural damage is considered *severe*. For ratios around 8% *moderate* damage is expected. This evaluation can be combined with simulation results to assess the level of flexural damage sustained by columns. Additionally, for shear damage, shear strains of 1%, 2%, and 3% would be considered light, moderate, and severe shear damage, respectively.

7.2 Damage Assessment

In this section, the performance of square columns to different intensities of blast load is discussed. In doing so, the largest and tallest square column considered in previous simulations has been selected to be further studied. The selected column is 6000 mm high and has a square cross section of 1000 mm \times 1000 mm. This column is exposed to three different blast intensities, namely 45.4 kg, 113.5 kg, and 227.0 kg of

Element Type	Material Type	Type of Failure	Criteria	Light Damage	Moderate Damage	Severe Damage
Beams	Reinforced Concrete ($\rho > 0.5\%/face$)	Global Bending/Membrane Response	Ratios of Center-line Deflection to Span, δ/L .	4%	8%	15%
		Shear	Average Shear Strain Across Section, γ .	1%	2%	3%
	Steel	Bending/Membrane	δ/L .	5%	12%	25%
		Shear	δ/L .	2%	4%	8%
Slabs	Reinforced Concrete ($\rho > 0.5\%/face$)	Bending/Membrane	δ/L .	4%	8%	15%
		Shear	γ .	1%	2%	3%
Columns	Reinforced Concrete ($\rho > 0.5\%/face$)	Compression	Shortening/Height	1%	2%	4%
	Steel	Compression	Shortening/Height	2%	4%	8%
Load-Bearing Walls	Reinforced Concrete ($\rho > 0.5\%/face$)	Compression	Shortening/Height	1%	2%	4%
Shear Walls	Reinforced Concrete ($\rho > 0.5\%/face$)	Shear	Average Shear Strain Across Section	1%	2%	3%

Figure 7.1 Damage Assessment for Different Structural Elements

TNT in a stand-off distance of 2000 mm. These charges translate to scaled distances equivalent of $z = 0.561, 0.413, \text{ and } 0.328 \text{ m/kg}^{\frac{1}{3}}$. Similar to previous simulations, the charge is located at the mid-height level of the column. Here, the inelastic response of the column will be studied and the level of the damage that the column sustains will be identified for each scenario.

In order to accurately model the inelastic behavior of the concrete column, both the longitudinal (bending) and lateral (shear) reinforcement have been included in the model to account for strength and confinement effects that they are providing to the concrete. In current simulations, the amount of the longitudinal reinforcement ratio provided is around 1.13% of the concrete gross area. In addition to longitudinal reinforcements, two different types of shear reinforcements – ties – have been provided. In type one, shear reinforcement includes ties with size of $\phi 16$ mm at 300 mm spacing and type two includes ties with $\phi 16$ mm at 600 mm spacing.

The yield strength of steel rebars is taken as 410 MPa (60 ksi). The uniaxial compressive strength of concrete is taken as 35 MPa (5 ksi). For concrete, RHT concrete material model is adopted. For rebars, Johnson-Cook plasticity model is used.

Results for the mid-height deflection for the two types of shear reinforcement are shown in Table 7.1. The elastic deflections that were discussed in Chapter 6, are also included in the table for comparison purposes. The results for elastic responses of the column to the first two blast intensities were simulated in the previous chapter. The elastic response to the third loading has been estimated via the SDOF transformation factor that discussed in the previous chapter. Also, impulses experienced by the column for inelastic and elastic cases are included.

Here, the results in the Table 7.1 are assessed for each blast loading intensities. First, for $z=0.561$, the column sustain very small damages only at its two supports.

Table 7.1 Comparing Elastic and Inelastic Deflections and Impulses

	Inelastic Response $\phi 16 @ 300 \text{ c/c}$		Inelastic Response $\phi 16 @ 600 \text{ c/c}$		Elastic Response No Shear Reinf.	
	v_{max}	i	v_{max}	i	v_{max}	i
z $m/kg^{\frac{1}{3}}$	mm	mN-ms	mm	mN-ms	mm	mN-ms
0.561	1.951	9.59E9	1.962	9.59E9	2.084	9.59E9
0.413	5.477	1.86E10	5.810	1.86E10	4.061	1.86E10
0.328	45.975	3.23E10	64.720	3.23E10	7.037*	3.08E10*

* denotes that values estimated with the proposed equations.

Hence, inelastic and elastic deflections are expected to be very close. In fact as it is observed, inelastic deflections are slightly smaller due to the contribution from the rebars. Note that in elastic simulations, rebars were not modeled. For $z=0.413$, some small damages occur at the center in addition to the supports. The plastic deflection is 35% to 40% more than the elastic deflection. Finally, for $z=0.328$, column undergoes fair damages and the inelastic deflection is approximately 7 times larger than that of elastic response. The elastic deflection for the latter case is calculated through proposed transformation factors since no simulation for this case has been done. Also, the elastic impulse is approximated via proposed equations in Chapter 6. It is interesting to note that proposed formula yields very good approximations even for ranges not covered in the simulation data. Also, it can be added that the impulse experienced by the columns is not affected even when columns undergo large deformations. The damage index for each loading scenario is shown in Figure 7.2 for the column with ties spaced at 300mm.

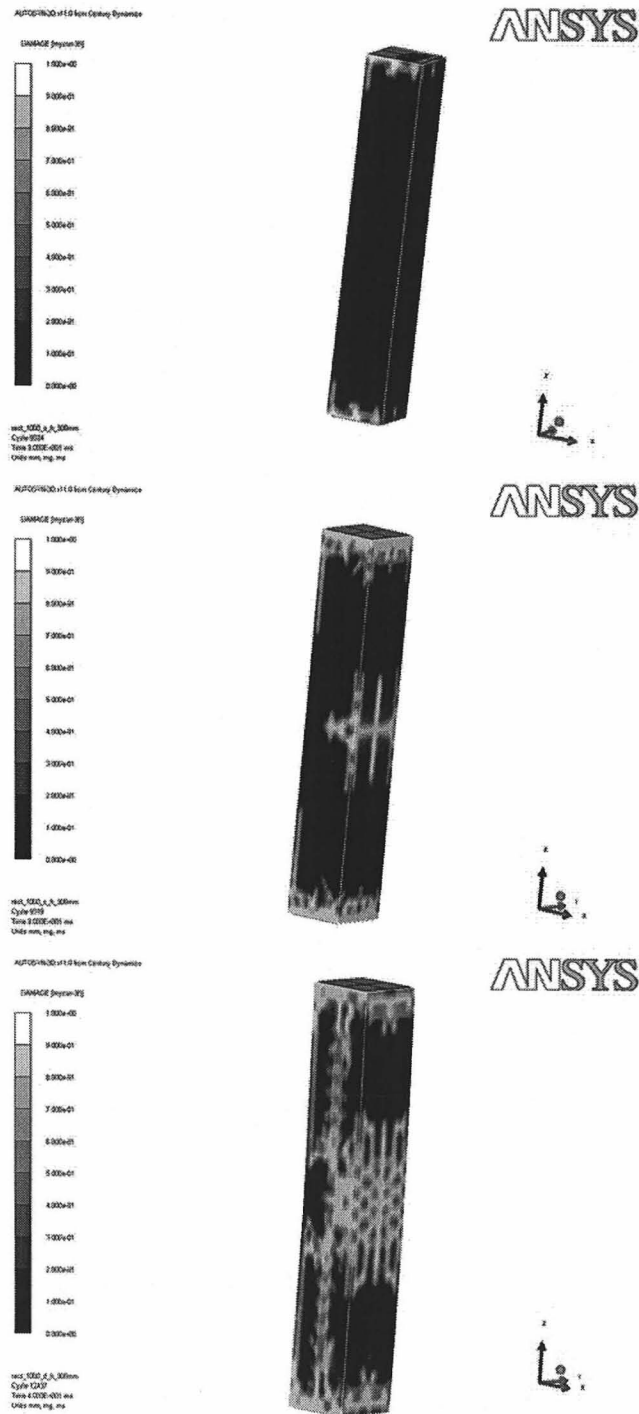


Figure 7.2 Damage Index for Square Column for Loading with $z = 0.561$ (top), $z = 0.413$ (middle), and $z = 0.328$ (bottom)

7.3 Retrofitting Measures

When an existing column deems insufficient to withstand a specific level of threat, there are ways to *retrofit* or *upgrade* its performance through providing more resistance or strength. For a column to survive a blast event, in addition to strength, enough ductility is also required to accommodate lateral deformations.

Any measures that can improve the resistance and ductility of columns will be considered beneficial to the blast response mitigation. There is a wealth of knowledge on seismic upgrading of members prepared by the Federal Emergency Management Agency (FEMA) that can be used also for blast mitigation. Efficacy of the idea of covering reinforced concrete columns with *steel jackets* or *fiber reinforced polymer* (FRP) wraps has been tested and used for seismic retrofitting. Also, use of these measures have been recommended for blast loading.

Steel jackets or composite wraps provide additional bending and shear strength to the columns. More importantly, these measures offer increased ductility to the columns in surviving blast loads. The ductility is provided through effective *confinement* to the concrete core and mobilizing the confined ductility of concrete.

Concrete expands and dilates on the onset of damage initiation. Steel jackets or composite wraps inhibit lateral expansion of the concrete columns via their relatively large stiffness through applying *hoop* stresses to the concrete. When designing retrofitting measures, the jacket or wrap must be capable of deforming within their elastic response region in order to ensure their elastic stiffness is available. This can be achieved through properly designing the thickness of the jacket or the number of layers.

In the last section on damage assessment, it was observed that a fair amount of damage is sustained by the square column when exposed to a blast loading of $z=0.328 \text{ m/kg}^{\frac{1}{3}}$. Here, it is tried to study the jacket retrofitted behavior of the

column to the same scenario of loading. The bare column studied is 6000 mm high with square cross-section of 1000×1000 mm and it has 300 mm spacing lateral (shear) reinforcement. The thickness of retrofitting plates are from steel with only 5 mm thickness.

To better understand the interaction of the steel jackets with concrete columns, a set of simulations has been performed and their responses have been compared with the bare column. In these simulations, two different retrofitting measures have been studied. In the first case, only front and back faces of the column are covered with plates. In second case, the four faces of the column are covered with the jacket. The jacket can provide confinement and resistance to the column. However, the former case only offers resistance without any effective confinement. A sketch of the columns are shown in Figure 7.3. This comparison helps to provide insights on the amount of the contribution of the jackets through confinement and resistance.

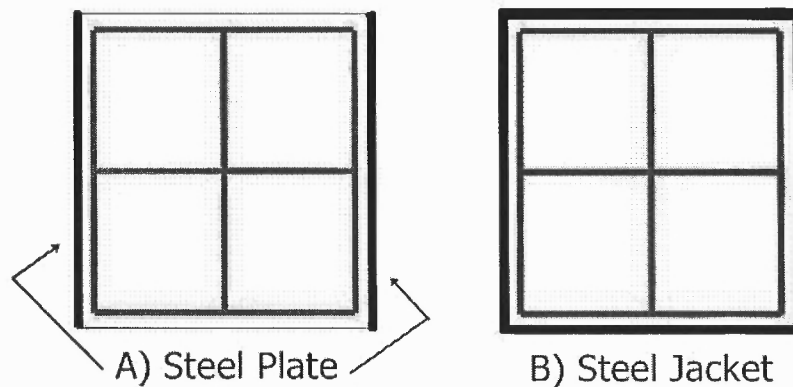


Figure 7.3 Retrofitted Columns with Plates(A) and Jacket(B)

For comparison, the mid-height deflection of the jacket retrofitted and plate retrofitted are compared with the deflection of the bare column as shown in Figure

7.4. While the calculated deflection for the plate-retrofitted column (41.4 mm) is slightly smaller than that of the bare column (46.0 mm); the jacket retrofitting is able to reduce the deflection to 14.4 mm. This shows significant response mitigation can be achieved through confining concrete columns with jackets. The plate-retrofitted column can slightly mitigate the response through providing more strength to the column.

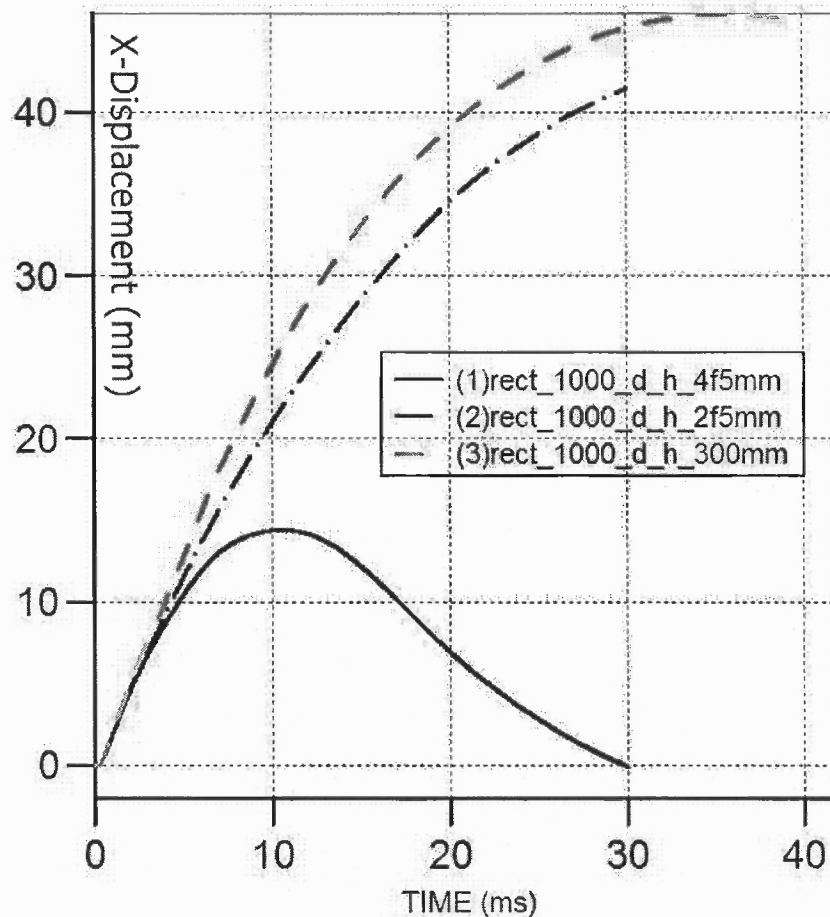


Figure 7.4 Deflection for Plate Retrofitted (dash-dot) and Jacket Retrofitted (solid) Compared with Bare Column (grey)

7.4 Material Models

In this section, a brief review has been presented for the materials employed in the simulations. For steel rebars, Johnson-Cook material model has been used. Additionally, for concrete, Riedel-Hiermaier-Thoma (RHT) model has been employed. These two material models are based on plasticity formulations.

When an explosion impinges on a structure or a hyper-velocity object impacts a target, dilatational and shear shock waves are transmitted internally at high speeds in the material. Reflection and refraction phenomena quickly occur and depending on the material properties, major disintegrations including fragmentation, spalling, and scabbing happen. For example, concrete as a relatively brittle material, tends to undergo multiple fractures which can lead to fragmentation. In steel, yielding and fracture can be expected [19]. In order to perform a reliable simulation, a proper dynamic material model should be used. In following, the material models that have been used for steel and concrete will be reviewed. For steel Johnson-Cook model has been employed, while for concrete Riedel-Hiermaier-Thoma (RHT) model has been adopted.

7.4.1 Steel Constitutive Model

In modeling dynamic loading behavior of steel, Johnson-Cook plasticity model will be used. Johnson-Cook model considers rate-effects, strain-hardening and high temperature effects. The yield surface Y is defined:

$$Y = [A + B\epsilon_p^n][1 + C \log \epsilon_p^*][1 - T_H^m]$$

where ϵ_p is effective plastic strain, $\epsilon_p^* = \dot{\epsilon}/\dot{\epsilon}_0$ is the normalized effective plastic strain rate for $\dot{\epsilon}_0 = 1s^{-1}$, $T_H = (T - T_{room})/(T_{melt} - T_{room})$. Material parameters include A, B, C, n , and m . The first term accounts for the strain-dependent yield stress in

which A is the basic yield stress at low strains and B , and n represent the effect of strain-hardening. The second and third terms represent the effects of strain-rate and temperature, respectively.

7.4.2 Concrete Constitutive Model

Riedel-Hiermaier-Thoma (RHT) concrete model was developed as an enhancement to the Johnson-Holmquist (JH) model. JH model is a dynamic concrete model which adopts a linear elastic response until a prescribed *failure (yield)* criterion, σ_f^* is reached. Afterwards, damage will accumulate as loading increases until total failure occurs. From the instant that damage initiates then the *post-failure* yield surface, σ_{pf}^* will be used. The *normalized equivalent stress*, $\sigma^* = \sqrt{3J_2}/f_c$ will be compared with the failure and post-failure surfaces in order to determine failure. The initial failure surface and post-failure surfaces account for pressure-dependency as well as strain-rate effect as:

$$\begin{aligned}\sigma_f^* &= [A + Bp^{*N}][1 + C \ln \epsilon^*] \\ \sigma_{pf}^* &= [A(1 - DI) + Bp^{*N}][1 + C \ln \epsilon^*]\end{aligned}$$

where, $p^* = p/f_c$ represents normalized pressure, and ϵ^* is the equivalent plastic strain rate normalized by a reference strain rate. Additionally, A, B, C , and N are material properties. In post-failure surface, the parameter A is reduced by a factor of $(1-DI)$, where DI is the *damage index*. Johnson-Holmquist defined the damage index as the accumulation of the ratio of equivalent plastic strain over a pressure-dependent *fracture strains* as:

$$DI = \int_0^{\epsilon_p} \frac{d\epsilon_p}{FS(p^*)}$$

where $d\epsilon_p$ is the sum of the equivalent plastic strain increment, $d\bar{\epsilon}_p$ and the plastic volumetric strain increment $d\mu_p$, i.e. $d\epsilon_p = d\bar{\epsilon}_p + d\mu_p$. Also, $FS(p^*)$ is the pressure dependent fracture strain defined as:

$$FS(p^*) = c_1(p^* + T^*)^{c_2} \text{ for } FS(p^*) > FS_{MIN}$$

$$FS(p^*) = FS_{MIN} \text{ for } FS(p^*) < FS_{MIN}$$

in which T^* is the normalized concrete uniaxial tensile strength $T^* = f_t/f_c$.

It is noteworthy that strain-rate increase factor $[1 + C \ln \epsilon^*]$ does not differentiate between tensile or compressive strains; however, in RHT different strain-rate increase factors have been adopted for tensile or compressive strains.

Additionally, in RHT model, strain hardening effect and the third invariant J_3 dependence are considered in defining yield surfaces. Also, in RHT four different strength surfaces have been defined, namely elastic Y_e , failure Y_f , residual Y_r , and post-failure Y_{pf} as depicted in Figure 7.5.

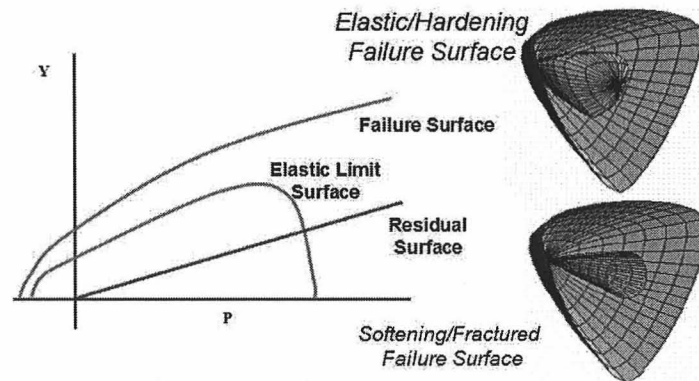


Figure 7.5 RHT Concrete Model

After failure surface is exceeded, then post-failure or fracture surface Y_{pf} would be determined by interpolation between the failure surface and the residual surface

via the damage index $0 \leq DI \leq 1$ as,

$$Y_{pf} = DI \times Y_r + (1 - DI) \times Y_f \quad (7.1)$$

Where, failure Y_f and residual Y_r yield surfaces are:

$$\begin{aligned} Y_f &= Y_c(p^*) \times r_3(\theta) \times F_{rate}(\dot{\epsilon}) \\ Y_c(p^*) &= f_c \times [A \times (p^* - p_{spall}^* \times F_{rate}(\dot{\epsilon}))^N] \\ Y_e &= Y_f(p^*/F_{elastic}) \times F_{elastic} \times F_{cap}(p) \\ Y_r &= B \times (p^*)^M \times [\text{sgn}(p^*) + 1]/2 \end{aligned}$$

In the above equations, $p_{spall}^* = f_t/f_c$; $F_{rate}(\dot{\epsilon})$ represents the dynamic increase factor for strain rate effects. F_{cap} introduces a cap on the elastic surface to limit unreal elastic responses in high pressures. $F_{elastic}$ specifies the range of elastic response as a percentage of the yield surface. Also $r_3(\theta)$ is evaluated as following:

$$r_3(\theta) = \frac{r}{r_c} = \frac{2(1 - \psi^2) \cos \theta + (2\psi - 1) \sqrt{4(1 - \psi^2) \cos^2 \theta + 5\psi^2 - 4\psi}}{4(1 - \psi^2) \cos^2 \theta + (1 - 2\psi)^2}$$

in which $\psi = r_t/r_c$ and $\cos 3\theta = \frac{3\sqrt{3}}{2} \frac{J_3}{J_2^{3/2}}$. The material properties used in RHT model are adopted from Tu et. al. [22].

7.5 Summary

In this chapter, the inelastic response of concrete columns to blast loading has been studied. The order of deflection of columns to blast scenarios has been evaluated. Also, the efficacy of steel jackets in providing confinement to the concrete columns was simulated. In an example, the deflections around 46 mm was reduced to 14 mm through using a steel jacket with thickness of 5 mm.

CHAPTER 8

CONCLUSIONS

This chapter summarizes the findings and results obtained in this study. Also, it provides suggestions and directions for future researches on the subject.

8.1 Conclusion

Chapter 1 provides an introduction to the current state of knowledge and practice on blast loading. It surveys the literature including available technical manuals in the public domain.

Chapter 2 studies the motion of a body in conjunction with the balance laws of mechanics. The balance laws are used to obtain the Euler's equations. Euler's equations govern wave propagation in a compressible and inviscid medium like air.

Chapter 3 discusses the finite element procedures used in solving differential equations and particularly Burger's and Euler's equations. This chapter explains spatial and temporal discretization. In temporal discretization, explicit and implicit time integration methods are explained.

Chapter 4 compares blast load parameters obtained with two different programs; namely Autodyn and ConWep. The former solves the governing Euler's equations while the latter is based on a semi-empirical approach. In ConWep, the peak overpressure and duration of the blast are determined from experiments. However, the pressure decay profile will be presumed as a combination of exponential and linear functions. Based on the findings in chapter 4, peak pressure and arrival time obtained from Autodyn and ConWep agree favorably. On the other hand, impulses obtained with the two approaches are less conforming. The impulse calculated in ConWep is

the area under the idealized pressure decay profile. This profile is oversimplifying some aspects of the detonation. For example, due to the disparity in the impedance properties of air and explosive materials, there are wave reflections at the interface of air and explosive materials. These reflections change the pressure profile and hence affect the impulse. Clearly, further research can provide more insights on verifying the results obtained for impulse with both ConWep and Autodyn.

In chapter 5, appropriate equations have been proposed to estimate the force and impulse imparted to columns in a blast accident. The equations for force are expressed as functions of cross section size a and scaled distance z for circular and square columns as:

$$f_{\circ} = 2.41e6 \ a \ z^{-2.3} \ \text{mN}$$

$$f_{\square} = 3.87e6 \ a \ z^{-2.4} \ \text{mN}$$

In above a is in mm and z is in $m/kg^{\frac{1}{3}}$. The proposed equations for force do not depend on the height of columns for the height range considered in the simulations. As explained, the blast load can only affect a certain portion of height of the column when maximum load is developed; and this is regardless of the extra remaining height of the column. In fact, increasing the height of columns only results in higher impulses (not forces), since the blast wave sweeps and stays on the column for extended time. Based on the proposed equation for impulse, the amount of experienced impulse is proportional with the square root of column's height in addition to cross section size a and scaled distance z :

$$i_{\circ} = 5780 \ h^{0.5} \ a^{1.2} \ z^{-2.1} \ \text{mN-ms}$$

$$i_{\square} = 8870 \ h^{0.5} \ a^{1.2} \ z^{-2.2} \ \text{mN-ms}$$

In blast design practice, usually maximum force or impulse are considered as di-

rectly proportional with the height of column. Based on the findings of this study, the assumption that blast loads are directly proportional to the height proves very conservative.

In chapter 6, it has been discussed how to use the total force and impulse estimated from equations in predicting the response of columns. The procedure to reduce the response of a column to an equivalent SDOF is described. This has been done via using transformation factors proposed by Biggs. In his work, the transformation factor for mass, stiffness, and force are provided only for *uniformly distributed* loading as well as *concentrated* loading; however, blast load distribution is neither uniform nor concentrated. Chapter 6 builds upon the work of Biggs to propose transformation factors for blast load distribution. The Biggs factors are back calculated from the simulation results for deflection.

In doing so, the slope of impulse asymptote line in shock response spectrum has been calculated from the simulation results for both circular and square column. As proved in the text, the impulse asymptote is:

$$v_{max} = \frac{1}{\sqrt{\kappa K_{LM}}} \frac{1}{\sqrt{\rho E}} \frac{h}{\sqrt{AI}} i$$

The fact that the deflections obtained from simulations follow the impulse asymptote line proves that the response of columns to blast loading is impulse-sensitive rather than pressure-sensitive. The value calculated for the slope $1/\sqrt{\kappa K_{LM}}$ both for circular and square columns are 0.078. This value lies in between of slopes calculated for uniform and concentrated loading. Based on this observation, it is recommended the transformation factors for blast loading to be taken as the average values for the uniform and concentrated loading values from Biggs tables.

Also, it is possible to compare the circular and square columns both in terms of loading and response. In spite of the fact that square column absorbs 50% more

impulse comparing with circular columns with similar size, the elastic deflection of square and circular columns are almost comparable. The reason is due to the better sectional properties of square columns. The larger area and second moment of inertia for square columns make up for the extra impulse experienced by square columns. A more meaningful comparison would be comparing circular and square columns with similar cross section area. In order for a circular and square section to have similar area, the diameter of the circular section needs to be 1.13 times larger than the size of the square. Using impulse equations, the square column experience 32% more impulse as shown in following:

$$\begin{aligned}
 i_{\circ} &= 5780 h^{0.5} (1.13a)^{1.2} z^{-2.1} \\
 &= 6693 h^{0.5} a^{1.2} z^{-2.1} \text{ mN-ms} \\
 i_{\square} &= 8870 h^{0.5} a^{1.2} z^{-2.2} \text{ mN-ms}
 \end{aligned}$$

Hence, the deflection of square column would be 32% more than that of circular column. Note that second moment of inertia for circular and square column with similar area are almost equal. In terms of deflection, circular columns outperform square columns provided both columns have equal areas.

Chapter 7 investigates the inelastic response of columns to blast loading. In this chapter the true nonlinear and inelastic response of materials have been utilized to evaluate the level of damage sustained by columns. It has been shown that employing steel jackets improves the response of columns considerably. Jackets improve the response by providing passive confinement to the core of concrete columns.

8.2 Future Research Directions

Upon examining Autodyn pressure history results in chapter 4, it was found that pressure reflection occurs at the interface of explosive materials and air. As a result, the

pressure history obtained from Autodyn will not be identical with idealized pressure profile obtained from ConWep. Further research can provide a better understanding of the reflection and consequently a better estimation of the impulse.

In chapter 5, simulations were performed to quantify blast induced loads on the column. The location of the charges were taken at the mid height of the columns. It is understood that this orientation is more critical than others; however, quantifying loading for other orientations can be also useful.

Chapter 6 discussed the equivalent SDOF for elastic response of columns. It can be advantageous to further develop the equivalent SDOF for inelastic range of response. Equivalent SDOF's can be developed for different modes of damage in columns.

In chapter 7, the efficiency of employing steel jackets as a retrofitting measure was discussed. Also, It will be useful to quantify the efficiency of retrofitting measures in column response and propose a simplified model for retrofitting measures. This model can be used in estimating the contribution of retrofitting measures in improving the response of a bare column. The simplified model will be adopted in designing proper retrofitting measures.

REFERENCES

- [1] J.D. Anderson. *Modern compressible flow: with historical perspective*. McGraw-Hill New York, 1990.
- [2] US Army, US Navy, and US Air Force. Structures to resist the effects of accidental explosions. *TM5-1300, NAVFAC P-397, AFR*, 88:22, 1990.
- [3] J.M. Biggs. *Introduction to structural dynamics*. McGraw-Hill New York, 1964.
- [4] R. Clough and J. Penzien. *Dynamics of structures*. 1975.
- [5] USAM Command. Engineering design handbook: Explosions in air, part. Technical report, One AD/A-003 817 (AMC Pamphlet AMCP 706-181), Alexandria, VA, 1974.
- [6] RD Cook. *Finite element modeling for stress analysis*. 1995.
- [7] R Courant and KO Friedrichs. *Supersonic Flow and Shock Waves*. Springer Verlag, 1977.
- [8] JO Hallquist. *LS-DYNA Theoretical Manual*. Livermore Software Technology Corporation, 2006.
- [9] AG Hanssen, L Enstock, and M Langseth. Close-range blast loading of aluminium foam panels. *International Journal of Impact Engineering*, 27(6):593–618, 2002.
- [10] American Association of State Highway and Transportation Officials. *Recommendations for Bridge and Tunnel Security*. FHWA: American Association of State Highway and Transportation Officials, 2003.
- [11] TJR Hughes. *The finite element method: linear static and dynamic finite element analysis*. Prentice-Hall Englewood Cliffs, NJ, 1987.
- [12] Ansys Inc. ANSYS Autodyn users manual v.11. *ANSYS Inc., Southpointe*, 2007.
- [13] N. Kambouchev, L. Noels, and R. Radovitzky. Nonlinear compressibility effects in fluid-structure interaction and their implications on the air-blast loading of structures. *Journal of Applied Physics*, 100, 2006.
- [14] D Kuzmin, R Löhner, and S Turek. *Flux-corrected Transport: Principles, Algorithms, And Applications*. Springer, 2005.
- [15] CB Laney. *Computational Gasdynamics*. Cambridge University Press, 1998.
- [16] G Mays and PD Smith. *Blast effects on buildings*. Thomas Telford, 2001.

- [17] P.F. Mlakar Sr, W.G. Corley, M.A. Sozen, C.H.T. Fellows, et al. The Oklahoma City bombing: analysis of blast damage to the Murrah Building. *Journal of Performance of Constructed Facilities*, 12:113, 1998.
- [18] DK Ofengeim and D Drikakis. Simulation of blast wave propagation over a cylinder. *Shock Waves*, 7(5):305–317, 1997.
- [19] Commission on Engineering and Technical Systems. *Protecting Buildings from Bomb Damage: Transfer of Blast-Effects Mitigation Technologies from Military to Civilian Applications*. National Academy Press, Washington, DC, 1995.
- [20] Andrs Schenker, Ido Anteby, Erez Gal, Yosef Kivity, Eyal Nizri, Oren Sadot, Ron Michaelis, Oran Levintant, and Gabi Ben-Dor. Full-scale field tests of concrete slabs subjected to blast loads. *International Journal of Impact Engineering*, 35(3):184–198, 2008.
- [21] Y Shi, H Hao, and ZX Li. Numerical simulation of blast wave interaction with structure columns. *Shock Waves*, 17(1):113–133, 2007.
- [22] Z Tu and Y Lu. Evaluation of typical concrete material models used in hydrocodes for high dynamic response simulations. *International Journal of Impact Engineering*, 36(1):132–146, 2009.
- [23] J. A. Zukas. *Introduction to Hydrocodes*. Elsevier Science, 2004.